united nations
educational, scientific
and cultural
organization

international atomic
energy agency

the
**abdus salam**
international centre for theoretical physics

**SMR 1302 - 19**

---

**WINTER SCHOOL ON LASER SPECTROSCOPY AND APPLICATIONS**

**19 February - 2 March 2001**

---

# *Background Information for lectures on High Resolution Spectroscopy and Laser Cooling*

M. INGUSCIO
L.E.N.S. - Lab. Europeo di Spettroscopie Non Lineari
Largo Enrico Fermi, 2 - Firenze, Italy

---

***These are preliminary lecture notes, intended only for distribution to participants.***

# SPECTROSCOPY, LASER

MASSIMO INGUSCIO, *Department of Physics of the University, Firenze, Italy*

ANTONIO SASSO, *Department of Physics of the University, Napoli, Italy*



## INTRODUCTION

Most of what we know of atomic and molecular structure has been derived from spectroscopic analysis of the radiation emitted when atoms or molecules are excited. From measurements of the wavelengths and intensities of observed spectral components, pioneering spectroscopists, with diligent and patient work, laid the basis upon which the exploration of the physics of microsystems would begin.

The foundation of spectral analysis dates back to about 1860, with Kirchhoff and Bunsen. The first instruments for wavelength measurement were spectrographs, which, in their modern version, continue to occupy an important position in the spectroscopy laboratory. The sample under investigation would be suitably excited, generally by means of an electrical discharge, and the emitted light dispersed by prisms or diffraction gratings. Finally, the emergent light was sent to a photographic plate upon which the spectra were recorded [excitation spectroscopy, Fig. 1(a)]. Alternatively, light from a





3-527-29300-0/97/$5.00 + .50

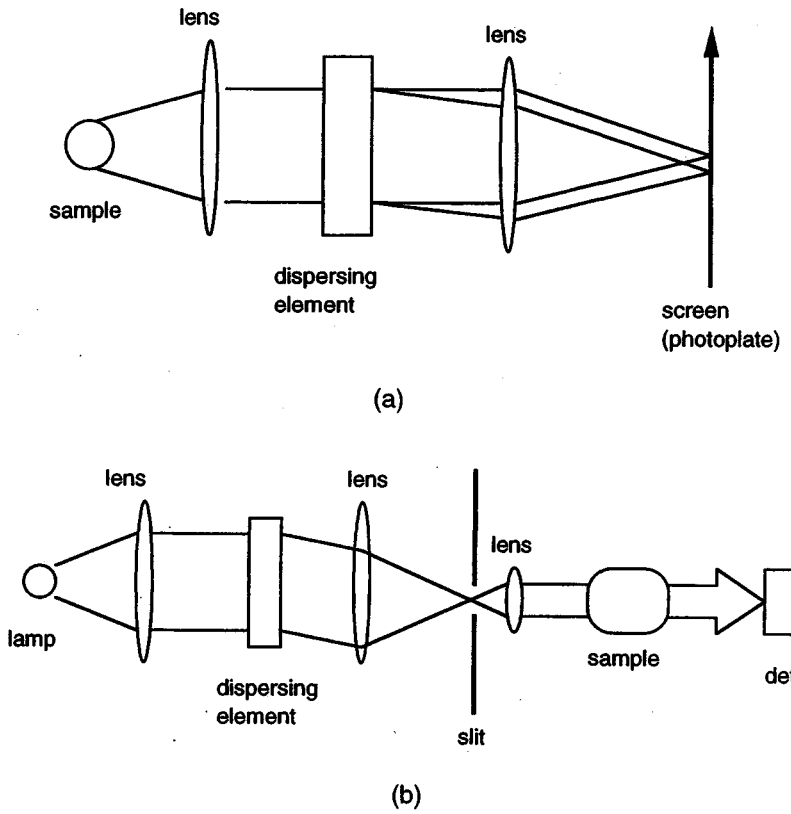


**FIG. 1.** Principle of (a) excitation and (b) absorption spectroscopy. In (a), the sample is excited, for instance, by an electrical discharge, and the emitted light sent into a prism spectrograph. In (b), light from a lamp is dispersed and the sample then investigated using only wavelengths that are resonant with a transition of the atomic or molecular species.

lamp could be selected in wavelength and used to record the absorption of the sample [absorption spectroscopy, Fig. 1(b)].

The first approach to treating the large amount of information accumulated during the early decades of these investigations consisted of finding some regularity in the sequences of spectral lines. Liveing and Dewar, in around 1880, emphasized physical similarities between the spectral lines of alkali elements and overtones in acoustics. In 1883, Hartley found an important numerical relationship that allowed, from the large number of lines in any given spectrum, the isolation of those groups of lines (multiplets) that were undoubtedly related. It soon became evident that the frequency $\nu$ was more representative than the wavelength $\lambda$. Nevertheless, because we measure directly not frequency but wavelength, it is customary in spectroscopy to use, instead of the frequency itself, the wave number $\tilde{\nu} = 1/\lambda$.

Our knowledge of spectral series formulas dates from a discovery by Balmer, in 1885. He reproduced very closely the wavelengths of the nine then-known lines in the visible spectrum of hydrogen (Balmer series) using a simple formula:

$$\lambda_n = 3645.6n^2/(n^2 - 4)\ \text{Å}, \qquad (1)$$

$n$ being a variable integer number assuming the values 3, 4, 5, ... for, respectively, the first, second, third, and so on lines in the spectrum. Other series of hydrogen were investigated in the ultraviolet by Lyman in 1906 and, two years later, in the infrared by Paschen.

A more general formula applicable to other series and elements was found by Rydberg. Using the comparatively large mass of wavelength data then available for alkali elements, Rydberg found that the wave numbers of the observed spectral sequence were described by the formula

$$\tilde{\nu}_n = \tilde{\nu} - R_\infty/(n + \mu)^2, \qquad (2)$$

where $\mu$ and $\tilde{\nu}$ are constants depending upon the series, $\tilde{\nu}$ representing the high-frequency limit to which the lines in the series converge. The constant $R_\infty$ in Eq. (2), now called the Rydberg constant, was found to be independent of the series considered and showed slight variations from one atom to another. The level scheme of the hydrogen atom is shown in Fig. 2, and a photograph of the Balmer spectral series is shown in Plate 1.

As is well known, at the beginning of this century many experimental observations not explicable in terms of classical physics led to

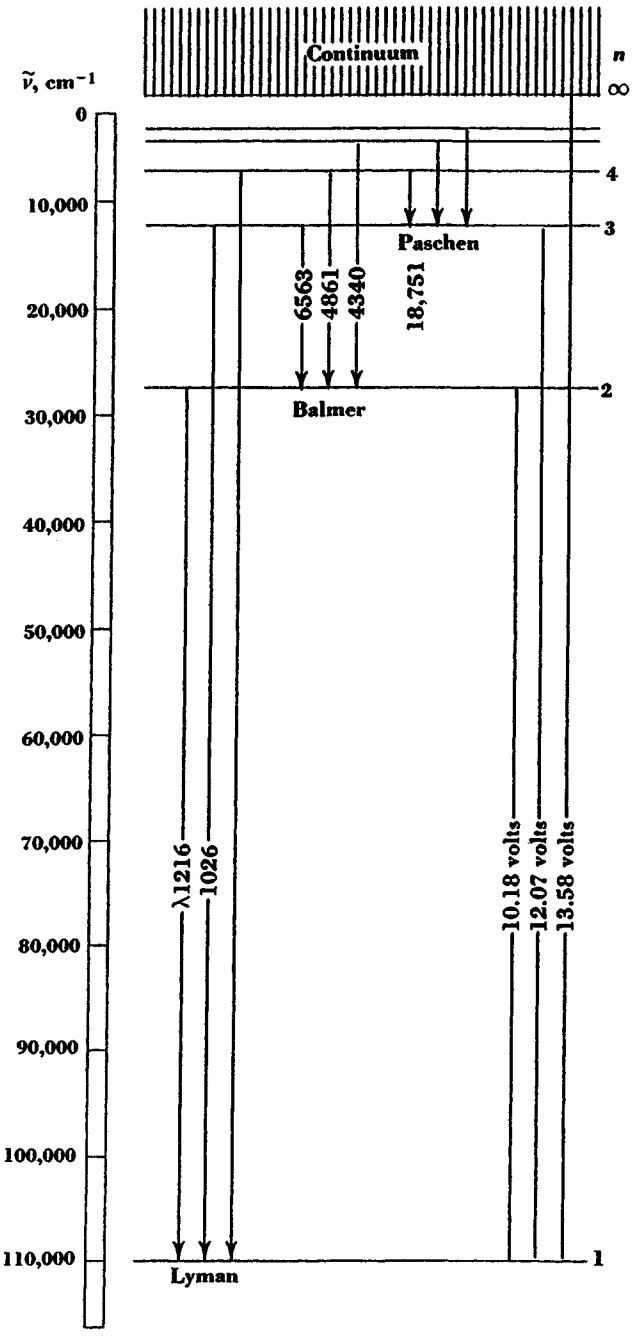


**FIG. 2.** Energy-level diagram of the hydrogen atom, showing some of the lines of the principal series.

the formulation of quantum mechanics. In particular, Niels Bohr was to apply the idea of quantum mechanics to the hydrogen atom, arriving at a theoretical formula for its spectrum that agreed with observations and with the empirical formulas of Balmer and Rydberg. According to Bohr's model, electrons move around the nucleus with definite energies. When an electron makes a transition from one allowed stationary state with energy $E_u$ to another of lower energy $E_l$, the frequency of the emitted radiation is determined by the condition that

$$h\nu = E_u - E_l, \tag{3}$$

where $h$ is the Planck constant ($h = 6.63 \times 10^{-34}$ J s). Conversely, it is necessary to absorb a quantum of electromagnetic energy—a photon—with energy $h\nu$ in order to induce a transition from a lower- to a higher-energy level. Measurements of the wavelengths of spectral lines are therefore related to the separations between energy levels, while the measured intensities are proportional to the transition probabilities.

From this basic idea of Bohr, experimental and theoretical investigations of atomic and molecular structure have evolved considerably over the intervening decades. Newer and more accurate experimental observations have stimulated the development of deeper and more sophisticated theories, and theoretical predictions have, in their turn, challenged experimentalists to seek ever finer structure in the spectra of atoms and molecules. This process gained a stimulating impetus from the discovery of the laser, which opened a new era in spectroscopy. On one hand, laser sources have allowed a return to classical spectroscopic techniques with an increase in spectral resolution and sensitivity of several orders of magnitude. More importantly, though, the many peculiarities of laser radiation (high intensity and spectral purity, short light pulses, etc.) have made it possible to explore the interaction between radiation and matter in a completely new light. Many experiments that could not be performed with classical radiation are now feasible, and new techniques based upon coherent light have reached, in the spectra of atoms and molecules, the ultimate limits of resolution.

Besides fundamental physics, spectroscopic investigations are of direct importance in fields such as astrophysics, combustion, and plasma physics and in an increasing variety of applications. Optical absorption and emission spectroscopy, for example, are used for the remote sensing of atmospheric pollutants and for medical tests.

In the following pages, the main techniques of modern laser spectroscopy are examined. For discussions in detail, the reader is referred to more specific and exhaustive

textbooks as, for instance, Corney (1977), Demtroeder (1981), Svanberg (1992), and Letokhov and Chebotayev (1977). In this work the physics of the laser is not treated; for a review of this subject, we suggest the following excellent books: Siegman (1971), Svelto (1976), and Yariv (1975).

## 1. WIDTHS OF SPECTRAL LINES

The more deeply we understand the structure of an atom or molecule, the higher is the resolution with which we need to examine its absorption and emission spectra. The limit of resolution is determined by the width of the spectral lines. According to the Rayleigh criterion, two close lines with equal intensities are resolved if the dip produced in the overlapping profile drops to 0.8 of the maximum intensity. In general, the spectral resolving power $R$ of any dispersing instrument is defined by

$$R = \lambda/\Delta\lambda = \nu/\Delta\nu \tag{4}$$

where $\Delta\lambda = \lambda_2 - \lambda_1$ is the minimum separation of two closely spaced lines that are just resolved.

The primary limit to the spectral resolution is usually the optically dispersing element used in the spectroscopic apparatus. Even if the experimental resolution is extremely high, however, spectral lines will still exhibit an intrinsic breadth. In other words, the lines in discrete spectra are never strictly monochromatic but show a spectral distribution $I(\nu)$ around the central frequency $\nu_0 = (E_u - E_l)/h$, $E_u$ and $E_l$ being the energies of the upper and lower levels of the transition under investigation. The width of such a line profile is usually expressed in terms of the so-called full width at half maximum (FWHM), which corresponds to the frequency interval $\Delta\nu$ where

$$I(\nu_0 - \Delta\nu/2) = I(\nu_0 + \Delta\nu/2) = I(\nu_0)/2. \tag{5}$$

### 1.1 Mechanisms of Line Broadening

There are several mechanisms that cause a broadening of the emission or absorption lines of atoms or molecules. These are usually divided into two categories, homogeneous and inhomogeneous broadening, depending upon whether the probability of absorption or emission of radiation with frequency $\nu$ is equal (homogeneous) or is not equal (inhomogeneous) for all the atoms of the sample.

**1.1.1 Homogeneous Broadening** The natural (also named radiative or spontaneous) width is an example of homogeneous broadening and represents the intrinsic breadth of a spectral line. The finite lifetime $\tau$ of an excited level gives rise, as described by the uncertainty principle of Heisenberg that $\Delta E \Delta t \gtrsim h$, to an uncertainty in the energy of the level. As a consequence, the radiation emitted when an electron jumps from that level to the ground state is composed of different frequencies, and the relative frequency distribution gives rise to a line shape described by a Lorentzian curve,

$$\begin{aligned} I(\nu) &= I(\nu_0)L(\nu - \nu_0) \\ &= I_0\gamma/[4\pi^2(\nu - \nu_0) + (\gamma/2)^2], \end{aligned} \tag{6}$$

where $I_0$ is the total intensity of the line and $\gamma = 2\pi\Delta\nu_{\text{nat}} = 1/\tau_u$ is the homogeneous width (FWHM). The line shape $L(\nu - \nu_0)$ is normalized; i.e., the area under the curve is unity.

If the lower level of the transition is also radiative with a lifetime $\tau_l$, then the radiative width becomes

$$\Delta\nu_{\text{nat}} = 1/2\pi\tau_u + 1/2\pi\tau_l. \tag{7}$$

Typically, the lifetime of radiative levels is of the order of tens of nanoseconds, and hence typical natural widths are of a few MHz.

Transitions do not necessarily occur between any arbitrary pair of energy levels because of general selection rules deriving from the conservation of energy, angular momentum, parity, etc. In general, such levels are said to be metastable and the line shape of the transition connecting them is extremely narrow. Such atoms usually decay through nonradiative processes, such as collisions with other atoms or with the walls of the gas container. For this reason, collisions also play an important role in the shape of spectral profiles. Collisions can be inelastic or elastic, depending upon whether the internal energy of the colliding partners is modified or not after the collision. Elastic collisions affect the phase but not the amplitude

of the wave function of the atomic state. The total effect of the collisions is to produce a shift and a broadening of the line shape. Collisional (or pressure) broadening is proportional to the pressure $p$ of the collision partner species, and the total homogeneous width is given by the sum of two terms:

$$\gamma_{\text{hom}} = \gamma_{\text{rad}} + \gamma_{\text{coll}} = \gamma_{\text{rad}} + ap. \tag{8}$$

In some cases, the interaction time of atoms with the radiation field can be shorter than the spontaneous lifetime, giving rise to time-of-flight broadening. In such circumstances the linewidth is determined by the interaction time $T$, and in the limiting case the width becomes

$$\gamma = 1/2\pi T. \tag{9}$$

### 1.1.2 Inhomogeneous Broadening

The main cause of inhomogeneous broadening for atoms and molecules in the gas phase is the Doppler effect. The central frequency $\nu_0$ emitted by an excited atom moving with velocity $\mathbf{v}$ relative to the rest frame of the observer will be shifted by a quantity $\Delta\nu$ given by

$$\Delta\nu = \nu - \nu_0 = \mathbf{k}\cdot\mathbf{v}, \tag{10}$$

where the wave vector $\mathbf{k}$ ($|\mathbf{k}| = 2\pi/\lambda$) indicates the direction of the emitted photon. At thermal equilibrium the molecules of a gas follow a Maxwellian velocity distribution. The whole line shape is hence given by the superposition of differently Doppler-shifted emitters, and the observed line shape is a Gaussian:

$$I(\nu) = I_0(0.94/\Delta\nu_{\text{D}}) \exp -[(\nu - \nu_0)^2/(0.36\Delta\nu_{\text{D}}^2)], \tag{11}$$

where the FWHM is given by

$$\Delta\nu_{\text{D}} = 7.16 \times 10^{-7}\nu_0(T/M)^{1/2} \tag{12}$$

with $T$ the gas temperature (expressed in kelvins) and $M$ the molar mass (expressed in grams). For the sodium $D_1$ line, the Doppler width is, at $T = 500$ K, $\Delta\nu_{\text{D}} = 1.7$ GHz, about two orders of magnitude broader than the radiative width. Since the Doppler width is proportional to the frequency $\nu$, line shapes of transitions in the infrared and microwave spectral regions are, in practice, little affected, while in the optical domain (the visible and ultraviolet) the Doppler effect is the dominant broadening mechanism.

From the previous discussion we can conclude that homogeneous and inhomogeneous broadening are governed by two line profiles: the Lorentzian and the Gaussian. Although the two curves appear similar, significant differences appear if we compare two curves having the same half-width, as shown in Fig. 3.

In our discussion of Doppler broadening, we have neglected the homogeneous broadening of each velocity class of atoms. This means that we should properly write the whole line shape as a superposition of different Lorentzian curves, each centered at the Doppler-shifted frequency and weighted by a Gaussian curve. The result of such a convolution of a Lorentzian and a Gaussian is called a Voigt profile (see Fig. 4). In practice, when $\Delta\nu_{\text{D}} \gg \Delta\nu_{\text{hom}}$, the line shape is well described by a Gaussian curve.

## 2. HIGH-RESOLUTION SPECTROSCOPY

The intrinsic width of a spectral line is determined by spontaneous emission. It may be desirable to reach such a limit experimentally for two main reasons: simply because it represents the highest resolution possible and to be able to investigate properties of isolated atoms in the absence of external perturbations (other than the laser radiation used for the experiment itself). Especially when the gaseous sample under investigation is rarefied in order to render collisions negligible, the Doppler effect will be the first obstacle to overcome.

At first sight, the easiest approach to reducing Doppler broadening might appear to be by cooling the sample. However, the slow dependence of $\Delta\nu_{\text{D}}$ upon temperature [see Eq. (12)] means that, for instance, to reduce $\Delta\nu_{\text{D}}$ by two orders of magnitude, the gas temperature must be decreased by four orders of magnitude. This is practically feasible only for atomic and molecular species with high vapor pressures.

Another approach that has been used to reduce Doppler broadening is the use of atomic beams. If a well-collimated beam of

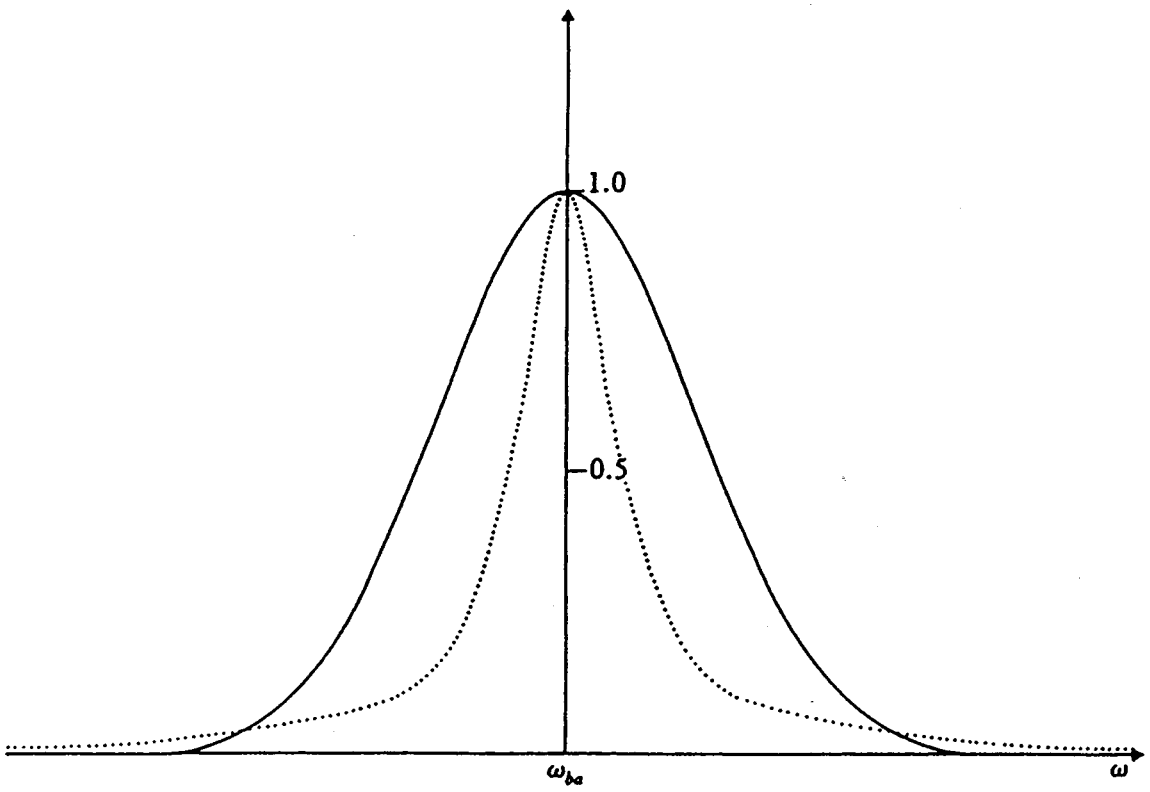


**FIG. 3.** Comparison between Lorentzian (homogeneous broadening) and Gaussian (inhomogeneous broadening) line shapes having equal maxima.

particles is irradiated perpendicularly by resonant radiation, then the first-order Doppler effect is removed ($\mathbf{k}\cdot\mathbf{v} = 0$). Because of the finite collimation of the beam, of course, the Doppler effect will still be present due to the small velocity component perpendicular to the atomic beam. If $\theta$ is the beam divergence, the residual Doppler effect is given by $\Delta\nu_{\text{D-res}} = \Delta\nu_{\text{D}} \tan\theta$.

It is worth noting that the relativistic second-order Doppler effect, depending upon $(v/c)^2$, is not eliminated even with a perfectly collimated beam. This quadratic Doppler effect can play an important role in ultrahigh-resolution spectroscopy, and we shall see later some novel techniques based upon laser cooling of the atoms that aim to overcome this limit. It should also be noted that, because the atoms interact with the laser radiation downstream of the nozzle, the method of atomic beam spectroscopy is not appropriate for the study of species in excited states with short lifetimes.

Doppler-free resolution is also possible us-

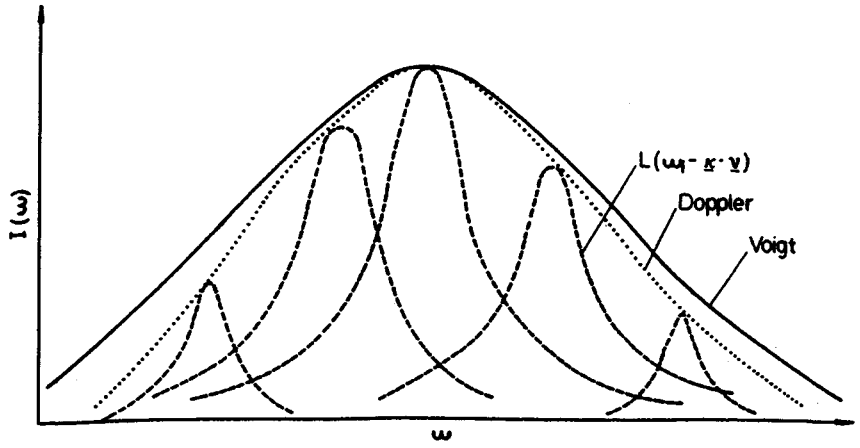


**FIG. 4.** Voigt profile obtained from the convolution of Gaussian and Lorentzian profiles (from Demtroeder, 1981).

ing classical light sources. This has been achieved, for instance, using double-resonance schemes in which two successive transitions, one in the visible and another in the radio-frequency region, are excited simultaneously (see Fig. 5). The radio-frequency transition will be between two closely spaced energy levels, such as fine-structure or hyperfine levels; the Doppler width of these transitions, as explained previously, will be negligible, and the levels' spacing, if not their absolute positions, may thus be measured with high resolution.

Level splittings may also be investigated with the methods of level-crossing (Hanle effect) or quantum-beat spectroscopy. These techniques are based on the interference between different atomic radiative transition channels, which lead to a spatial distribution of the intensity and polarization of the emitted radiation. The need for radiation of high spectral purity is avoided, and these techniques are particularly valuable for accurate measurements of fine and hyperfine structure and of the Zeeman and Stark splittings of atomic and molecular levels.

The advent of tunable laser sources has allowed the development of nonlinear techniques that eliminate Doppler broadening without suffering from these restrictions. They are therefore competitive with and complementary to the older spectroscopic methods and have led to a number of novel spectroscopic studies that would otherwise hardly have been possible. These techniques are applicable to atoms and molecules in cells and hence have an immediate practical advantage with respect to beam methods, which require complex and expensive apparatus.

Doppler-free laser spectroscopic techniques are mainly based on two different schemes: saturation spectroscopy and Doppler-free two-photon spectroscopy. In the former, narrow-band cw laser radiation "marks" a small group of atoms within a narrow range of axial velocities. In two-photon spectroscopy an atom undergoes a transition between two quantum states of the same parity through the absorption of two photons, whose energies add up to the required energy. If the photons are absorbed from counterpropagating beams, the Doppler effect is cancelled. The basic principles of these sub-Doppler techniques are outlined using a rather simple approach in the following paragraphs.

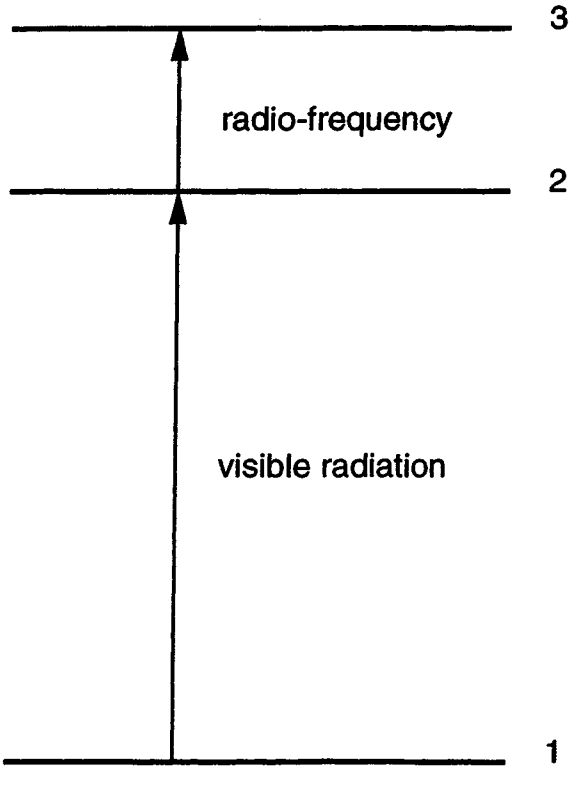


**FIG. 5.** Level scheme for double resonance involving optical and radio-frequency radiation.

### 2.1 Saturation Spectroscopy

We start with a single optical transition between two energy levels 1 and 2. Initially, we suppose that such a transition is homogeneously broadened. We recall that in linear (low intensity) absorption spectroscopy, the absorption of the intensity $I$ as a function of the optical thickness $z$ of the sample is given by the well-known Beer–Lambert law

$$I(z) = I(0)\exp(-\alpha z), \tag{13}$$

where $\alpha$ is the absorption coefficient, a quantity depending upon microscopic properties of the medium under investigation. For low light intensities, the population densities of the upper ($N_2$) and lower ($N_1$) levels of the investigated transition are only slightly changed, and the coefficient $\alpha$ is thus independent of intensity:

$$\alpha = \sigma_{12}[N_1 - (g_1/g_2)N_2]. \tag{14}$$

where $\sigma_{12}$ represents the absorption cross

section and $g_1$ and $g_2$ the degeneracies of the upper and lower levels, respectively. At higher intensities, $N_1$ may decrease significantly while the upper-state density $N_2$ increases, ultimately rendering the atomic sample completely transparent ($\Delta N = N_2 - N_1 = 0$). Since $N_2$ and $N_1$ are both functions of intensity, the absorption coefficient itself becomes nonlinearly intensity dependent. In this case, it can be shown that the population difference $\Delta N$ can be written as

$$\Delta N = \Delta N_0/[1 + S(\nu)], \tag{15}$$

where $\Delta N_0$ is the population difference in the absence of laser radiation and $S(\nu)$ is the so-called saturation parameter,

$$S(\nu) = S_0 \frac{(\gamma/2)^2}{(\omega - \omega_0)^2 + (\gamma/2)^2}, \tag{16}$$

where $\gamma$ is the homogeneous breadth of the transition and $\omega = 2\pi\nu$ the optical angular frequency. The saturated absorption coefficient $\alpha_s(\nu)$ thus becomes

$$\alpha_s(\nu) = \frac{C}{1 + I/I_s} \frac{(\gamma_s/2)^2}{(\omega - \omega_0)^2 + (\gamma_s/2)^2}, \tag{17}$$

where $C$ is a constant. Comparing Eq. (17) with the unsaturated absorption profile of Eq. (14), we see that saturation decreases the absorption by a factor $1 + S(\nu)$ and broadens the line profile by a factor $(1 + S_0)^{1/2}$, as shown in Fig. 6.

We now consider the effect of the motion of the atoms. If the laser beam is a monochromatic wave of angular frequency $\omega$ and wave vector $\mathbf{k}$, the Doppler shift will mean

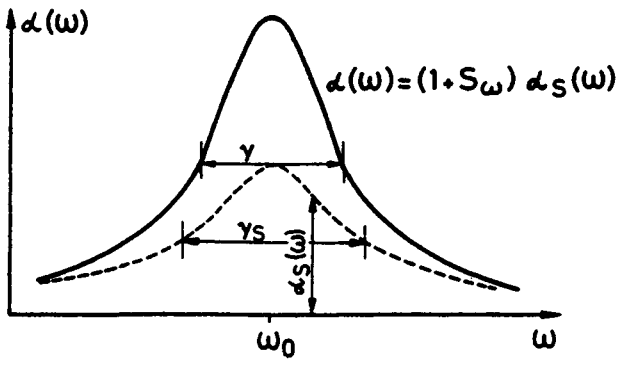


FIG. 6. Homogeneous line shape affected by saturation (from Demtroeder, 1981).

that only atoms having a velocity component toward the laser in the interval $v \pm \Delta v$ given by the relation

$$(v \pm \Delta v)\mathbf{k} = \omega - \omega_0 \pm \gamma \tag{18}$$

will absorb. This causes a hole in the velocity distribution of the lower level and a corresponding bump in the upper-level distribution. As we have seen, this group of atoms will undergo saturation, and hence the hole (or dip) will exhibit a saturated profile. If the laser beam, after crossing the sample, is reflected back into the cell, then two symmetric holes (or dips) will be produced in the velocity distribution. As the laser frequency approaches the resonant frequency $\nu_0$ of the transition, the two holes will collapse into one, and the two counterpropagating beams will simultaneously interact with the same group of atoms; see Fig. 7(a). Tuning the laser frequency across the Doppler width, it can be shown (in the weak-field approximation) that the absorption coefficient will be given by

$$\alpha_s(\omega) = \alpha D(\omega) \times \left[1 - \frac{S_0}{2}\left(1 + \frac{(\gamma_s/2)^2}{(\omega - \omega_0)^2 + (\gamma_s/2)^2}\right)\right], \tag{19}$$

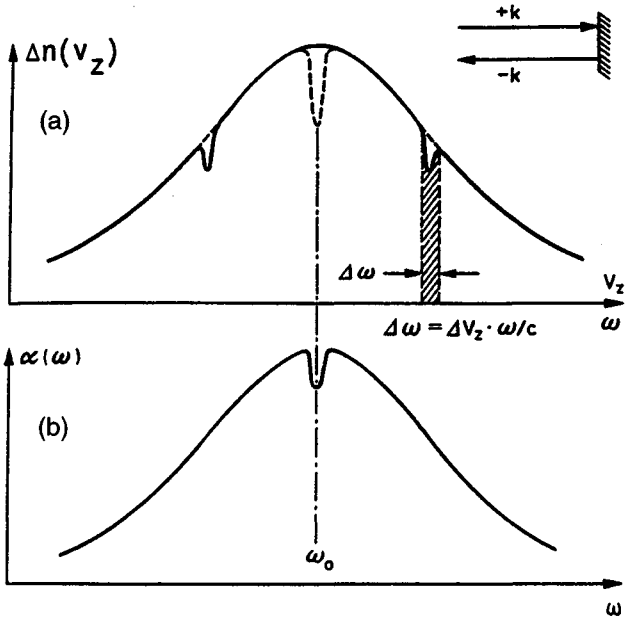


FIG. 7. (a) Holes in the velocity distribution of the lower level produced by two counterpropagating laser beams when the laser frequency is off resonance and in resonance. (b) The absorption profile as a function of the laser tuning.

which represents a Doppler profile modified by the presence of a minimum at the center of the line [the Lorentzian term in Eq. (19)] as shown in Fig. 7(b).

In the previous analysis we have considered an atomic system at thermal equilibrium where $N_1 < N_2$. The same discussion can be extended to systems where a population inversion has been produced. This is, for instance, the case of a laser medium with an inhomogeneously broadened gain profile. If the length of the single-mode laser cavity is tuned so that the laser frequency $\nu_l = \nu_0$, the output power will show a minimum around the central frequency $\nu_0$.

Historically, saturation spectroscopy at optical frequencies dates from 1963 (three years after the discovery of the laser) when McFarlane *et al.* (1963) and, independently, Szöke and Javan (1963) demonstrated the saturation minimum at the center of the emission curve of a single-mode He–Ne laser. Nevertheless, saturation spectroscopy became extensively used as a spectroscopic technique only with the advent of tunable dye lasers. Hänsch *et al.* (1971) developed an experimental arrangement that provided a Doppler-free profile with a good signal-to-noise ratio. This scheme is shown in Fig. 8. The primary beam is divided in two using a partially reflecting mirror (beam splitter). One of the two beams has a higher intensity than the other, by about a factor of 10, and is usually named the pump or saturating beam, while the weaker is called the probe or analysis beam. The two beams are sent in opposite directions through the cell, and the intensity of the transmitted probe is detected using, for example, a photodiode. When the laser is tuned across the absorption line, the probe beam sees the hole burned by the saturating beam, and the recorded line shape consists of a Gaussian with a dip at the center. In order to isolate the saturating contribution, a phase-sensitive detection scheme can be used. For this purpose, the intensity of the pump beam is mechanically chopped at a given frequency—a few hundred Hz—and the signal processed using a lock-in amplifier.

A typical saturation spectrum is shown in Fig. 9 for the neon transition $1s_4(J = 1)$–$2p_4(J = 0)$ at 607.4 nm, obtained with a single-mode dye laser. The lower level of this transition is metastable and is populated by an electrical glow discharge. Figure 9(a) shows the Doppler-broadened absorption profile obtained with a single laser beam, from which a 2-GHz Doppler width may be estimated, corresponding to a gas temperature of about 500 K. A slight asymmetry is apparent, due to the presence of two closely spaced transitions corresponding to the two isotopes $^{20}$Ne and $^{22}$Ne present in the discharge with natural abundances of 91% and 9%, respectively. When counterpropagating beams are used, Lamb dips are produced at the resonances of the two isotopes [Fig. 9(b)]. Finally, a Doppler-free recording may be obtained using a phase-sensitive detection

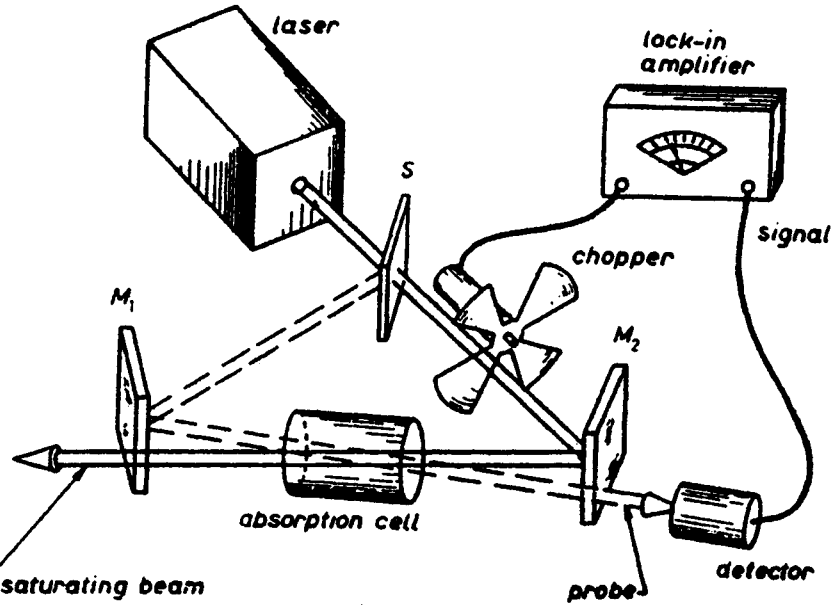


FIG. 8. Typical experimental arrangement for saturation spectroscopy (from Hänsch, 1975).

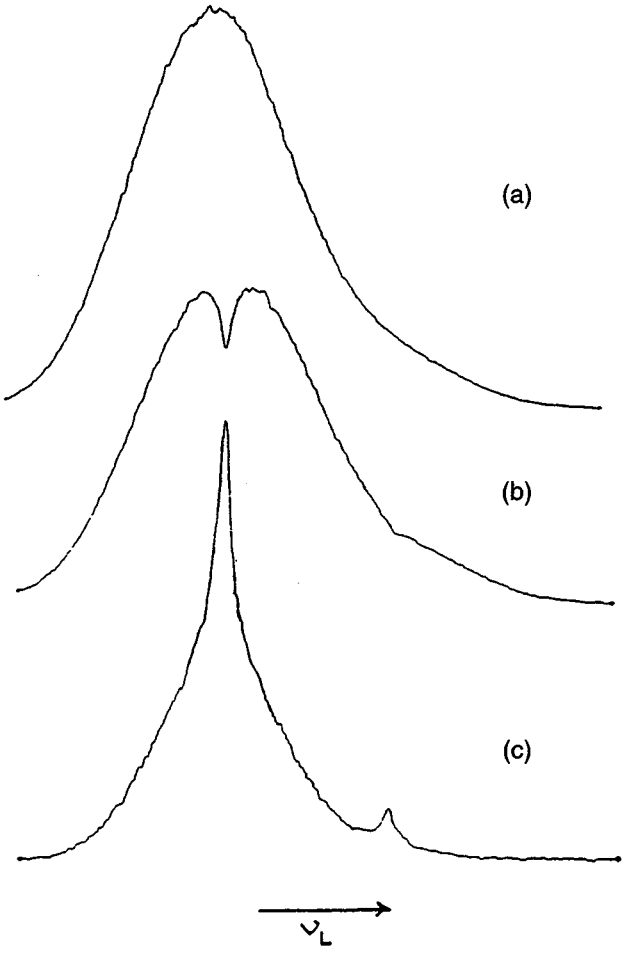


**FIG. 9.** Recording of the neon transition at 607.4 nm using a tunable single-mode dye laser. In (a), the line is recorded in presence of a single beam (Doppler broadened), while in (b), the effect of the saturation produced by the pump beam is visible within the Doppler profile as a homogeneous dip. (c) Doppler-free recording obtained by means of a phase-sensitive detection scheme.

scheme [Fig. 9(c)]; in this case, the lines from two isotopes are completely resolved, and their separation is about 1.7 GHz.

## 2.2 Intermodulated Spectroscopy

As we have seen in the preceding section, saturation spectroscopy monitors changes in the absorption of the probe beam caused by a pump beam. This can significantly limit the sensitivity when weak transitions are to be studied. In such cases it is better to use "transverse" detection schemes where different observables are detected, such as fluorescent, optogalvanic, and optoacoustic signals, which we treat in the following sections. For all these techniques the detected signal is over a zero ground, and this can offer orders of magnitude more sensitivity than absorption spectroscopy.

Intermodulated spectroscopy is a technique derived from saturation spectroscopy (Sorem and Schawlow, 1972) in which one of these transverse detection schemes is used. The basic principle is illustrated in Fig. 10. Here, the intensities of the pump ($I_{\text{pump}}$) and probe ($I_{\text{probe}}$) beams are of the same order of magnitude, and the beams are modulated at frequencies $f_1$ and $f_2$, respectively; i.e.

$$I_{\text{pump}} = I_0[1 + \cos(2\pi f_1 t)],$$
$$I_{\text{probe}} = I_0[1 + \cos(2\pi f_2 t)]. \tag{20}$$

The intensity of the fluorescent (or optogalvanic) signal $I_{fl}$ induced simultaneously by the two beams is

$$I_{fl} = CN_{\text{sat}}(I_{\text{pump}} + I_{\text{probe}}), \tag{21}$$

where $C$ is a constant that takes into account the transition probability and the detection efficiency, while $N_{\text{sat}}$ is the saturated population density of the lower level and can be written as

$$N_{\text{sat}} = N_0(1 - S_0) = N_0[1 - a(I_{\text{pump}} + I_{\text{probe}})], \tag{22}$$

$N_0$ being the unsaturated population density. By use of Eqs. (20) and (22), and assuming

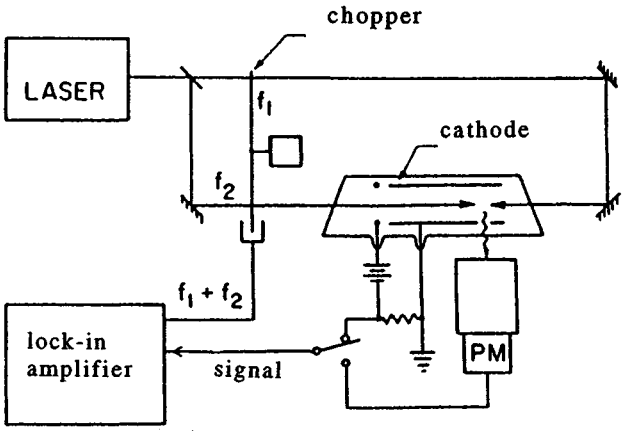


**FIG. 10.** Scheme for intermodulated spectroscopy. The sample consists of an electrical discharge, and the measurement is made by recording the fluorescence or optogalvanic signal at the sum or difference frequency produced by the interference of the modulation frequencies of the two laser beams.

$I_{pump} = I_{probe} = I_0$, it may readily be shown that Eq. (21) becomes

$$\begin{aligned} I_{fl} = {} & CI_0 a_0(\omega - \omega_0) \\ & \times [1 + 1/2 \cos(2\pi f_1 t) + 1/2 \cos(2\pi f_2 t)] \\ & + C' I_0^2 a_0(\omega - \omega_0)[1 + 1/4 \cos^2(2\pi f_1 t) \\ & + 1/4 \cos^2(2\pi f_2 t) + \cos(2\pi f_1 t) \\ & + \cos(2\pi f_2 t) + \cos(2\pi f_1 t) \cos(2\pi f_2 t)] \\ & \times L(\omega - \omega_0). \end{aligned} \tag{23}$$

This shows that the fluorescence signal is composed of several terms modulated at different frequencies. The first two terms depend linearly upon intensity: they are modulated at the frequencies $f_1$ and $f_2$, respectively, and originate from the pure interaction of each laser beam. Their dependence upon the laser frequency is, therefore, given by the Doppler-broadened absorption $a_0(\omega - \omega_0)$. The term $\cos(2\pi f_1 t) \cos(2\pi f_2 t)$, quadratically dependent upon intensity, is the most interesting because it gives rise to two terms modulated at the beat frequencies $(f_1 + f_2)$ and $|f_1 - f_2|$. These quadratic terms correspond to the simultaneous interaction of the two counterpropagating laser beams with the same velocity class of atoms, which occurs when the laser frequency is tuned near the center of the line. Therefore, if the detected fluorescence signal is processed by a lock-in amplifier set to one of the two beat frequencies, a Doppler-free signal will be obtained.

It is interesting to note that both saturation and intermodulated spectroscopies are based upon the simultaneous interaction of atoms with two counterpropagating laser beams, along whose axis the atoms have zero velocity; the interacting atoms may thus be compared to an atomic beam moving perpendicular to the laser beams. Nevertheless, there is an important difference with respect to a true atomic beam because, in a cell, atoms undergo collisions that, besides giving rise to pressure broadening, are also responsible for the broad residual pedestal shown in Fig. 10(c).

An unexpected signal is also observed when the laser frequency is far enough away from line center but still within the Doppler width. This effect is due to so-called velocity-changing collisions, which may be described simply as follows. When $\nu_1 \neq \nu_0$, the probe and pump beams interact with two symmetrically displaced velocity classes of atoms. Nevertheless, collisions tend to thermalize the velocity distribution, and atoms with a velocity $v$ "marked" by the pump beam can, after one or more collisions, acquire a velocity $-v$. If this occurs within the detection time, these atoms may thereby interact with both the pump and probe beams.

The Doppler-broadened pedestal depends upon several collisional parameters and the lifetimes of the levels involved. This contribution to the Doppler-free spectrum can be useful in learning about collisional physics itself but prevents full resolution of closely spaced spectral lines. In order to improve the resolution and sensitivity, other techniques are required.

### 2.3 Polarization Spectroscopy

Polarization spectroscopy is based on the light-induced birefringence and dichroism of an absorbing gas. These effects were first observed by Fornaca *et al.* (1963) using classical radiation sources; polarization spectroscopy using single-mode tunable lasers was demonstrated by Wieman and Hänsch (1976).

In a polarization spectroscopy experiment, the laser beam is split into two beams of different intensities, the pump beam being circularly polarized by means of a quarter-wave plate while the probe beam is polarized linearly. As with the previous Doppler-free techniques, the two beams pass in opposite directions through the sample cell. The transmitted probe beam passes through a high–extinction-ratio polarizer that is set to maximum extinction, before falling upon the detector.

The basic idea of polarization spectroscopy can be understood with the help of Fig. 11, which shows a transition between two levels having angular momenta of $J_1 = 2$ and $J_2 = 1$. Both levels are degenerate with $2J + 1$ Zeeman sublevels labeled with quantum number $m = -J \ldots +J$, describing the projection of $J$ along a quantization axis that, in our case, is the laser beam direction. Transitions $m'' \rightarrow m'$ follow the selection rule $\Delta m = \pm 1$ for right ($\sigma^+$) and left ($\sigma^-$) circularly polarized light. Thus, if the pump beam is $\sigma^+$ polarized only, some of the lower sublevels are partially depleted (the sublevels with $m = -2$, $-1$, and 0). The angular mo-

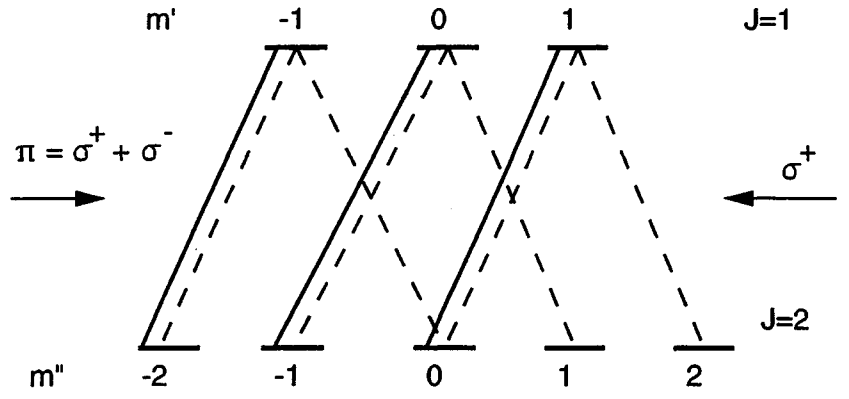


**FIG. 11.** The $\sigma^+$ pump beam induces transitions with $\Delta m_j = +1$ creating a birefringence in the gaseous sample. The birefrengence is monitored with a second counterpropagating beam (probe beam) normally extinguished between two crossed polarizers.

mentum of the light is hence transferred to the atomic sample, producing a nonuniform population of the $m$ sublevels, which corresponds to a macroscopic anisotropy of the sample. Such induced birefringence can be "read" by the linearly polarized probe beam, which may be considered to be a superposition of $\sigma^+$ and $\sigma^-$ circular polarizations. In the absence of the pump beam, and when the laser frequency is resonant with the transition under investigation, the intensity transmitted by the crossed polarizer is

$$I_{(\text{pump off})} = I_0(\chi + \theta^2 + b^2)\exp(-\alpha l), \qquad (24)$$

where $I_0$ is the probe beam intensity, $\chi$ is the finite extinction coefficient of the polarizer, $\theta$ is the angular deviation from orthogonality, and $L$ is the thickness of the sample. Finally, $b$ is a term that takes into account the residual birefringence introduced by stress induced in the windows of the cell.

When the laser frequency is tuned to within the homogeneous width of the line, the $\sigma^+$ and $\sigma^-$ components experience different absorption coefficients $\alpha_+$ and $\alpha_-$ and refractive indices $\eta_+$ and $\eta_-$ because of velocity-selective pumping by the $\sigma^+$ pump beam. As a consequence, after passing through the sample, the resulting probe polarization will generally be elliptical, with the minor axis rotated with respect to the transmission axis of the analyzer ($x$ axis in Fig. 12). In the limit of low saturation and a thin sample, it can be shown that the transmitted intensity $I$ after the crossed polarizer is

$$I = I_0\left[\chi + \theta^2 + b^2 - \left(\frac{\theta\Delta\alpha L x}{2(1+x^2)}\right) + \left(\frac{Lb\Delta\alpha}{2(1+x^2)}\right) + \left(\frac{(\Delta\alpha L)^2}{16(1+x^2)}\right)\right], \qquad (25)$$

where $x = (\omega - \omega_0)/\gamma$ is the laser detuning relative to the homogeneous width and $\Delta\alpha$ is the difference between the absorption coefficients of the $\sigma^+$ and $\sigma^-$ probe components. In Eq. (25), only $\Delta\alpha$ appears, because $\Delta\eta$ is related to $\Delta\alpha$ through the Kramers–Kronig dispersion relations.

Equation (25) shows the spectral profile of the polarization signal; it is given by a constant term $I_0(\chi + \theta^2 + b^2)$, a dispersion-shaped term, and a Lorentzian. By an appropriate choice of the experimental conditions, a pure Lorentzian or dispersive shape can be obtained.

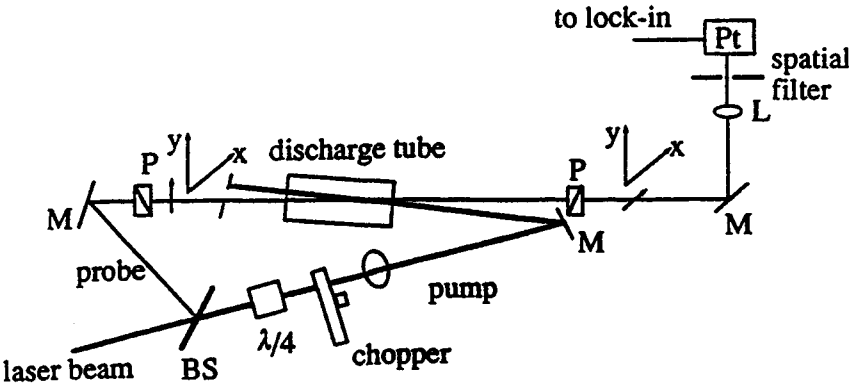


**FIG. 12.** Experimental arrangement for polarization spectroscopy.

In Fig. 13 are shown typical line shapes for the $^5S_2$–$^5P_3$ oxygen transition at $\lambda$ = 777.4 nm, obtained by polarization spectroscopy using a diode laser. Atomic oxygen was produced by dissociation in a radio-frequency discharge where molecular oxygen was present at trace levels. The two extreme regimes of symmetrical Lorentzian [Fig. 13(a)] and dispersive [Fig. 13(b)] shapes were achieved by setting the angle $\theta$ between the two polarizers to two different values. Narrower line shapes, down to one-half of the homogeneous width, can be achieved by recording the first derivative of the dispersion-shaped signal, as shown in Fig. 13(c) (the derivative of a line profile is simply obtained by modulating the laser frequency instead of the intensity). The "artificial" subnatural resolution reached in this way can provide some advantages for high-resolution spectroscopy or can be used to lock laser frequencies.

As we have already discussed, in saturation spectroscopy the atomic populations are probed and line shapes are affected by velocity-changing collisions that rethermalize the velocity distribution altered by the pump laser beam. In contrast, polarization spectroscopy probes the dichroism and birefringence originating from velocity-selective orientation of the atomic sample. Collisions do not usually conserve atomic angular orientation, and the recorded line shapes are unaffected by the residual Doppler background, so that the spectral resolution is further improved.

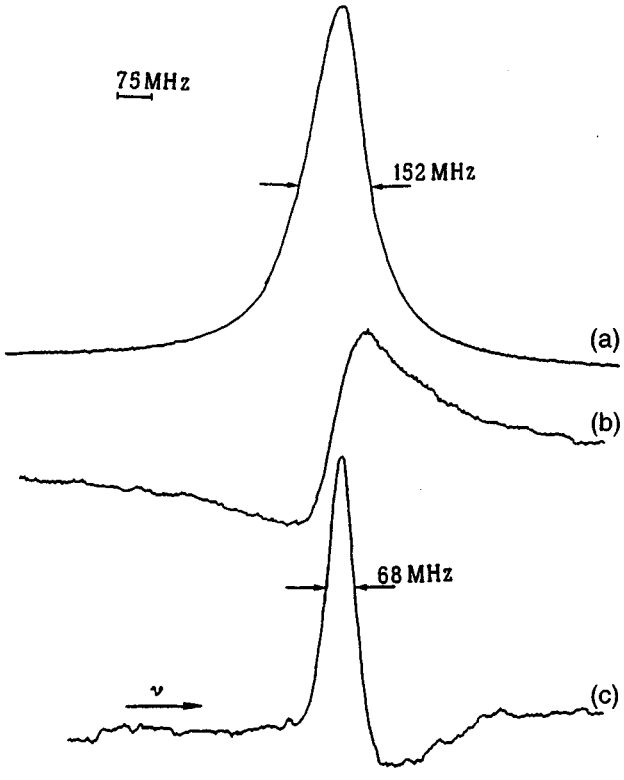


**FIG. 13.** Typical recording of the $^5S_2$–$^5P_3$ oxygen transition obtained with polarization spectroscopy by using a diode laser tunable around 777.4 nm. (a), (b) The extreme cases of Lorentzian and dispersive line shapes, respectively. (c) By modulating the laser frequency instead of the amplitude, the derivative of a Lorentzian shape is obtained. (From Gianfrani *et al.*, 1991.)

## 2.4 Velocity-Selective Optical-Pumping Spectroscopy

Polarization spectroscopy is a particular case of a more general class of Doppler-free techniques based on velocity-selective optical pumping (Pinard *et al.*, 1979). The population distribution among the Zeeman sublevels can be expressed in terms of a power series in $m$ ($m = -|J| \ldots +|J|$):

$$D = \sum_k \sum_m N_m m^k, \tag{26}$$

where $N_m$ is the probability of occupation of the sublevel $m$. The zero-order term ($k = 0$) is the population $P$ and is given by

$$P = \sum_m N_m, \tag{27}$$

while the first ($k = 1$) and second ($k = 2$) orders are the orientation $O$ and alignment $A$ expressed by

$$O = \sum_m N_m m, \tag{28}$$

$$A = \sum_m N_m m^2 - \tfrac{1}{3}J(J+1). \tag{29}$$

Generally, the population distribution will be a superposition of orientation and alignment. Nevertheless, for particular light polarizations, a pure orientation or alignment can be achieved. For instance, pure orientation is created with circularly polarized light [atoms accumulate in the sublevels with $m = J(\sigma^+)$ or $m = -J(\sigma^-)$], while pure alignment may be induced using linearly polarized light.

If the polarization rather than the amplitude of the pump beam is modulated, the orientation or alignment may be monitored.

In the orientation modulation technique, for instance, an electro-optic modulator (EOM) is square-wave modulated to provide an alternating $\sigma^+/\sigma^-$ polarization of the pump beam while the probe beam is circularly polarized. Alternatively, for alignment detection, the EOM provides a polarization that alternates between vertical and horizontal (see Fig. 14).

Typical recordings obtained using orientation and alignment detection are shown in Fig. 15 for the $^5S_2$–$^5P_3$ oxygen transition (de Angelis *et al.*, 1991). It may be seen that, in the case of alignment detection, atoms undergoing velocity-changing collisions become depolarized and do not contribute to the residual Doppler pedestal.

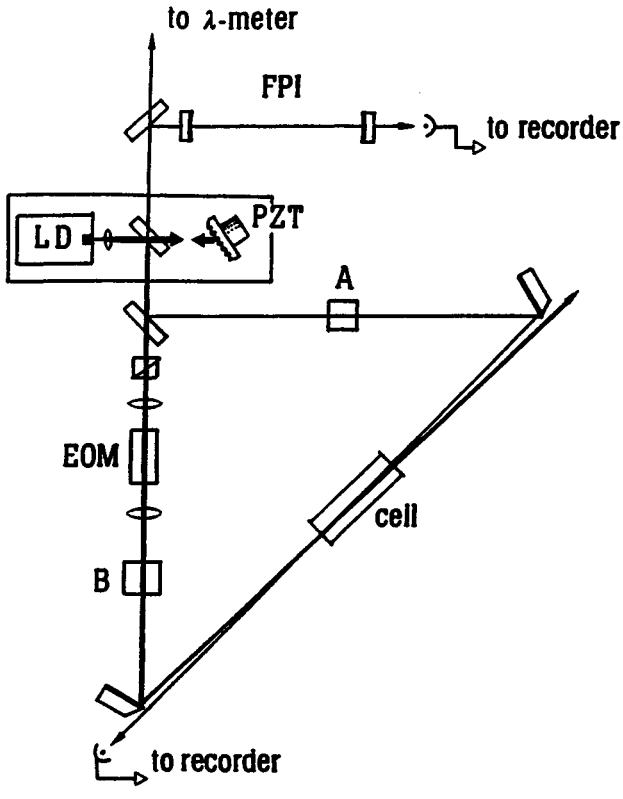


**FIG. 14.** Experimental setup to monitor alignment and orientation. A and B are optical components according to the observable to be detected (see following description). The laser diode (LD) is mounted in an extended cavity controlled by a piezoelectric crystal (PZT), and its frequency is monitored by a Fabry–Pérot interferometer (FPI). The polarization of the pump beam is modulated by means of an electro-optic modulator (EOM). In order to monitor orientation, the EOM produces an alternating $\sigma^+$–$\sigma^-$ polarization of the pump, while A is a linear polarizer followed by a quarter-wave retarder, and B is absent. For alignment detection, the EOM renders the polarization alternately vertical and horizontal. A is a linear polarizer, and B is again absent. To monitor the population (saturation spectroscopy), the EOM may be used like a chopper to modulate the intensity, with linear polarizers at A and B. (From de Angelis *et al.*, 1991.)

## 2.5 Polarization-Intermodulated Excitation Spectroscopy (POLINEX)

The intermodulated technique was improved by Hänsch and co-workers by modulating the polarizations, rather than the amplitudes, of the counterpropagating beams. This method is referred to as the polarization-intermodulated excitation, or POLINEX (Hänsch and Toschek, 1970). When the laser is tuned to within the homogeneous width, the total excitation rate is still modulated at the sum or difference frequency, but the combined absorption of the two beams in general depends upon their relative polarization. When the two laser beams share the same polarization, they will be preferentially absorbed by atoms of the same orientation, with a resultant increase in saturation; when the polarizations are different, the two beams will tend to interact with atoms of different orientation and, as a consequence, the total saturation decreases.

In addition to the density-matrix formalism used by Hänsch and Toschek (1970), POLINEX may be described using a simpler rate equation approach (Teets *et al.*, 1977). If optical pumping effects are neglected, and in the approximation of a Doppler width much larger than the homogeneous width, it is possible to obtain an analytical expression for the Doppler-free line shape.

There is a substantial difference between POLINEX and polarization spectroscopy, although in both schemes the signal is derived from the orientation and alignment. Indeed, in polarization spectroscopy, the signal depends upon both dichroism and birefringence induced by the absorbed light, and as a consequence the line shapes are usually asymmetric. In contrast, POLINEX spectroscopy detects only the dichroism, and the line shapes are symmetric.

One advantage of POLINEX over intermodulation spectroscopy is that the crossover signals are frequently of opposite signs and can therefore be easily distinguished even in complicated spectra. It should be noted, however, that if amplitude modulation is unintentionally present together with

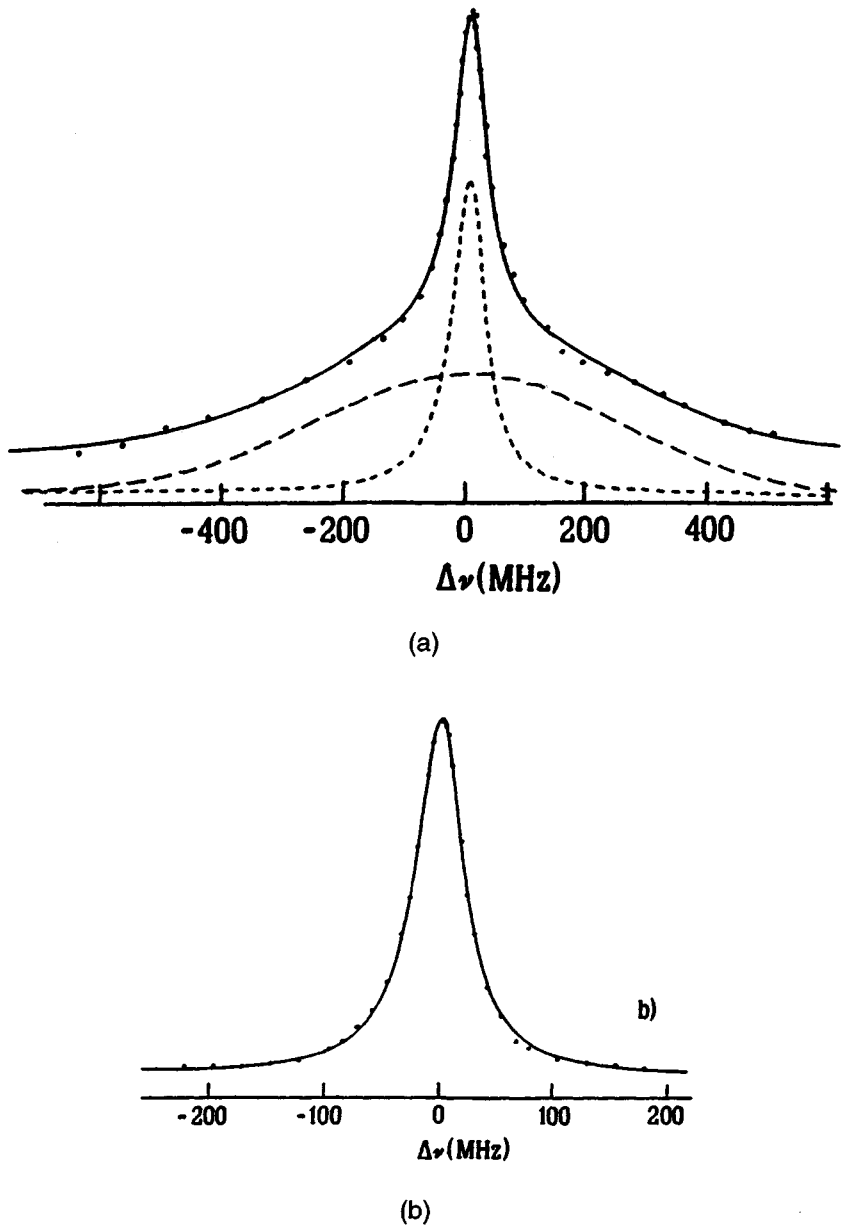


**FIG. 15.** Comparison between velocity-selective (a) orientation and (b) alignment detection of the $J = 2$–$J' = 3$ transition of oxygen at 777.4 nm. The line shape (a) is given by the superposition of a Lorentzian curve and a Gaussian curve due to the velocity-changing collisions.

the polarization modulation, spurious signals can be produced.

A comparison between intermodulation and POLINEX spectroscopy is shown in Fig. 16 for the copper transition at 578.2 nm. Copper vapor was produced by sputtering in a hollow-cathode discharge. It is interesting to note that in POLINEX spectroscopy the residual Doppler background is absent. This is a consequence of the fact that atomic orientation and alignment are not conserved during collisions. Another difference between the two spectra is the absence in the POLINEX spectrum of transitions starting from levels with $F = 0$, which cannot be oriented.

The various techniques previously discussed, combining saturation and optical activity, have been extensively used in many spectroscopic applications. The ability to deplete selectively a specified rotational–vibrational level by optical pumping can be used to simplify complex molecular spectra. This method, named polarization labeling spectroscopy, uses two lasers. The first laser beam is again split into two counterpropagating beams (pump and probe) and locked to the center of the polarization signal of a transition $(\nu'',J'') \rightarrow (\nu',J')$. The second laser acts as a probe laser: it passes collinearly with the probe beam of the first laser through the sample cell, after which the two probe beams are separated and individually

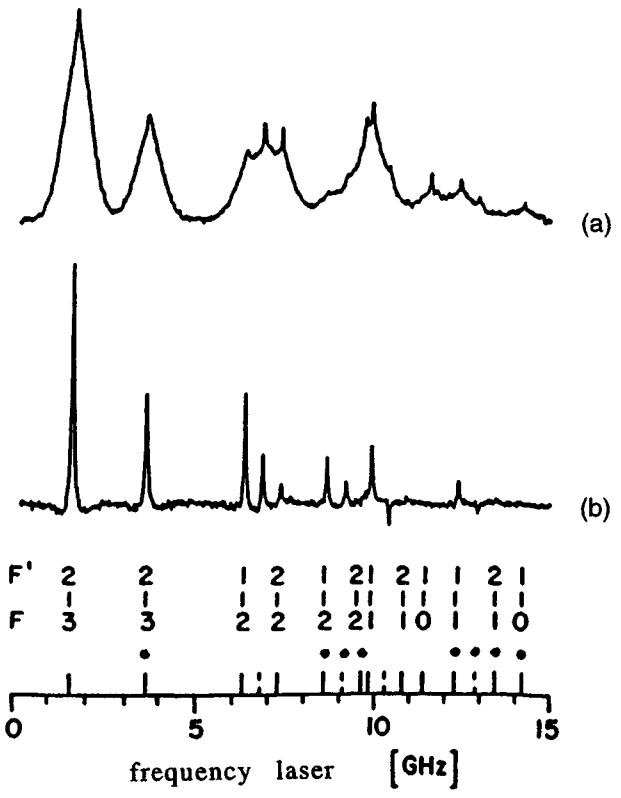


**FIG. 16.** Comparison between (a) intermodulated spectroscopy and (b) POLINEX detection of the Cu transition at 578.2 nm. Lines in the spectrum (a) are broader than in the spectrum (b) because they are affected by velocity-changing collisions.

detected. When the frequency of the probe laser is tuned, a polarization signal is produced every time the probe laser hits a transition that shares a common level with the pump transition $(\nu'',J'') \rightarrow (\nu',J')$.

## 2.6 Multiphoton Spectroscopy

In many spectroscopic techniques, two or more photons are involved. As a simple example, we consider the case where a level $b$ is selectively excited by a first laser of frequency $\omega_1$. This level represents a platform from which a second photon can be absorbed to reach a higher excited level $c$. Such a two-step excitation approach has been extensively used for many double-resonance schemes where the two photons lie in a wide spectral region (radio frequency, microwave, infrared, and visible). We now, however, focus our attention on a class of multiphoton spectroscopic techniques (Bruzzese *et al.*, 1989) in which the jump from the lower level $a$ to the excited level $c$ occurs through the absorption of two or more photons (see Fig. 17) without intermediate levels. This possibility was predicted upon the introduction of quantum mechanics, and one of the first examples was represented by the Raman process, in which a photon of frequency $\omega$ is absorbed and another photon of lower (Stokes process) or higher (anti-Stokes process) frequency $\omega'$ is emitted, with consequent excitation of a different state of the atomic or molecular system. In the low-intensity (spontaneous emission) regime, this process is linear.

The first theoretical study considering the possibility of inducing transitions through two-photon absorption was performed in 1931 by Goeppert-Mayer (1931). Her idea was, at the time, experimentally unfeasible

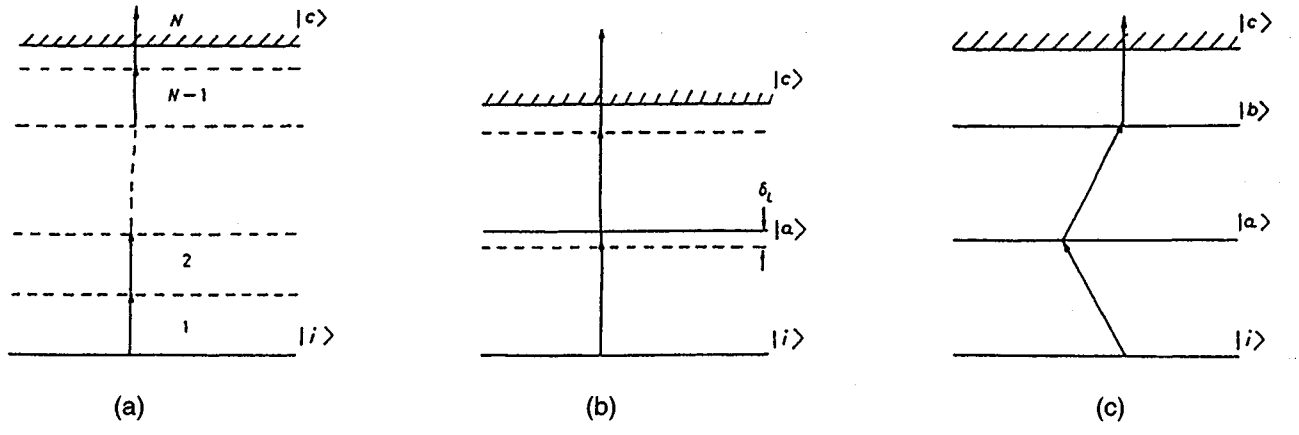


**FIG. 17.** Schematic representation of multiphoton processes: (a) nonresonant, (b) quasiresonant, and (c) multistep excitation. Dashed lines represent virtual states.

because of the low intensity of the available radiation sources: The higher-order terms of the perturbation theory, which describe multiphoton processes, become relevant only when the intensity of the electromagnetic field is sufficiently large with respect to the Coulombian atomic field. Since then, however, the development of maser and, successively, laser sources has offered the possibility of carrying out two-photon and more generally multiphoton processes, thereby providing powerful tools to investigate a new class of phenomena.

The first experimental evidence of multiphoton processes was produced by Brossel *et al.* (1954), who used an intense radio-frequency field, and by Battaglia *et al.* (1959) with microwaves. In 1962, just two years after the operation of the first laser, Abella (1962) observed two-photon absorption between the $6^2S_{1/2}$ ground state and the $9^2D_{3/2}$ state of cesium by tuning a $Q$-switched ruby laser at $\lambda = 693.5$ nm by temperature control of the active medium. However, most spectroscopic applications based on multiphoton absorption followed the later development of pulsed tunable dye lasers.

The main advantages offered by two- (or more) photon processes are the following:

1. The selection rules for transitions induced by multiphoton absorption are different from those for single-photon processes. For instance, in the electric dipole approximation, two-photon transitions can occur only between levels having the same parity. As a consequence, it is possible to induce transitions from the ground state not otherwise feasible with single-photon absorption.
2. Two-photon excitation can be achieved by using visible or ultraviolet radiation instead of the higher-frequency radiation required for an equivalent single-photon transition.
3. If the two photons are absorbed from opposite directions, the first-order Doppler effect can be removed, and the spectral resolution thus improved.

**2.6.1 Selection Rules for Two-Photon Transitions** In the electric dipole approximation, the interaction Hamiltonian acts only on the orbital quantum numbers of the electrons. If we consider polarized light ($\sigma^+$, $\sigma^-$, and $\pi$), the interaction components are transformed as the component of an irreducible tensor of rank one $T_1^{(q)}$, with $q = +1$ for $\sigma^+$ polarization, $q = -1$ for $\sigma^-$ polarization, and $q = 0$ for $\pi$ polarization. Applying such an operator changes the angular momentum by 1. As a consequence, applying the operator twice, we have

$$\Delta L = 0, 2,$$
$$\Delta m_L = q_1 + q_2. \tag{30}$$

In the presence of a strong external magnetic field, $L$ and $S$ are completely uncoupled (the Paschen–Back effect), and the quantum numbers of spin cannot change:

$$\Delta m_s = \Delta m_l = 0, \tag{31}$$

while in the contrasting case in which the spin-orbit interaction and hyperfine interaction are not negligible, it can be shown from the Wigner–Eckart theorem that

$$|\Delta F| \leq 2; \qquad \Delta m_F = q_1 + q_2. \tag{32}$$

We consider two cases of particular importance to many spectroscopic applications. The first concerns transitions between two $s$ states: the electronic and nuclear spins can be modified only through coupling with the orbital angular momentum and, since $L = 0$, we have $\Delta F = \Delta m_F = 0$. The second case concerns two states with the same total angular momentum $J$. If $J = 0$ or $\frac{1}{2}$, only a scalar operator can couple these two states, and we again have $\Delta F = \Delta m_F = 0$.

**2.6.2 Transition Probabilities and Line Shapes for Two-Photon Transitions** We suppose that an atom having velocity $v$ interacts with two laser beams of the same frequency $\omega$ and wave vectors $\mathbf{k}_1$ and $\mathbf{k}_2$, respectively. If the intensities of the two counterpropagating beams are the same ($I_1 = I_2 = I$), then the two-photon transition rate from a state $|a\rangle$ to a state $|b\rangle$ can be calculated from second-order perturbation theory:

$$P_{ab} \propto \left[\frac{4\gamma_{ab}}{(\omega_{ab} - 2\omega - k_1 v + k_2 v)^2 + (\gamma_{ab}/2)^2} + \frac{\gamma_{ab}}{(\omega_{ab} - 2\omega - 2k_1 v)^2 + (\gamma_{ab}/2)^2} + \frac{\gamma_{ab}}{(\omega_{ab} - 2\omega + 2k_2 v)^2 + (\gamma_{ab}/2)^2}\right] \times \left|\sum_{\kappa} \frac{R_{a\kappa} R_{\kappa b}}{\omega - \omega_{a\kappa}}\right|^2 I^2, \quad (33)$$

where $\gamma_{ab}$ is the homogeneous linewidth of the transition $a$–$b$ and where $R_{ij}$ are the matrix elements

$$R_{ij} = \langle i|r|j\rangle. \quad (34)$$

For the particular case of two counterpropagating beams ($\mathbf{k}_1 = -\mathbf{k}_2$), the first term of the transition probability [Eq. (33)] is not affected by the velocity distribution of the atoms. Indeed, since the laser frequency $\omega$ will be shifted by $+kv$ and $-kv$, respectively, for the two beams, the two Doppler shifts will exactly compensate, and we have

$$E_b - E_a = \hbar(\omega + kv) + \hbar(\omega - kv) = 2\hbar\omega_{ab}. \quad (35)$$

In other words, when the frequency of the laser is resonant [$\hbar\omega = (E_a - E_b)/2$], all of the atoms will undergo the two-photon transition with the same probability, independent of their velocities.

The second term of Eq. (34) represents the absorption of two photons from the same laser beam. In this case, for a given laser frequency $\omega$, there is a group of atomic velocities that, because of the Doppler effect, will see the frequency resonant with the transition $a \rightarrow b$:

$$E_b - E_a - 2\hbar\omega = \pm\hbar kv. \quad (36)$$

The line shape of a two-photon transition is therefore given by the superposition of two curves: a Lorentzian curve, representing the Doppler-free term, and a Gaussian curve that takes into account the velocity dependence of the second term of Eq. (34) (see Fig. 18). If the polarizations of the two counterpropagating laser beams are the same, it can be shown that the area under the Lorentzian curve is twice that under the Gaussian curve. In order to improve the resolution, the Gaussian background can be removed with a suitable choice of polarization of the two laser beams.

Doppler-free two-photon spectroscopy was first proposed by Vasilenko *et al.* (1970) at Novisibirsk and demonstrated experimentally by Cagnac *et al.* (1973) at Paris and Bloembergen *et al.* (1974) at Harvard. The investigated atom was chosen to be sodium for its favorable energy level scheme, the two-photon transitions $3S$–$5S$ at 602.23 nm and $3S$–$4D$ at 578.73 nm both being in a spectral range where tunable dye lasers are easily available. Moreover, for both transitions, the intermediate $3P$ level makes the transition probabilities relatively large. Figure 19 shows a typical recording for the transition $3S_{1/2}$–$5S_{1/2}$, where the two-photon absorption was

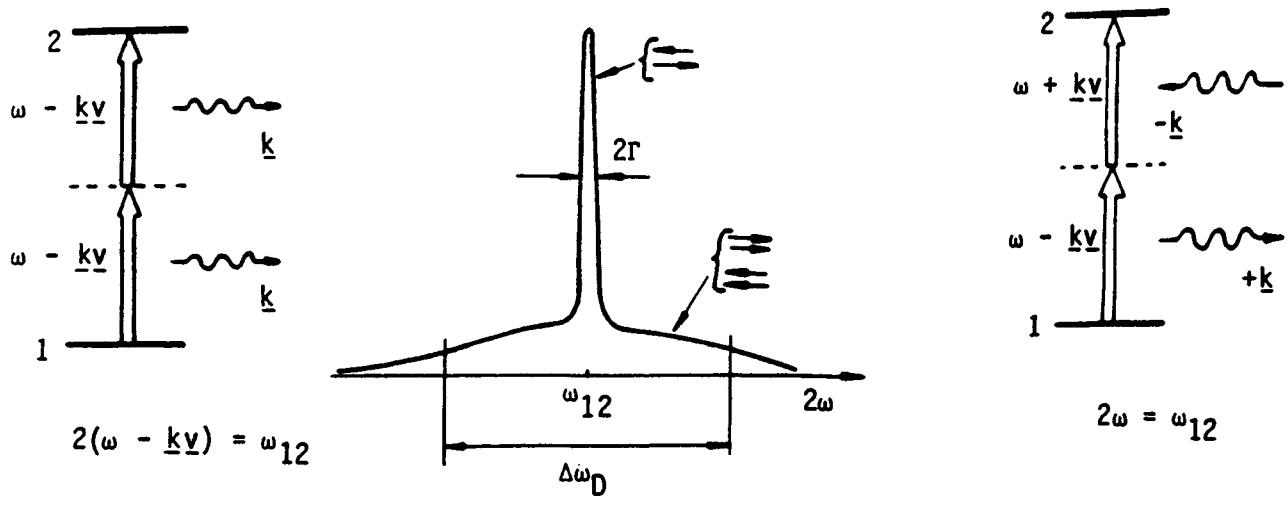


**FIG. 18.** Typical Doppler-free two-photon spectrum. The residual Doppler background is due to the absorption of two photons traveling in the same direction.

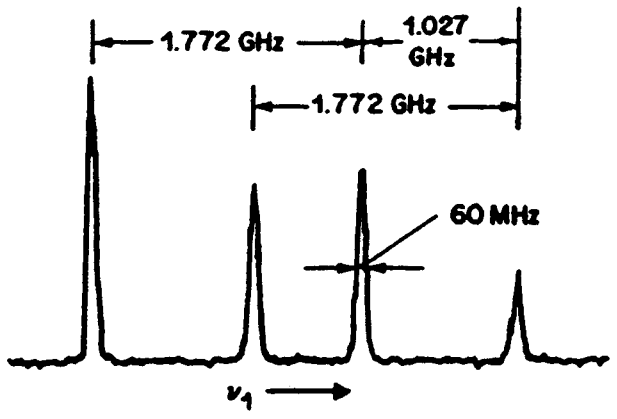


FIG. 19. The excitation spectrum for two-photon excitation of the $4D$ level in sodium. The peaks correspond to the hyperfine transitions between the ground state $3S_{1/2}(F = 1, 2)$ and the final state $4D_{3/2,5/2}$. The 1.772-GHz splittings are due to the hyperfine splitting of the ground state, while the 1.027-GHz splitting reflects the $4D$ fine structure. (From Bjorkholm and Liao, 1974).

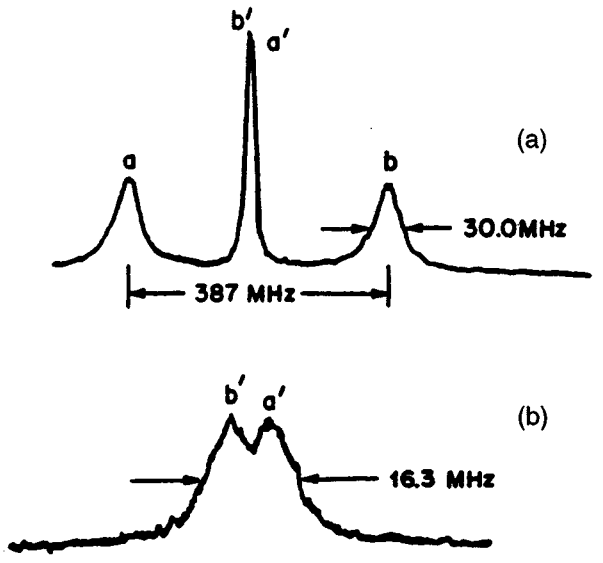


FIG. 20. Typical two-photon spectra in sodium with one laser resonant with the $3S$–$3P_{1/2}$ transition and the second swept around the $3P$–$4D$ transition. The two laser beams copropagate in (a) and are counterpropagating in (b). (From Bjorkholm and Liao, 1976).

monitored by observing cascading fluorescence from the $4P$ to the $3S$ state at 330.3 nm. This demonstrates another advantage of this technique, whereby an induced transition can be studied by detecting fluorescence at a wavelength quite different from that of the excitation radiation. Both the lower $3S_{1/2}$ and upper $5S_{1/2}$ levels consist of two hyperfine levels ($F = 3$ and 4). Because of the two-photon selection rules, only hyperfine transitions with $\Delta F = 0$ can be induced, giving rise to two spectral components separated by the combined hyperfine splittings of the lower and upper levels. As is shown in Fig. 20(a), the two hyperfine components, separated by less than the Doppler width, are not resolved if copropagating beams are used. A higher resolution is achieved using two counterpropagating beams, as shown in Fig. 20(b).

Like saturation spectroscopy, Doppler-free two-photon spectroscopy has been used to investigate fine effects in the structure of atoms and molecules, such as isotope shifts, hyperfine splittings, Zeeman and Stark effects in weak fields, and collisional broadenings and shifts. It is interesting to note that two-photon signals are not significantly lower than those obtained in saturation spectroscopy, especially if an intermediate level is present midway between the initial and final states. This is easily explicable if we recall that in saturation spectroscopy the signal is produced by atoms having zero velocity along the laser-beam direction, while in two-photon spectroscopy all atoms contribute to the signal. This feature is important, for it means that two-photon transitions can be investigated using cw lasers of relatively low intensity.

A generalization of the opposing-beam technique to demonstrate resonant enhancement of the two-photon transition probability has been carried out by Bjorkholm and Liao (1976) in sodium vapor. Their experiment was performed with use of two single-mode dye lasers operating at different frequencies. One laser produced a fixed frequency matched to the $3S$–$3P$ transition, while the second laser was tuned around the $3P$–$4D$ transition. Because the frequencies of the two lasers were not equal, Doppler effects were not in this case completely removed, and the residual Doppler effect made it impossible to be simultaneously resonant with all the velocities of the Maxwellian thermal distribution. Consequently, the use of two unequal frequencies results in a decrease in the excitation efficiency. To demonstrate resonant enhancement, Bjorkholm and Liao used different wavelengths for the first laser and tuned the second around the two-photon resonance ($E_b - E_a = \hbar\omega_1 + \hbar\omega_2$). As is shown in Fig. 21, when the first laser ap-

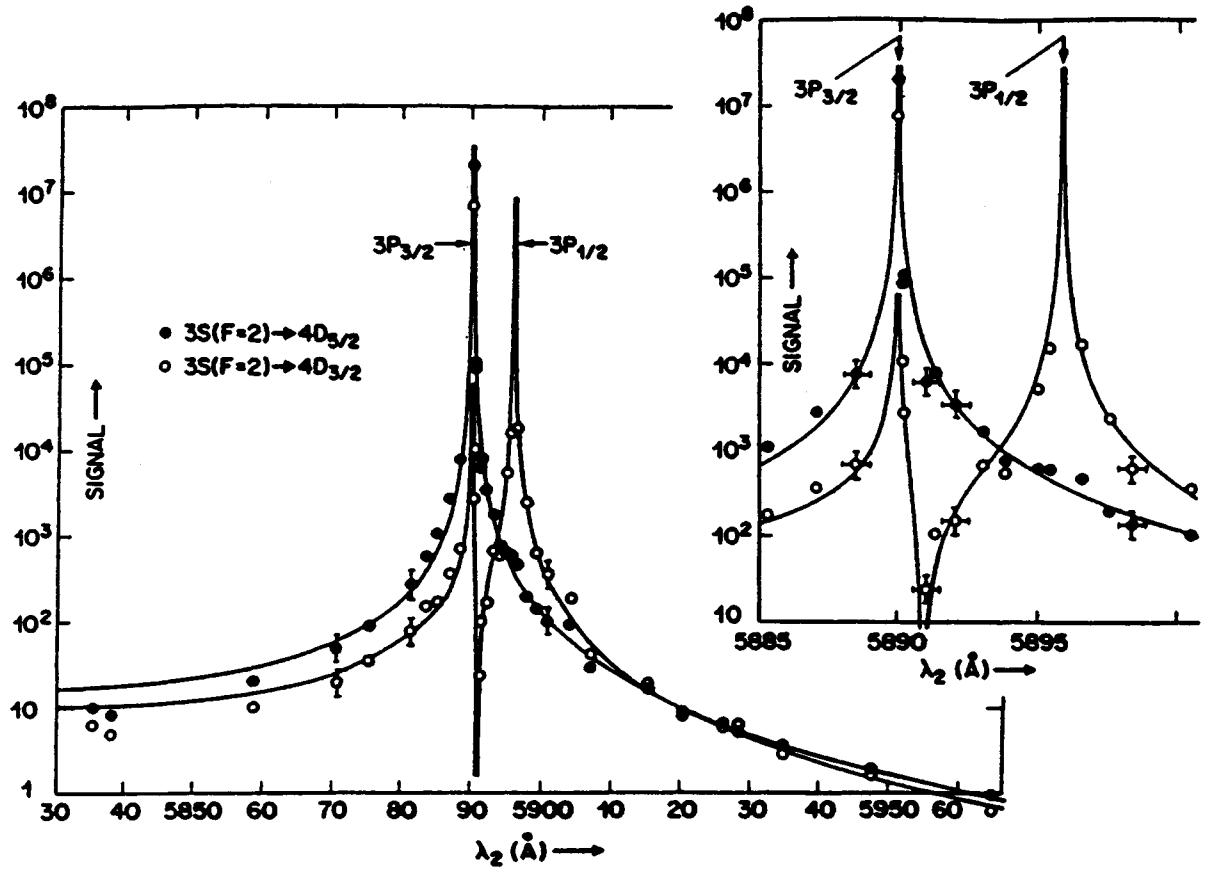


FIG. 21. Normalized two-photon transition rates for the $3S(F = 2)$–$4D_{5/2}$ and $3S(F = 2)$–$4D_{3/2}$ transitions as a function of the laser detuning (from Bjorkholm and Liao, 1976).

proaches the 3S–3P resonance, the signal increases by seven orders of magnitude. It is also interesting to note that for frequencies between those of the two fine structure components $3P_{1/2}$ and $3P_{3/2}$, the signal decreases because of quantum interference effects.

**2.6.3 Doppler-Free Multiphoton Transitions** The Doppler effect can also be canceled when three or more photons are absorbed if a suitable geometry of laser beams is used. Consider the case of an atom irradiated by different beams having wave vectors $\mathbf{k}_i$. The Doppler shift for each interaction is $\mathbf{k}_i \cdot \mathbf{v}$, and hence, if the atom absorbs $n$ photons, the total Doppler shift is given by $\Sigma_i \mathbf{k}_i \cdot \mathbf{v}$, where the sum extends to all $n$ absorbed photons. So, if

$$\sum_i \mathbf{k}_i = \mathbf{0}, \tag{37}$$

the $n$-photon transition is unaffected by the Doppler effect. In the particular case of photons of the same frequency, if $n = 2$, the two laser beams are counterpropagating ($\mathbf{k}_1 = -\mathbf{k}_2$), while for $n = 3$, the laser beams are directed along the bisectors of an equilateral triangle.

The first Doppler-free three-photon experiment, in which two photons were absorbed and one emitted, was made by Grynberg, Biraben, Bassini, and Cagnac.

**2.6.4 Applications of High-Resolution Spectroscopic Techniques to the Hydrogen Atom: Lamb-Shift and Rydberg-Constant Measurements** Spectroscopic investigations of atomic hydrogen allow the testing of fundamental physical theory and the measurement of physical constants, with high accuracy. Doppler-free two-photon spectroscopy has been used by several groups to measure the Rydberg constant and to determine the Lamb shifts of the hydrogen energy levels accounted for by quantum electrodynamics.

The Rydberg constant is of particular importance because it is composed of only fundamental constants ($R_\infty = me^4/8\epsilon_0^2 h^3 c$), so that a very precise measurement of $R_\infty$ allows the consistency of other constants to be

checked. The Rydberg constant can be determined by measuring the energy separation between two levels having different principal quantum numbers. $R_\infty$ is related to these separations through the Bohr formula, with corrections for the isotope shift, Dirac fine-structure effects, and quantum-electrodynamical radiative effects.

Figure 22 shows a saturation spectrum of the Balmer-$\alpha$ line of atomic hydrogen produced in a gas discharge. Thanks to the high resolution offered by saturation spectroscopy, the separation between the $2S_{1/2}$ and $2P_{1/2}$ levels (Lamb shift) was thus determined. Furthermore, absolute wavelength measurements of the strong $2P_{3/2}$–$3D_{5/2}$ component provided a new and more accurate value of the Rydberg constant. Nevertheless, the accuracy achievable in such experiments is generally dependent upon the characteristics of the atomic sample; indeed, a gas discharge introduces further broadenings and shifts of atomic lines due to collisions with other atoms and electrons.

Atomic beams would, on the other hand, present an ideal atomic sample if collisions and other perturbations could be kept to negligible levels and if first-order Doppler broadening could be eliminated. To this end, the group of Lichten at Yale performed an optical study of hydrogen very similar to the historic experiment by Lamb at radio frequencies (Amin *et al.*, 1981). Molecular hydrogen was dissociated by means of a hot wire, and the metastable 2S level was populated through collisions with a transverse electron beam. The atomic beam then interacted with a laser beam of low intensity. Absorption of the laser beam was monitored by detecting a variation in the flux of metastable atoms after the interaction with the laser beam. From an absolute wavelength measurement, Lichten derived one of the most accurate values of the Rydberg constant, $R_\infty = 109\,737.315\,73(3)\ \mathrm{cm}^{-1}$.

Atoms with a single optical electron have also been used to determine the Rydberg constant. The idea is to investigate highly excited levels (Rydberg states) in which electrons experience a hydrogen-type Coulomb field. The advantage offered by this approach is that lasers with high spectral purity are unnecessary because the energy difference between closely spaced Rydberg levels corresponds to radiation wavelengths in the submillimeter range.

The first excitation of the $2s$ level by two-photon absorption was performed by Hänsch and co-workers (1975, 1977) at Stanford. The two-photon $1S$–$2S$ transition is particularly difficult because, in contrast to the $3S$–$5S$ transition in sodium, no intermediate levels are present. Furthermore, the 243-nm laser radiation required for this experiment is in a difficult spectral region and could be produced only by frequency doubling a 486-nm pulsed dye laser by means of a lithium fluoride nonlinear optical crystal. The two-photon transition was observed through collision-induced fluorescence on the Lyman-$\alpha$ ($2P$–$1S$) transition at 121 nm. Frequency calibration was performed by sending part of the laser at 486 nm into a second discharge cell and observing the saturated spectrum of the Balmer-$\beta$ line. In absence of the Lamb shift, the frequency of the $1S$–$2S$ transition should be four times that of the $2S$–$4P$ line. The frequency difference between the two resonances (see Fig. 23) is thus determined by the Lamb shifts of the $1S$ and $2S$ states. Using a previously measured value of the $2S$ Lamb shift, the Lamb shift of the ground state was determined to be 8151(30) MHz for hydrogen and 8177(30) MHz for deuterium.

The first version of the $1S$–$2S$ two-photon measurement used pulsed lasers, and the linewidth of the observed transition was thus limited by the broad spectral width of these lasers. More recently, Hänsch *et al.* have investigated the same transition with much improved resolution by combining cw lasers with Fabry–Pérot built-up cavities.

## 3. HIGH-SENSITIVITY LASER SPECTROSCOPY

Laser radiation has been used extensively in spectroscopy to achieve not only high resolution but also high sensitivity, in order to investigate very weak transitions or to monitor species present at trace level.

The absorption coefficient $\alpha$ is related to microscopic parameters of the investigated atomic or molecular line by the relation

$$\alpha = [2\pi^2|\mu|^2\nu_{12}(N_1 - N_2)/3\eta\epsilon_0 ch]g(\Delta\nu), \quad (38)$$

where $\nu_{12}$ is the frequency of the transition, $\mu$ is the dipole moment of the transition, $\eta$ is

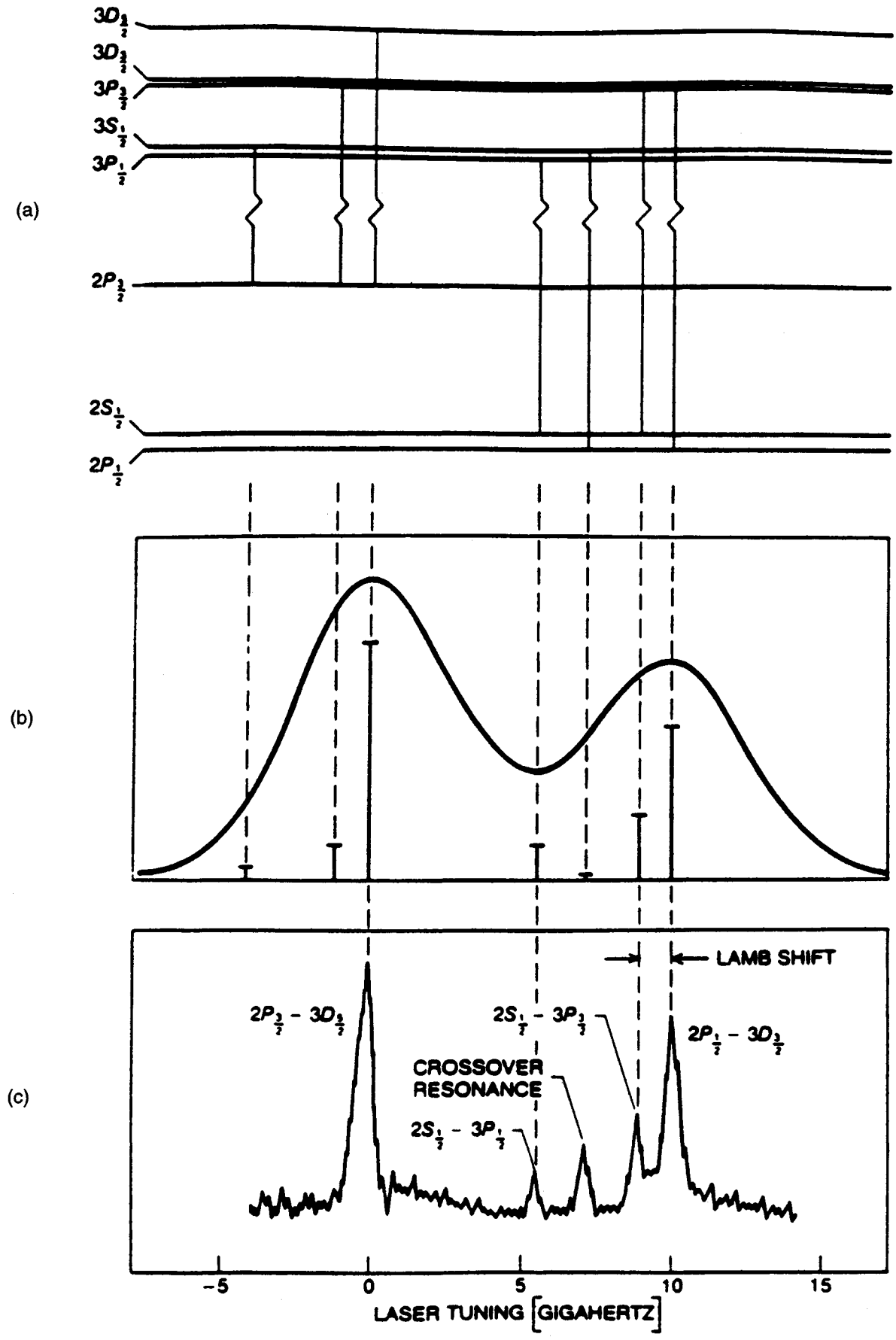


**FIG. 22.** Balmer-$\alpha$ line of atomic hydrogen: (a) energy levels with fine-structure transitions, (b) Doppler-limited emission line profile, and (c) saturation spectrum with optically resolved Lamb shift (from Hänsch, *et al.*, 1975b).

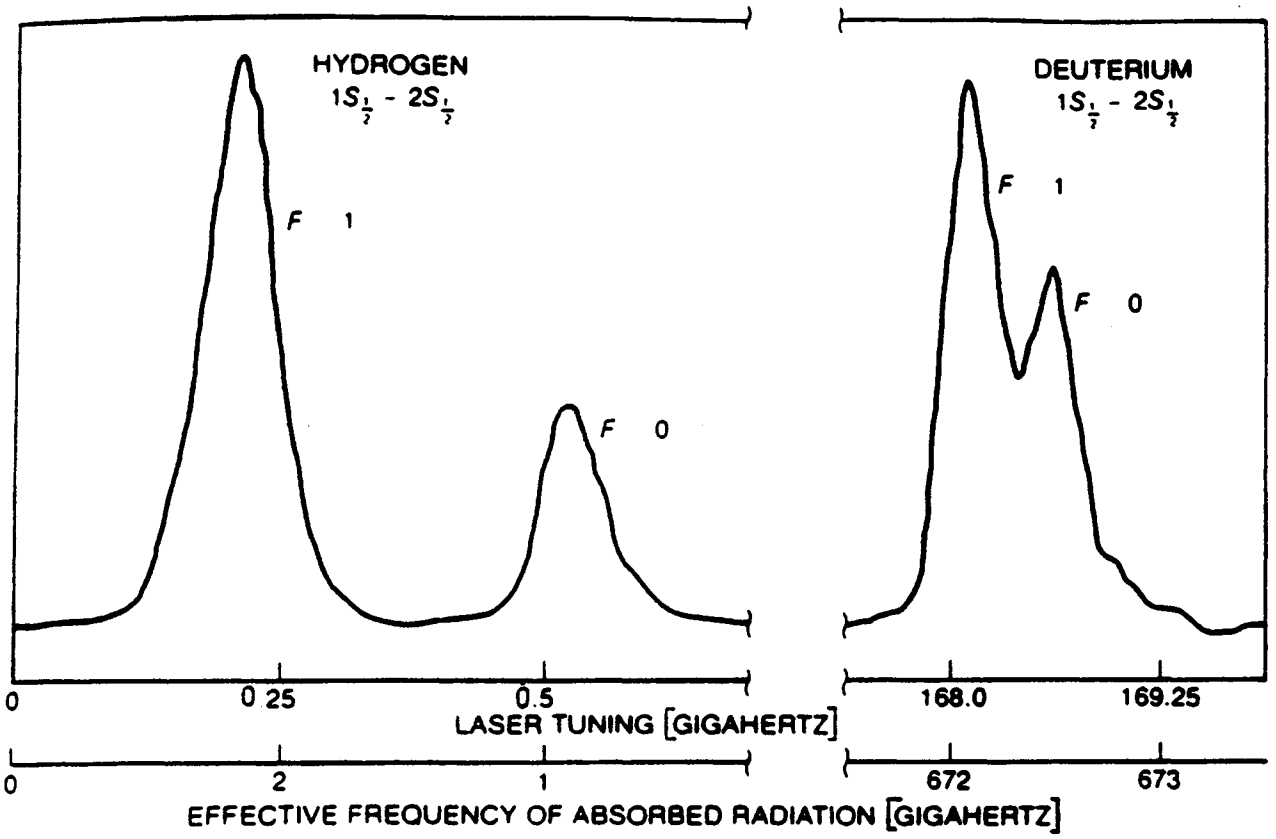


**FIG. 23.** Doppler-free two-photon spectrum of the 1*s*–2*s* transition of (a) atomic hydrogen and (b) deuterium (from Hänsch, *et al.*, 1975b).

the refractive index, and $g(\Delta\nu)$ is the line shape. To determine $\alpha$, we use the well-known Beer law, which describes the radiation absorbed by a length $L$ of the sample:

$$I(L) = I(0)\exp[-\alpha L]. \tag{39}$$

In the case of weak absorption, $\alpha L \ll 1$, Eq. (39) can be approximated by the first-order power series

$$I(L) = I(0)(1 - \alpha L). \tag{40}$$

Hence, the absorption coefficient can be determined from the fractional loss of the incident intensity:

$$\alpha L = [I(0) - I(L)]/I(0). \tag{41}$$

For weak absorption, however, this method cannot be very accurate because it measures small differences above a large background, and the minimum detectable absorption is thus limited by the amplitude fluctuations of the radiation source.

The advent of lasers has unleashed a wide variety of spectroscopic techniques that have increased the sensitivity enormously, allowing the detection of even a single atom. In the following section, we discuss some of these techniques.

The first approach is based upon the modulation of the laser frequency at a frequency $f$. If the amplitude of the modulation is sufficiently small (with respect to the width of the investigated line) and the transmitted radiation is detected with a lock-in amplifier tuned to the same modulation frequency $f$, the recorded signal is proportional to the derivative of the absorption spectrum. The advantage of this phase-sensitive method of detection is to restrict the noise to a narrow band centered around the modulation frequency $f$. In terms of the signal-to-noise ratio, frequency modulation is more sensitive than amplitude modulation because the frequency-independent background due to light scattered from cell windows etc. is blocked. We note that in some applications it may be more practical to modulate the frequency of the absorption curve rather than the laser, as is the case, for example, with intracavity magnetic resonance spectroscopy.

Other more sensitive methods make use of observations related to the energy absorbed rather than the difference in that transmitted $[I(0) - I(L)]$. Induced fluorescence, for instance, is proportional to the number of photons absorbed and provides a very sensitive detection scheme (excitation spectroscopy). In some cases, the absorbed energy can be transformed into thermal energy, giving rise to acoustic waves that are readily detected by a sensitive microphone (photoacoustic spectroscopy). Alternatively, if the atomic or molecular sample is prepared in a discharge or flame, absorption can be monitored by detecting the variation in the discharge current or ionization in the weak plasma represented by the flame (optogalvanic spectroscopy). This method can be generalized to the case of neutral samples, in which an atom or molecule is ionized through the resonant absorption of two or more photons. The electron-ion pairs thus produced are detected with unitary efficiency, and this method (resonance ionization spectroscopy) has been demonstrated to detect a single atom. A further technique achieves "amplification" of the absorption by including the sample within a laser cavity (intracavity spectroscopy).

### 3.1 Excitation Spectroscopy

Consider a spectroscopic arrangement in which the laser radiation is resonant with an atomic transition $1 \rightarrow 2$. The number of photons absorbed per unit time and unit path length, $n_{abs}$, is proportional to the incident photon flux, the absorption cross section $\sigma_{12}$, and the atomic density $N_1$ in the lower level. The number of photons emitted per unit time from the excited level, $n_{fl}$, is proportional to the number of photons absorbed, $n_{abs}$:

$$n_{fl} = \eta n_{abs} = N_2 A_2, \tag{42}$$

where $A_2 = \Sigma_m A_{2m}$ is the total spontaneous transition probability from the level 2 to all the levels with $E_m < E_2$. The quantum efficiency $\eta$ is

$$\eta = A_2/(A_2 + R), \tag{43}$$

$R$ being the collisional de-excitation rate. In the absence of collisions, all the atoms in level 2 decay emitting photons ($\eta = 1$) that can be collected with a given geometrical efficiency $\delta$ by a photomultiplier. Photons collected on the photocathode surface give rise to the emission of electrons at a rate

$$N_e = n_{abs}\eta\eta_e\delta = N_1\sigma_{12}N_{phot}\eta\eta_e\delta, \tag{44}$$

where $\eta_e$ is the quantum efficiency of the photocathode—i.e., the ratio between the numbers of emitted electrons and incident photons. Modern photocathodes reach quantum efficiencies in excess of 20%, and, by use of photon-counting techniques, it is possible to measure absorption rates of $10^3$ photons per second. With a flux of photons $N_{phot} = 10^{18}$ photons $s^{-1}$ (corresponding to a laser beam of 1 W at 500 nm), this implies that it is possible to detect a relative absorption of $\Delta I/I = 10^{-14}$. This impressive sensitivity can be further enhanced by placing the sample inside a laser cavity where the light flux is one or two orders of magnitude larger.

When the laser radiation is tuned across an absorption line, the total fluorescence intensity $I_{fl} = N_{phot}\sigma_{ik}N_i$ reproduces the absorption spectrum. Although the positions of the lines in the excitation spectrum are coincident with those of the absorption spectrum, the relative intensities can be different. Indeed, the quantum efficiency of both the transitions and the photocathode are dependent upon the laser wavelength. The geometrical efficiency may also vary: indeed, excited atoms with relatively long lifetimes may diffuse out of the interaction volume before emitting any fluorescence photons.

Excitation spectroscopy has been used in atomic- and molecular-beam spectroscopy where the density of particles is rather low. As an example, in Fig. 24 we show a typical spectrum of molecular sodium, excited with radiation at 604 nm. The molecular density in the beam was $N = 10^8$ mol $cm^{-3}$ while the absorption length was 10 mm. In the case of atomic sodium, absolute atomic densities down to $10^2$ atoms $cm^{-3}$ have been measured. The technique has also been successfully used to investigate radicals and short-lived intermediate products in chemical reactions.

Excitation spectroscopy becomes less sensitive in the infrared region, where the photocathode efficiency decreases. In addition,

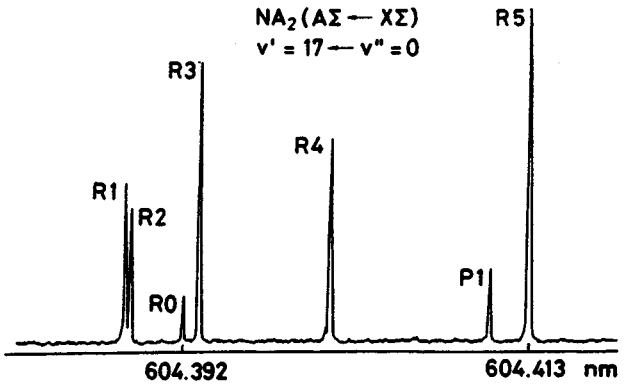


**FIG. 24.** Excitation spectrum of molecular sodium obtained in a molecular beam with radiation at 604 nm (from Demtroeder, 1981).

vibrational–rotational levels excited by infrared photons have lifetimes several orders of magnitude longer than do electronic states. As a consequence, excited molecules escape from the detection volume before they radiate. For such investigations, optoacoustic spectroscopy can be more advantageous.

### 3.2 Optoacoustic Spectroscopy

Although the optoacoustic effect was observed for the first time more than a century ago (Bell, 1881), spectroscopic applications began only with the development of laser sources (Tam, 1986). The technique is based on the fact that energy absorbed by molecules can be converted into rotational, vibrational, and translational energy. At thermal equilibrium, this energy is distributed over all the degrees of freedom, leading to heating of the sample. If the laser intensity is modulated at audio frequencies, sound waves of the same frequencies are induced inside the irradiated cell where they can be detected with sensitive microphones.

Optoacoustic spectroscopy is an unconventional detection scheme (Ernst and Inguscio, 1988) in the sense that microscopic processes, in the form of atom-photon or molecule-photon interactions, are detected through macroscopic changes of the system as a whole (in this case, an acoustic wave). Several advantages are offered with respect to conventional spectroscopic techniques where usually light is monitored. In this case, the detector is only sensitive to the radiation absorbed, and the problem of stray light is completely removed. Moreover, in the infrared, where the sensitivity of common light detectors is very poor, optoacoustic detection can prove to be the only option.

Applications of optoacoustic spectroscopy are numerous and have concerned the monitoring of species at low concentrations in gases, liquids, and solids.

The sensitivity of optoacoustic spectroscopy can be enhanced if the cell is shaped to form a resonant acoustic cavity at the modulation frequency, allowing the detection of concentrations as low as one part in $10^9$. This has also allowed the study of molecules at low pressures, where collisional broadening is small in comparison with Doppler broadening. In this case, Doppler-free techniques have been combined with this method, and, as a demonstration, we show in Fig. 25 a typical two-photon Doppler-free spectrum of the $0 \rightarrow \nu_2$ vibrational transition of $NH_3$ obtained using two counterpropagating beams from a $CO_2$ laser, one being tuned to the 10P(18) line at 945.9802 $cm^{-1}$ and the second to the 10P(34) line at 931.0014 $cm^{-1}$. The energy difference between the final and initial states of the investigated transition differed slightly from the sum of the two photon energies, and resonance was achieved by shifting the energy levels using an external electric field (Stark effect). By changing the intensity of the electric field, transitions between different Zeeman sublevels $m$ are brought into resonance with the fixed laser frequencies, giving rise to the peaks shown in Fig. 26.

### 3.3 Optogalvanic Spectroscopy

The absorption of photons can alter the electrical equilibrium of an irradiated sample. In such cases, charge variations can be monitored, instead of the absorption or emission of light. As with the optoacoustic technique discussed above, the methods based on this principle may be considered unconventional in the sense that a macroscopic response of the system is monitored. Moreover, because of the high efficiency with which electrical charges may be collected, very high sensitivities can be achieved. We discuss here two of the more relevant techniques: resonant ionization spectroscopy (RIS) and optogalvanic (OG) spectroscopy.

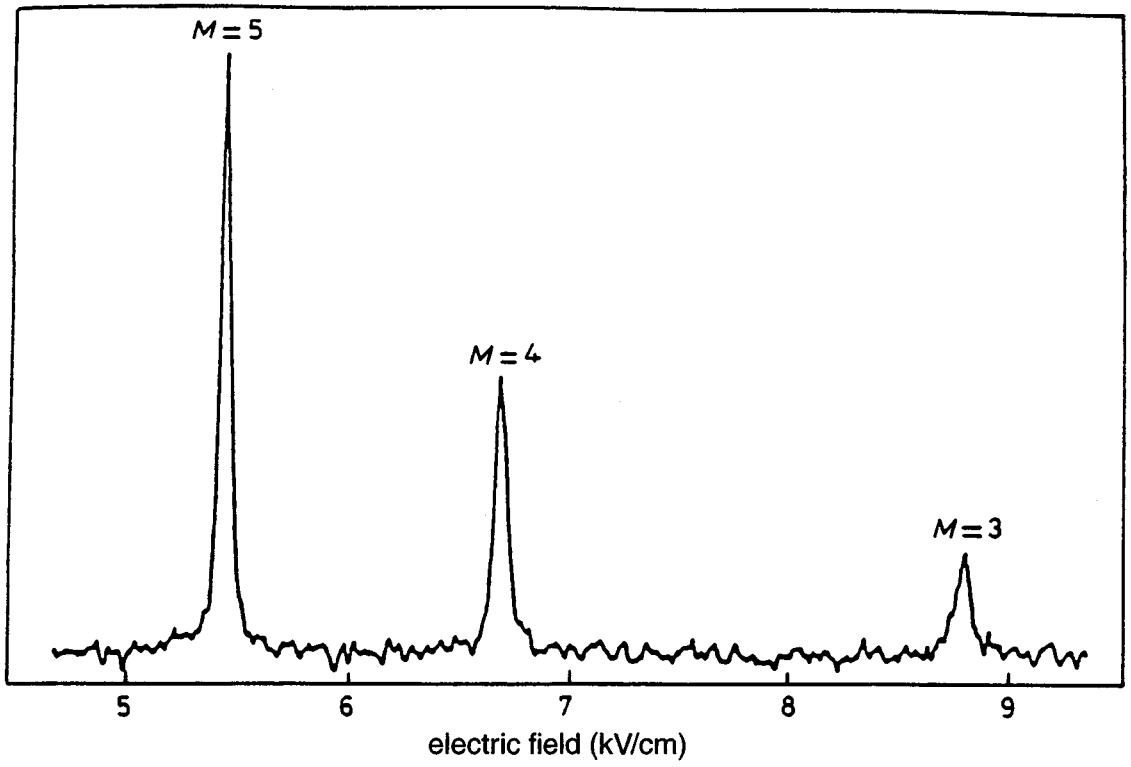


**FIG. 25.** Optoacoustic recording of the two-photon transitions in $NH_3$ observed using the P(18) and P(34) $CO_2$ laser lines (from Minguzzi *et al.*, 1982a).

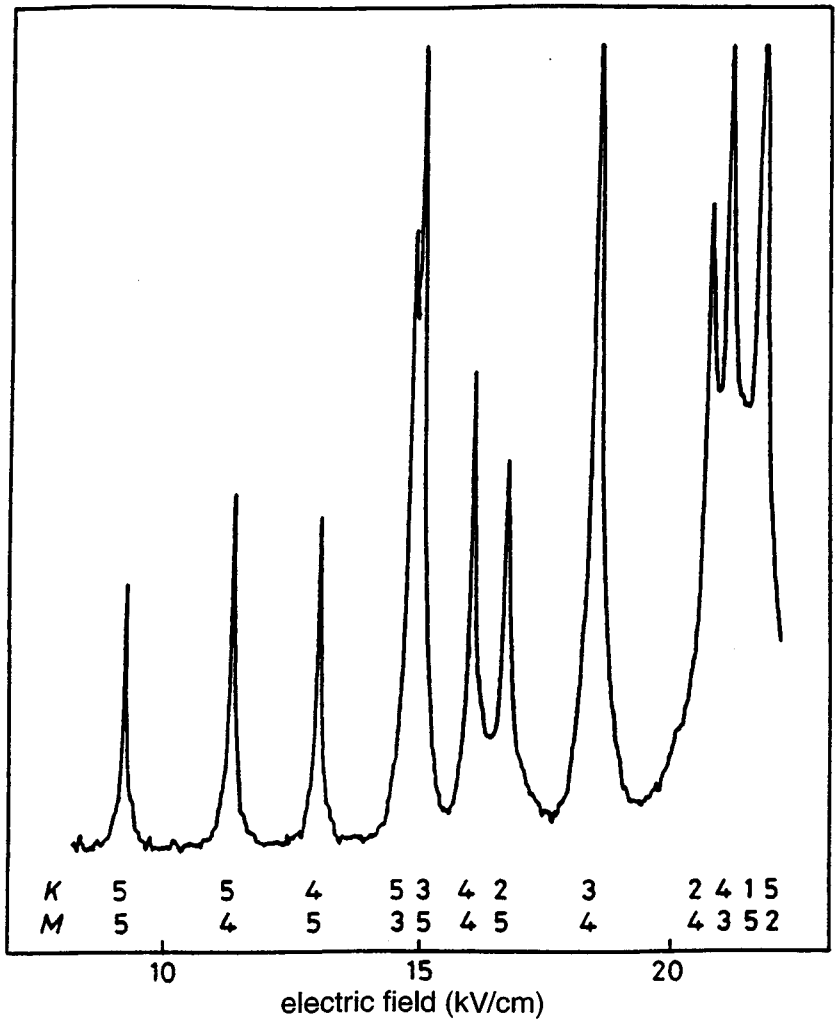


**FIG. 26.** Optoacoustic laser Stark spectrum of $NH_3$, recorded with in termodulated detection (from Minguzzi *et al.*, 1982b).

RIS (Hurst *et al.*, 1979) is a particular case of the more general multiphoton spectroscopy already discussed. In RIS, the final state is the continuum, and two or more photons resonant with intermediate levels are absorbed. Essentially, schemes have been suggested for all the elements of the periodic table by which the element may be ionized through the absorption of two or more photons of suitable wavelengths. The main advantages are that a species can be ionized selectively and that the electron-ion pairs produced may be collected with 100% probability. For this purpose, standard systems employed in nuclear physics can be used as ionization chambers or proportional chambers. The high sensitivity of RIS has been proved by detecting a single atom of caesium in a background of $10^{19}$ atoms of argon. A detection sensitivity of just a few atoms is necessary for studies of very rare events originating in such nuclear reactions as those induced by solar neutrinos, $^{37}Cl(\nu,e)^{37}Ar$.

Even when the atoms or molecules under investigation are in a discharge—a weak plasma—resonant laser radiation can still affect the electrical equilibrium of the discharge itself. This change is observed as an increase or decrease in the conductivity of the discharge and is known as the optogalvanic effect (OGE), first described by Penning (1928), who noted a variation in the impedance of a neon discharge when it was irradiated with emission from an adjacent neon discharge. Extensive and practical applications of the OGE had to await the introduction of tunable lasers (Barbieri *et al.*, 1990).

The mechanisms that translate the OGE into current perturbation are rather complex because of the large number of processes occurring within the discharge, but as a first approximation the effect can be explained by considering the difference between the ionization cross sections $\sigma_i$ for the two states involved in the optical transition. Such a simple model explains the fact that optical excitation leads to a change in the number of charges (electrons and ions), which in turn causes a change in the discharge impedance. In a typical OG detection scheme, the laser beam is amplitude modulated by a chopper, and variations in current are detected by means of a lock-in amplifier. The experimentally observed perturbation of the discharge characteristics induced by laser radiation is usually sufficiently small that the OGE can be considered linearly proportional to the number of photons absorbed.

Many features make OG spectroscopy attractive when compared with other conventional spectroscopic techniques in the ultraviolet, visible, and near-infrared regions of the spectrum. First, it is a relatively economical technique, since it does not require the use of such devices as a monochromator or photomultiplier tube. A glow discharge is an inexpensive way of obtaining quite large densities of excited states in volatile elements, especially in metastable states, and gaseous states of refractory elements are easily produced by sputtering in hollow-cathode discharges. A remarkable population of atoms in excited levels is present in the discharge as a result of electron–neutral-atom collisions, allowing transitions between excited levels to be investigated. OG spectroscopy permits one to record atomic and molecular lines that, otherwise, would be measurable only in an atomic or molecular beam. In molecular spectroscopy, OG techniques are the most natural way to study atomic and molecular species and radicals produced from parent molecular compounds that are present in the discharge.

OG spectroscopy is intrinsically more sensitive than that based upon absorption, the former yielding a signal against a zero background, the latter recording a small variation superimposed on a large signal. In comparison with fluorescence techniques, OG spectroscopy offers the advantage of being unaffected by either the luminosity of the discharge or the stray scatter of excitation radiation.

To underline the diverse mechanisms corresponding to different spectroscopic techniques, we show in Fig. 27 a comparison between various measurements of the same spectrum of neon: by fluorescence, optogalvanic, and optoacoustic spectroscopy. The neon was excited in a positive column at a few Torr and irradiated by a tunable dye laser. The dramatic differences in the relative intensities of the recorded lines are evidence of the various mechanisms governing the different spectroscopic techniques.

The numerous methods developed for sub-Doppler spectroscopy, such as saturation, intermodulated, and two-photon spec-

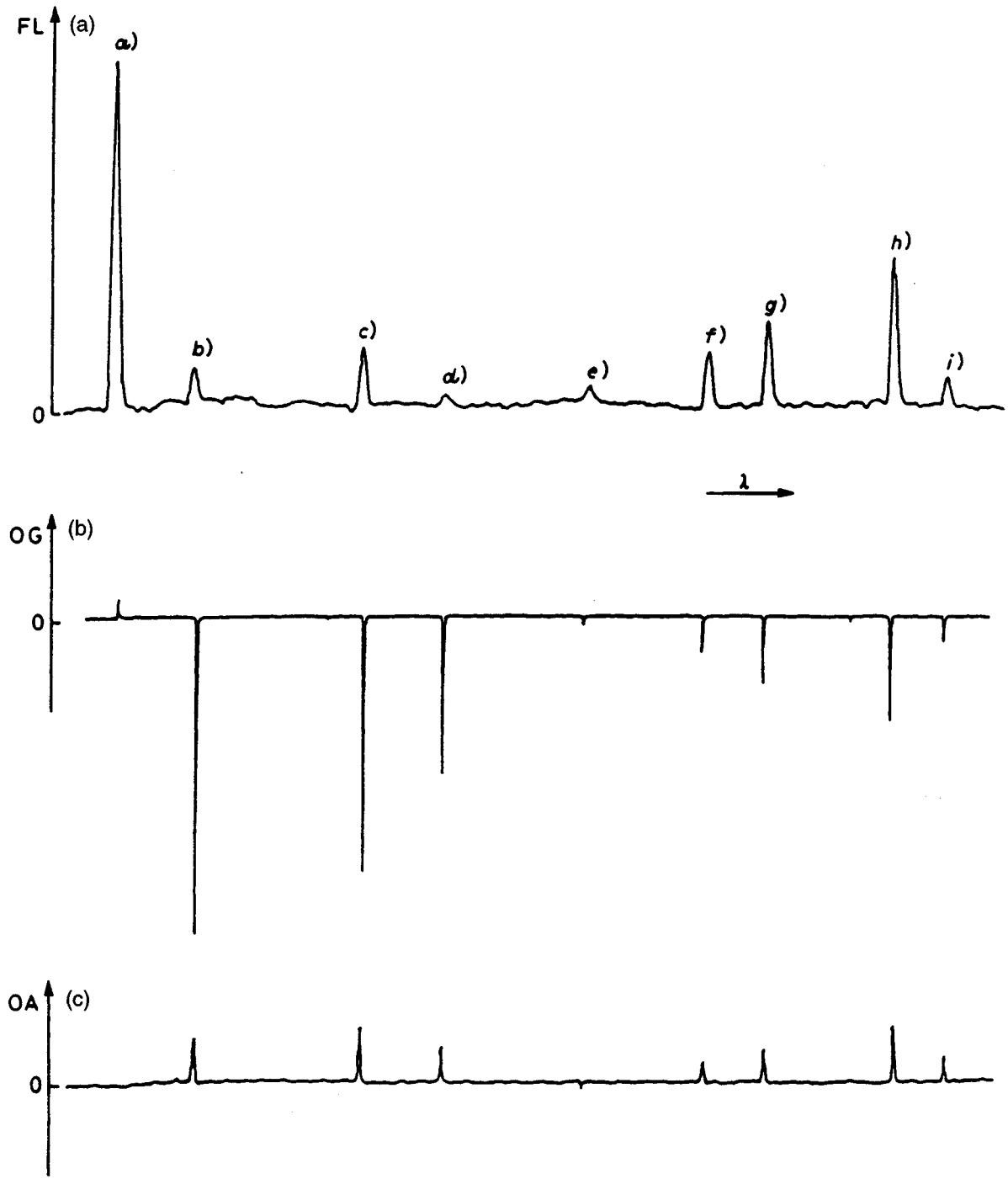


**FIG. 27.** Transitions in neon from 560 to 620 nm. The three spectra are obtained using (a) fluorescence, (b) optogalvanic, and (c) optoacoustic detection. (From Ernst and Inguscio, 1988).

troscopy, can also be applied using the OG technique. The OG signal is actually proportional to the absorption of radiation by the atoms of the discharge, so that the same saturation methods used for other detection schemes, such as optoacoustic or fluorescence spectroscopy, can be used. Transitions between highly excited states of atomic oxygen populated through the dissociation of $O_2$ molecules in a discharge are shown in Fig. 28. The Doppler-broadened spectrum was obtained by using a tunable dye laser around 616 nm, while higher resolution was achieved by means of optogalvanic intermodulated spectroscopy.

### 3.4 Intracavity Spectroscopy

The spectroscopic sensitivity can be enhanced if the sample is placed within the la-

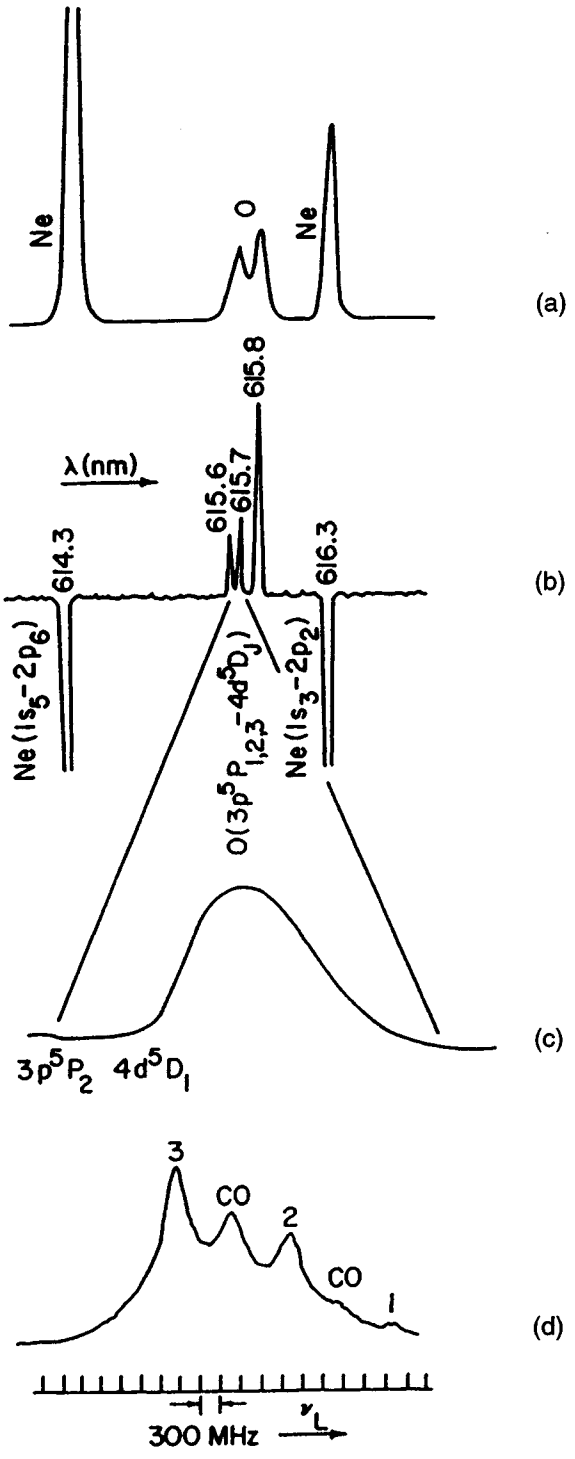


**FIG. 28.** Spectrum of an $O_2$–Ne discharge around 616 nm: (a) fluorescence spectrum; (b) optogalvanic signal obtained by frequency scanning a multimode dye laser; (c) Doppler-limited line profile; (d) intermodulated optogalvanic spectrum of the $^5P_2$–$^5D_{3,2,1}$ transitions (from Barbieri *et al.*, 1990).

ser cavity. Indeed, at a laser output power $P_{out}$, the power inside the laser cavity is

$$P_{inside} = (1/T)P_{out} = qP_{out}, \tag{45}$$

$T$ being the transmissivity of the output coupling mirror. By suitably shaping the laser cavity, a region can be created where the beam is focused (the waist) and the intensity thus further increased. For $\alpha L \ll 1$ the absorbed intensity is

$$\Delta I = (1/T)\alpha L I_{out}, \tag{46}$$

i.e., $1/T$ times the absorption rate observed outside the cavity. For a typical transmissivity of 0.02 ($R$ = 98%), the amplification factor is 50.

If the cell cannot be placed inside the active resonator, an external passive resonator may be used. By matching the laser output to a fundamental mode of the passive resonator and making as low as possible the losses $g$, the power circulating inside the resonator can be $1/q$ times the laser output power. Passive resonators represent an improvement over multipass cells and, since the atoms or molecules experience two counterpropagating beams, a Doppler-free scheme may be adopted.

Intracavity absorption can be monitored through the laser-induced fluorescence or using other detection schemes already discussed (optoacoustic, optogalvanic, etc.). A further improvement in the sensitivity can be obtained if the output power is monitored and the laser is running close to threshold. Indeed, because of the nonlinear response of the laser near threshold, small changes in the losses $\Delta g$ caused by the absorbing intracavity sample lead to a dramatic variation of the laser output. If $G_0$ is the unsaturated gain and $g$ the total loss, it can be shown that the amplification factor $q$ is

$$q = G_0/(G_0 - g)(g + \Delta g) \simeq G_0/g(G_0 - g), \tag{47}$$

where it has been supposed that $\Delta g \ll g$. Equation (47) shows that the sensitivity can be greatly enhanced when the threshold condition is approached ($G_0 \to g$). Nevertheless, an upper limit is imposed by the huge instabilities that a laser exhibits when such a condition is reached. Amplification factors of $10^5$ have been obtained, allowing the study of very weak transitions having oscillator strengths below $10^{-12}$ or with very low concentrations below $10^8$ atoms $cm^{-3}$.

Intracavity spectroscopy has been extensively used in the infrared and far infrared

where the alternative of fluorescence spectroscopy does not exist. The $CO_2$ laser, with tens of lines around 10 $\mu$m, is commonly used, and, because of the narrow tunability of the laser, the resonance condition is usually achieved by shifting the atomic or molecular levels by means of the Stark and Zeeman effects. The Stark effect is used for polar molecules, while Zeeman shifting affects paramagnetic species. By extrapolating the measured frequency to zero field, information on the electric dipole moment or gyromagnetic ($g$) factors can be obtained.

Most rotational molecular lines lie in the far infrared (50 $\mu$m $< \lambda <$ 1 mm) where coherent radiation is usually generated by optically pumped lasers. An apparatus for intracavity spectroscopy in this spectral region has been developed by Evenson (1981) to investigate the rotational structures of molecules and the fine structure of atoms. In the quasiconfocal laser cavity is placed the sample cell, which is separated from the active medium by a window at Brewster's angle. The population inversion in the active medium is created by a $CO_2$ laser, and the far-infrared output is detected by means of a liquid-helium–cooled bolometer; such detectors show very low noise and hence enhanced sensitivity. Absorption coefficients of $10^{-10}$ $cm^{-1}$ have been measured in studies of transient species and free radicals produced in discharges, and of intermediate products in chemical reactions.

An interesting demonstration of the high sensitivity reached by this technique is shown in Fig. 29, which shows the fine-structure $^3P_0$–$^3P_1$ component of the ground state of silicon. Atoms of silicon were produced by dissociation of silane ($SiH_4$) in a microwave discharge, and the resonance condition was achieved by applying a magnetic field of 1121.2 Gauss. It should be noted that there is an excellent signal-to-noise ratio in spite of the extremely low transition probability $A = 8 \times 10^{-6}$ $s^{-1}$.

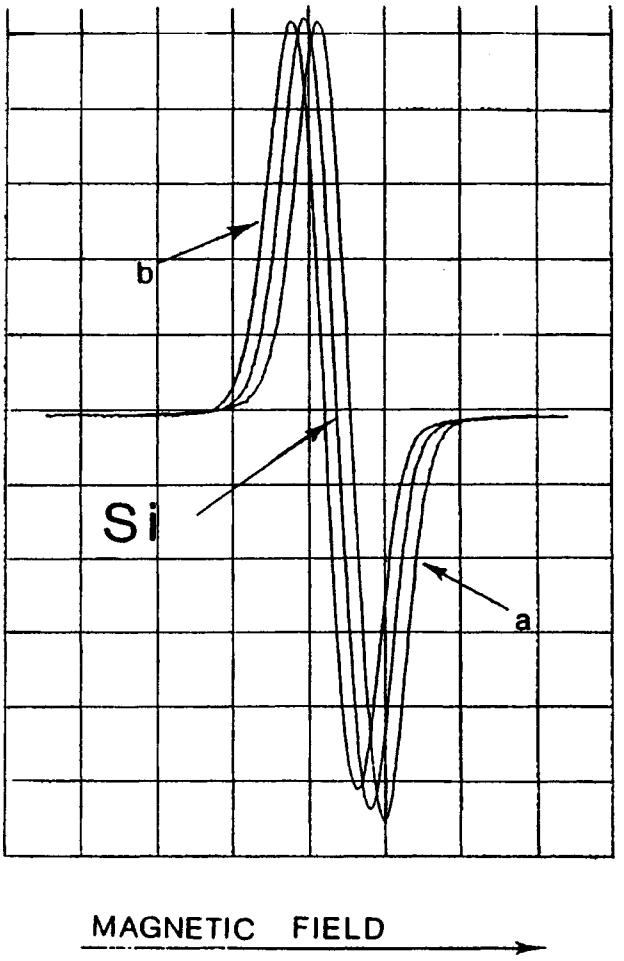


**FIG. 29.** Laser magnetic resonance measurement of the silicon ground-state fine-structure component $^3P_0$–$^3P_1$ of the 129.5-mm line $CH_3OH$. In (a) and (b), the far-infrared cavity was slightly detuned to frequencies respectively higher and lower than the transition to the ground state. (From Evenson, 1981).

## 3.5 Fast Modulation Spectroscopy

We have already seen that a significant improvement in sensitivity over direct absorption techniques may be achieved by modulating the laser amplitude and using a phase-sensitive detection scheme. This principle can be extended to modulating the laser frequency (wavelength modulation) at a relatively high frequency (kilohertz) and by an amount typically several times smaller than the width of the absorption line of the species under investigation. Scanning the laser wavelength and using ac detection at the modulation frequency, or twice the modulation frequency, provides a detected signal that is the first or second derivative of the absorption line shape. When the modulation frequency is comparable with or larger than the linewidth (megahertz or gigahertz range), the two modulation sidebands may be resolved, and the technique is known as frequency-modulation spectroscopy. Such techniques are particularly suited to semiconductor diode lasers, whose wavelengths may be modulated at very high frequencies simply by modulating the injection current.

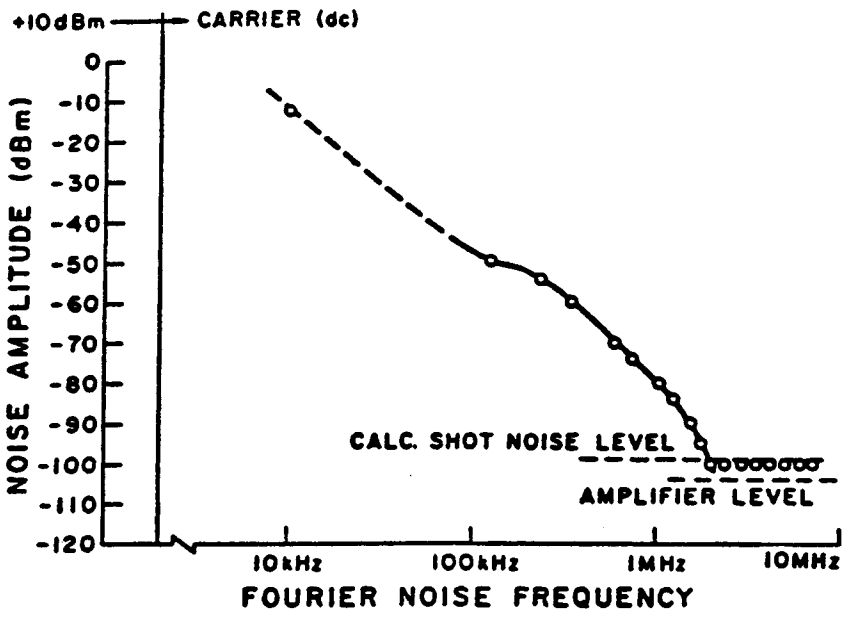


**FIG. 30.** Dye-laser amplitude noise spectral density (300 $\mu$W light power, 10 kHz analysis bandwidth).

In this fashion, absorptions down to $10^{-9}$ $cm^{-1}$ can be measured. The advantages of these techniques derive essentially from the high modulation frequencies, which allow the predominantly low-frequency $1/f$ noise to be rejected. Figure 30 shows the noise spectrum for a diode laser in the megahertz region where the amplitude fluctuations are dominated by shot noise.

In Fig. 31, the same transition in methane has been observed using absorption, wavelength-modulation, and frequency-modulation techniques. The signal-to-noise ratio in the FM case clearly represents an improvement of several orders of magnitude. Moreover, the sloping baseline is removed, and high discrimination against signals that do not show wavelength dependence is introduced.

Still higher sensitivity can be achieved with heterodyne detection, which is an extension to optical and infrared wavelengths of the superheterodyne radio receiver. A beam of radiation of frequency $\nu_s$ is detected by a photodiode that absorbs photons and releases charge carriers, the photocurrent being proportional to the square of the total electric field $E_s$ of the incident radiation. With direct detection, this means that the photocurrent is proportional to the power of the optical or IR field.

In heterodyne detection, however, the incoming radiation is mixed in the detector with radiation from a local oscillator ($E_l$) of frequency $\nu_l$, which could be a diode laser or

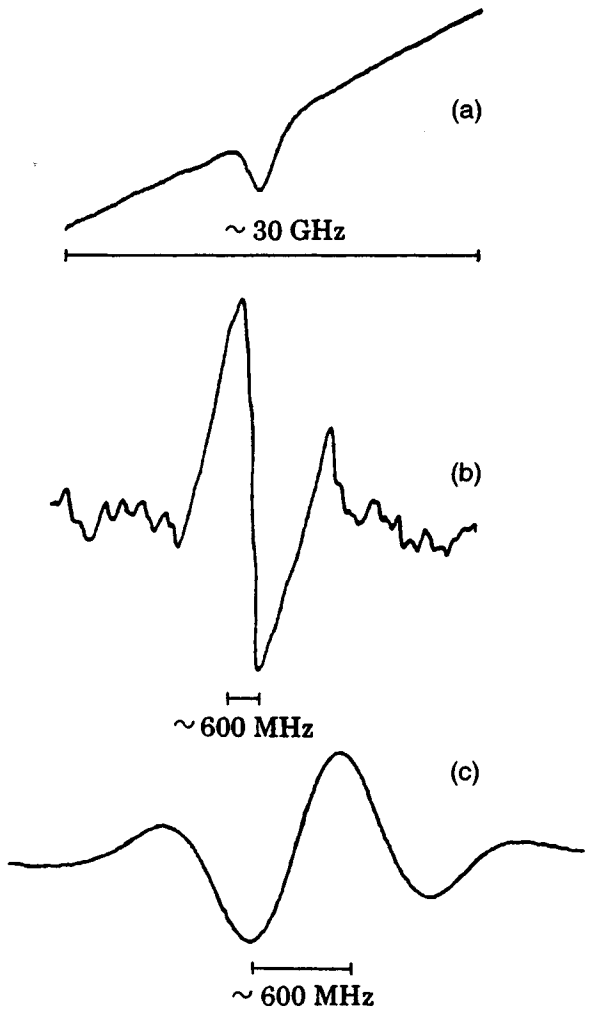


**FIG. 31.** (a) Pure absorption signal on the third overtone of methane ($CH_4$) at 100 Torr. Derivative line shapes recorded at 500 mTorr with (b) WM and (c) two-tone FM spectroscopy.

a $CO_2$ laser, producing a photocurrent containing the terms $E_s^2$, $E_l^2$, $E_s$, and $E_l$. The first two terms correspond to the optical and local oscillator powers. More interesting is the mixing term $E_sE_l$ that oscillates at the beat frequency $\nu_b = |\nu_s - \nu_l|$ between the two fields. This frequency difference $\nu_b$ can be chosen to be in the radio-frequency region where amplification can readily be performed. The heterodyne receiver can thus detect radiation in a narrow spectral band around the local oscillator frequency, and the bandwidth is determined by electronic filters instead of optical filters or dispersive optics. The power signal-to-noise ratio of a heterodyne receiver is

$$\text{SNR} = \eta P_s/h\nu B, \tag{48}$$

where $\eta$ is the heterodyne quantum efficiency, $P_s$ is the signal power, and $B$ is the bandwidth of the receiver. It is sometimes also convenient to use phase-sensitive detection at the frequency of a beam chopper to increase further the signal-to-noise ratio.

## 4. TIME-RESOLVED SPECTROSCOPY

In the preceding sections we have discussed a variety of spectroscopic techniques in which information about atomic or molecular structures is obtained by analyzing the response of the system as a function of the optical frequency. In this section, by contrast, we consider the temporal response of a system when it is irradiated by short laser pulses. We will see that spectroscopic techniques based on the temporal and frequency domains can provide complementary information.

The availability of short and intense laser pulses allows the transfer of a large fraction of an irradiated sample of ground-state atoms or molecules into excited states. By use of step-wise excitations with synchronized lasers, highly excited levels can be reached. By monitoring of the temporal decay of fluorescence from a given level, the lifetime of that level can be measured. If two closely lying states are excited coherently, a new class of phenomena can be studied, such as quantum beats, whereby atomic interference is observed as a temporal modulation of the fluorescent intensity. The recent development of ultrashort laser pulses, of picosecond or subpicosecond duration (Shapiro, 1977), makes possible the investigation with extremely high time resolution of ultrafast relaxation processes occurring during the excitation and deactivation of molecular states.

The interaction between atoms and very short, intense laser pulses also gives rise to strong nonlinear processes. Atoms in very intense laser fields can be ionized by absorbing tens of photons. Furthermore, within the same laser pulse, the ions produced can be further ionized several times (multicharge ionization), while quasifree photoelectrons may absorb further photons (above-ionization spectroscopy). In such strongly nonlinear regimes, high-order harmonics reaching into the x-ray region can be generated.

### 4.1 Lifetime Measurements

Lifetime measurements are of particular interest in spectroscopy, for the lifetime is directly related to the transition probability, and hence, such measurements make possible the testing of quantum mechanical calculations. Anomalies among the lifetimes within a molecular band can also provide information about perturbations due to coupling with other series. Finally, lifetimes are of more applied interest—for instance, in laser physics.

In Sec. 1 we showed that the radiative width of a line is related to the lifetimes of the lower and upper levels of the transition. We also mentioned that the homogeneous width is usually affected by such other broadening effects as saturation, time of flight, collisions, etc. Even if these further broadening mechanisms are removed, to determine from a transition linewidth the lifetime of a given level requires knowledge of the lifetime of the other level (unless it is the ground state). Unlike frequency-domain spectroscopy, time-resolved measurement allows the lifetime to be evaluated directly. Several experimental approaches have been developed.

**4.1.1 Phase-Shift Method** This method is based on the use of a cw laser, sinusoidally modulated in amplitude at a frequency $f$ and resonant with a transition $i \rightarrow k$ of frequency $\omega_{ik}$. The rate equation for the final state $k$ is

$$dN_k/dt = \sigma F(N_i - N_k) - N_k/\tau, \quad (49)$$

where $\sigma$ is the absorption cross section, $F$ the photon flux, and $\tau$ the lifetime of the level $k$. The difference $N_i - N_k$ in Eq. (49) takes into account absorption and stimulated emission, while $N_k/\tau$ represents the spontaneous emission decay. The photon flux is

$$F = (I_0/\hbar\omega_{ik})(1 + a \sin 2\pi ft) \cos\omega_{ik}t. \quad (50)$$

The induced resonant fluorescence is modulated at the same frequency but is shifted in phase with respect to the forcing excitation field by an amount $\phi$, related to the level lifetime $\tau$ by

$$\tan\phi = 2\pi f\tau. \quad (51)$$

By measuring the phase shift $\phi$ with a lock-in amplifier, the lifetime $\tau$ can thus be estimated.

This method fails when two or more levels with different lifetimes are simultaneously populated. In this case the induced fluorescence for each level presents different phase shifts, which are not easily determinable. The method also suffers in the event of stimulated emission [see Eq. (49)], which is especially likely to be present when laser sources are used.

**4.1.2 Pulse Excitation** Another approach to lifetime measurement makes use of pulsed lasers able to excite the atoms or molecules in a time short compared with the lifetime of the investigated level. The fluorescence decay can be observed in the absence of stimulated emission in two different ways.

With the first method the fluorescence is monitored directly by means of a transient digitizer or a boxcar. To reconstruct the whole exponential curve using either technique requires many fluorescence photons per excitation pulse, and nonlinearities in the photomultiplier response present a further limitation to this technique. These difficulties can be overcome by a delayed-coincidence method, which operates in the regime of extremely low intensity. In this technique, single-photon counts are recorded while the repetition rate of the excitation laser pulse is chosen to be as high as possible. At the heart of the experimental scheme is a time-to-amplitude converter. A trigger signal synchronized to the laser pulse starts a voltage ramp at time $t_0$, which is stopped by the first fluorescence photon after the excitation pulse, detected at time $t_1$. The ramp height is thus proportional to the time interval $t_1 - t_0$ and is stored by a multichannel analyzer. After each excitation pulse, a given channel will be increased by one unit, and the voltage distribution recorded by the multichannel analyzer thus yields the decay curve directly (see Fig. 32).

It is important that the detection probability be kept below one fluorescence photon per excitation pulse to avoid so-called pileup. If two or more photons were generated, the photons with short delays would be over-represented, and the decay curve would be altered.

Although a high repetition rate is required in order to provide a reasonable measurement time, the pulse frequency also has an upper limit, for the time interval between two pulses must be longer than the lifetime of the investigated level. Moreover, the pulse frequencies must not exceed the reciprocal of the dead time of the electronic chain, which is typically 100 ns.

The decay of an excited state can also be monitored with a second laser (probe) tuned to a transition sharing a common level with the investigated transition (pump-and-probe technique). When the pump pulse alters the population of this level, the probe pulse can monitor how quickly the population is restored through relaxation processes if a controlled delay is introduced between pump and probe pulses. The pump-and-probe technique is particularly useful for investigating ultrafast processes (picosecond and femtosecond range) where conventional techniques fail.

### 4.2 Quantum-Beat Spectroscopy

If two or more closely spaced atomic or molecular levels are simultaneously excited by a short laser pulse at $t = t_0$, the total wave function will be given by the superposition of the wave functions of the excited states:

$$\Psi(0) = \sum_k a_k \Phi(0), \quad (52)$$

where $a_k$ is the probability amplitude that

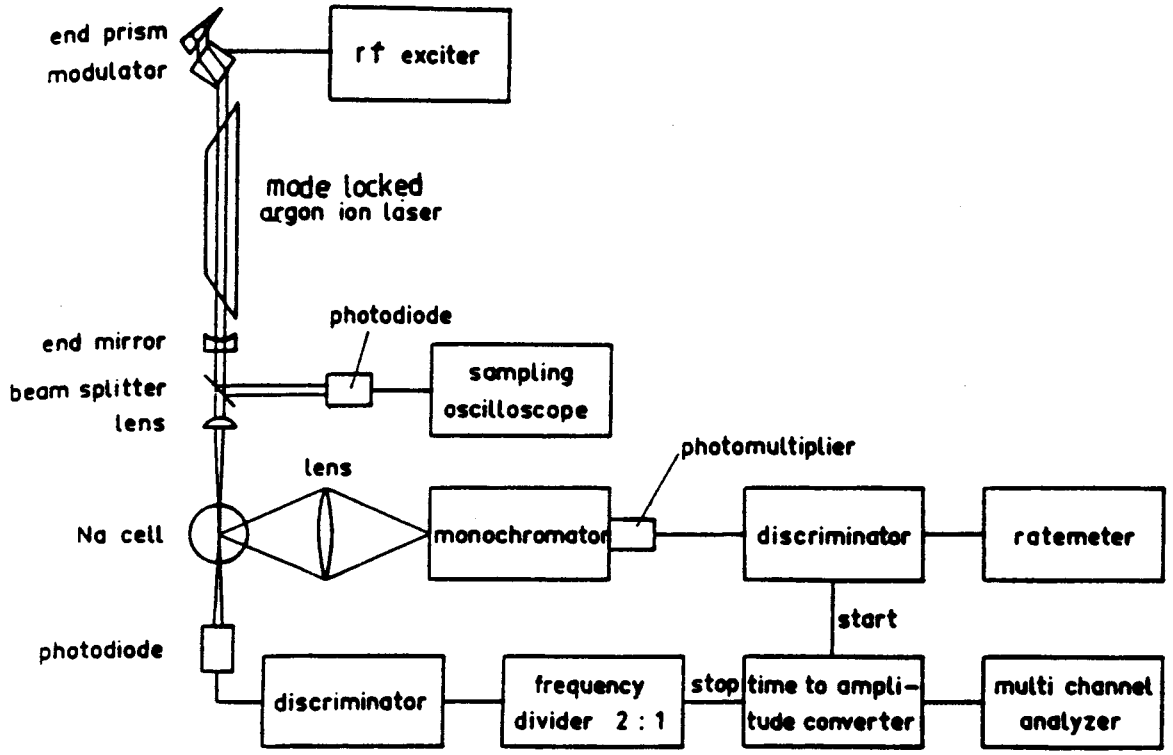


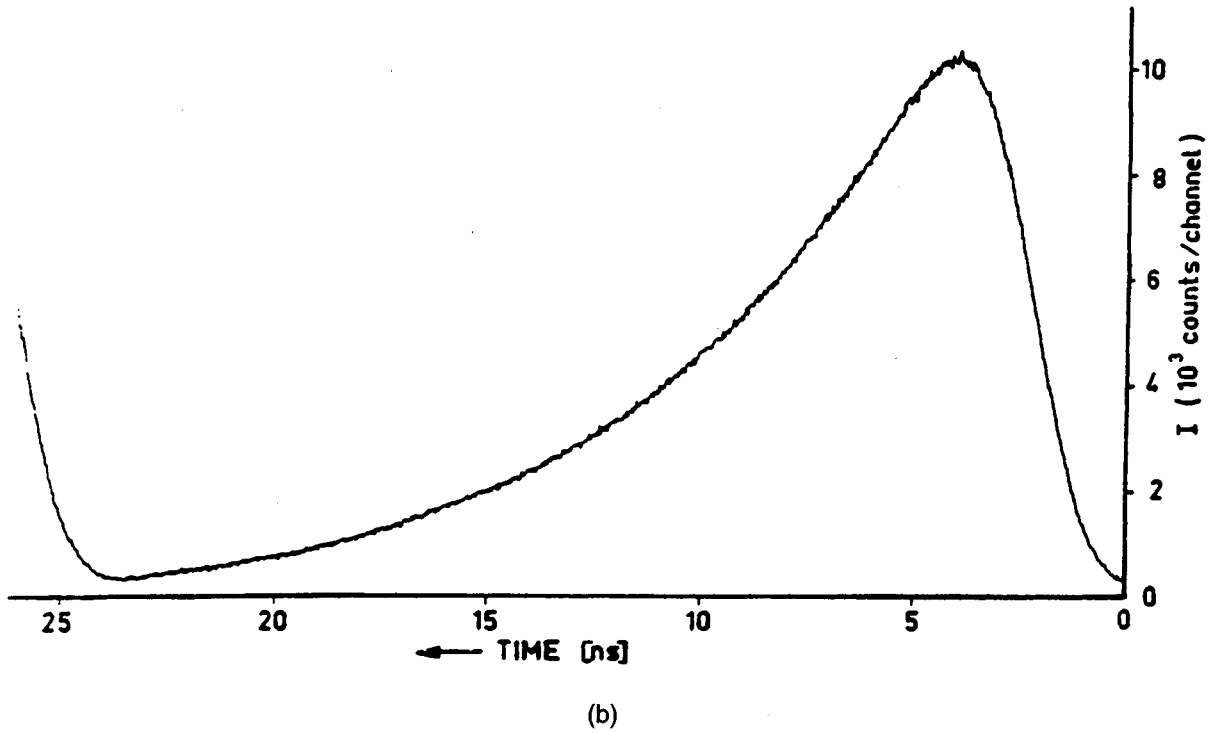


**FIG. 32.** (a) Schematic diagram of the delayed-coincidence technique. (b) Fluorescence decay, reconstructed by a multichannel analyzer. (From Demtroeder, 1981.)

the light pulse has prepared the atom in level $|k\rangle$. The time-dependent intensity of the fluorescence emitted when the excited levels decay into the final state $|f\rangle$ is given in terms of the matrix element by

$$I(t) = CI|\langle\Phi_f|\epsilon r|\Psi(t)\rangle|^2, \tag{53}$$

where $\epsilon$ is the polarization vector and $\Psi(t)$ is the temporal evolution of the total wave function, given by

$$\Psi(t) = \sum_k a_k |\Phi_k(0)\rangle \exp\left[-(iE_{kf}/h + \gamma_k/2)t\right]. \tag{54}$$

Inserting (54) into (53) and assuming equal the decay rates of levels 1 and 2 ($\gamma_1 = \gamma_2 = \gamma$), we have

$$I(t) = C \exp(-\gamma t)(A + B \cos\omega_{21} t), \tag{55}$$

where $A$ is the sum of the transition probabilities $1 \to f$ and $2 \to f$, $B$ is the interference term, and $\omega_{21} = (E_2 - E_1)/\hbar$. The time-dependent fluorescence is hence given by the superposition of an exponential curve and an oscillation with frequency $\omega_{21}$. The measurement of such an oscillation allows the determination of very closely spaced energy levels. Quantum-beat spectroscopy therefore allows Doppler-free resolution.

In Fig. 33 a typical example of a Zeeman quantum beat for a resonance line in ytterbium is shown. The three Zeeman sublevels of the upper level $^3P_1$ are excited simultaneously, but only the levels with $m_j = +1$ and $m_j = -1$ can decay into the ground state $^1S_0$ (transitions with $\Delta m_j = 0$ for $m_j = 0 \to m_j = 0$ are forbidden by the selection rules). The modulation observed in the time-dependent fluorescence is thus related to the separation of these two levels.

If further levels are excited simultaneously, modulations appear in the time-dependent fluorescence at a different frequency, and their measurement in the time domain becomes rather difficult. In this case the Fourier transform of the time-dependent fluorescence intensity yields its spectral distribution $I(\omega)$ with sub-Doppler resolution. Figure 34 illustrates as an example quantum beats measured by Andrä *et al.* (1975) in the fluorescence following excitation of three hyperfine levels in the $6p\ ^2P_{3/2}$ state of the $^{137}Ba^+$ ion.

## 5. ULTRAHIGH-RESOLUTION SPECTROSCOPY

Many of the processes by which spectral lines are broadened are due to the random motion of the atoms. Let us consider an atom of mass $M$ and velocity $v$. On account of its motion, the atom absorbs photons at a frequency $\omega'$ given by the relation

$$\omega' = \omega_0 + kv - \omega_0 v^2/2c^2, \tag{56}$$

where $\omega_0 = (E_b - E_a)/\hbar$ is the resonance fre-

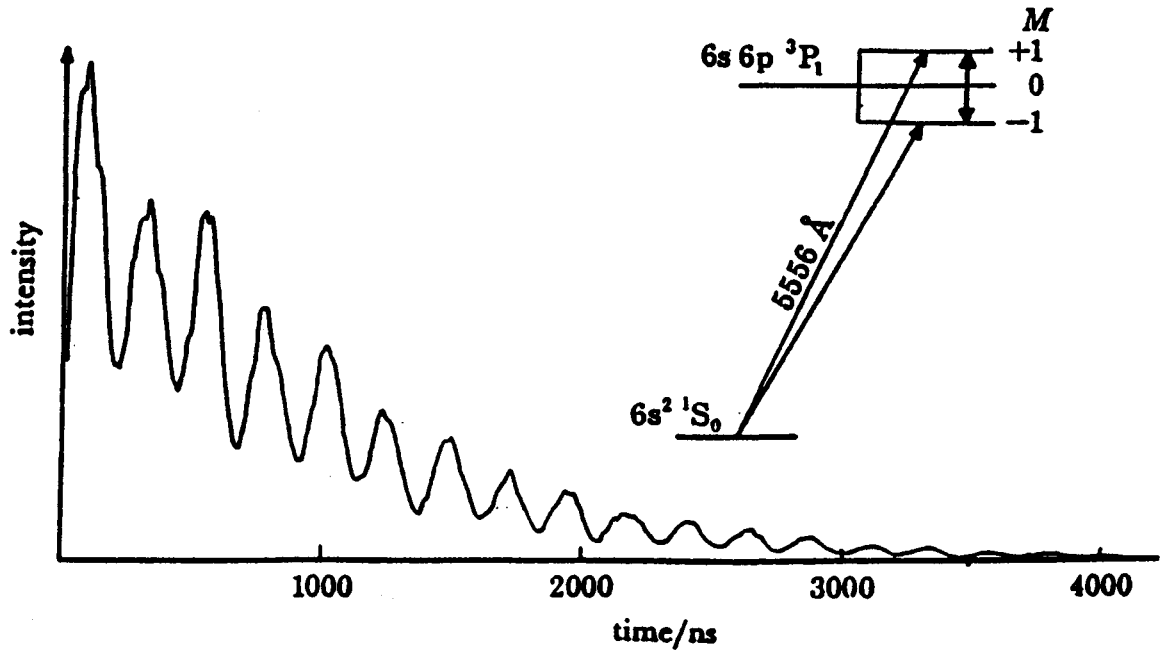


**FIG. 33.** Typical example of Zeeman quantum beat for the resonance line in ytterbium (from Svanberg, 1992).

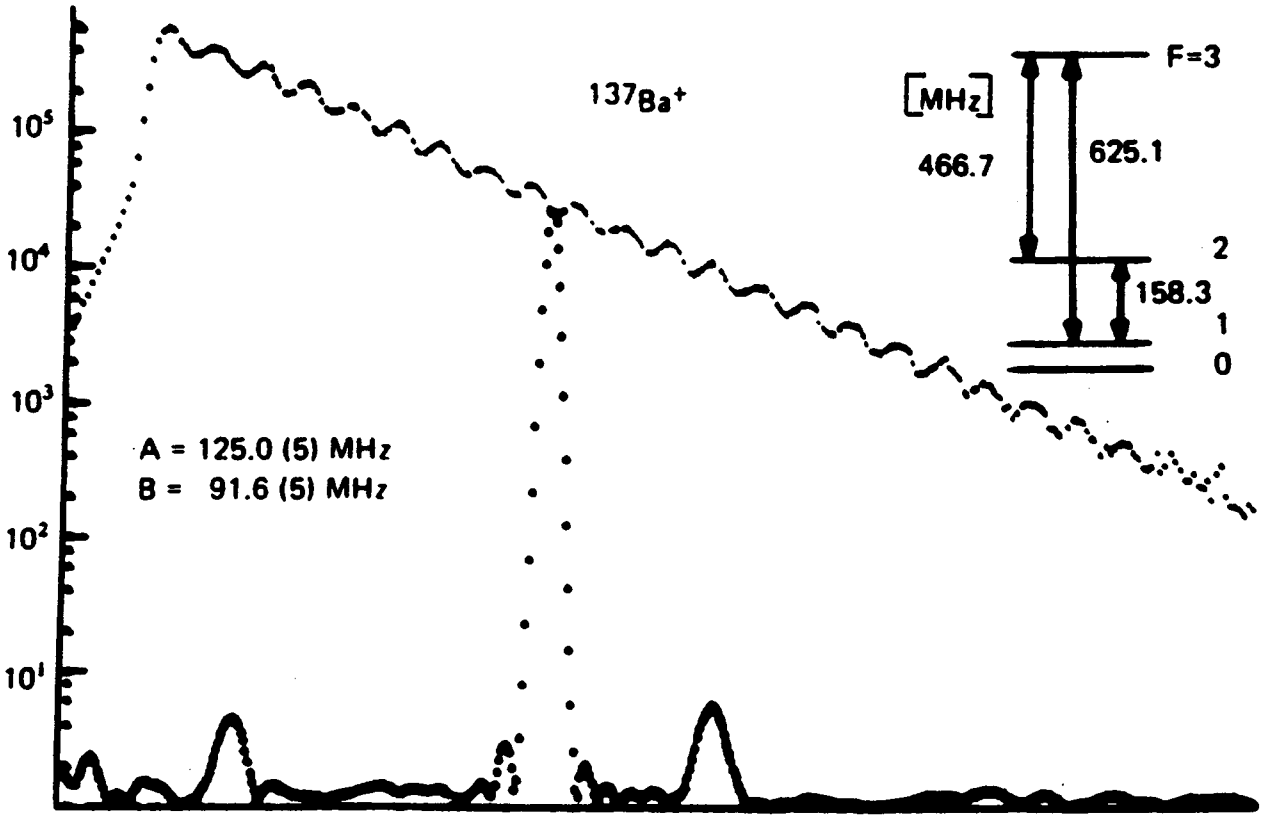


**FIG. 34.** Quantum beats in fluorescence from the $6p\ ^2P_{3/2}$ state of the $^{137}Ba^+$ ion (from Andrä, 1975). The upper curve represents the time evolution of the emitted fluorescence following excitation, and the lower curve is the Fourier-transform spectrum.

quency and the second and third terms represent, respectively, the first- and second-order Doppler shifts.

In the preceding sections we have seen that the linear (first-order) Doppler shift can be canceled by use of atomic beams or by means of one of the numerous Doppler-free spectroscopic techniques, but such methods fail to eliminate the second-order Doppler shift, which, as shown in Eq. (56), depends quadratically upon the atomic velocity. Another effect strictly connected to the atomic motion is the previously discussed transit-time (or time-of-flight) broadening. In many cases these two broadenings determine the ultimate limit of spectral resolution. This is the case, for instance, for transitions involving long-lived levels for which the radiative width is very narrow. Full resolution of such narrow transitions is of importance in testing the fundamental laws of physics and for many metrological applications such as atomic clocks. In order to achieve maximum resolution, it is necessary to reduce the atomic velocities, since this reduces the second-order Doppler shift and increases the interaction time between the atoms and the laser field.

When an atom interacts with a light beam, the emitted and absorbed photons carry much information about the atomic structure, this being the essence of spectroscopy. But the interaction of photons with atoms can also be used to manipulate the kinetic status of the atoms, i.e., their velocity. This phenomenon, usually manifested as so-called laser cooling, was first suggested independently by Hänsch and Schawlow (1975) for neutral species and by Wineland and Dehmelt (1975) for trapped ions. A more detailed discussion of this subject is reported in the article ATOMIC COOLING AND TRAPPING.

In the last few years, there has been increasing interest in the use of near-resonant photon scattering to cool and trap atoms and ions. This interest is motivated in part by the physics governing such phenomena and in part by the wide variety of atomic and molecular physics experiments to which it may be applied. The production of ultracold atomic samples alone, having temperatures of a few tens of microkelvins, has opened up

a rich area for experiments in atomic and molecular physics. One of the main applications is in ultrahigh-resolution spectroscopy, since for very slow atoms the first- and second-order Doppler shifts and the pressure shift are eliminated, and Doppler-free techniques are no longer required.

The production of cold atoms moreover offers the possibility of revisiting the physics of collisions in a new light. There are two principal reasons for investigating collisions in atomic traps: The first is to understand, and perhaps to minimize, the role of such collisions because they represent a significant loss channel; the other is to explore the fundamental physics of ultracold collisions between atoms with large de Broglie wavelengths, for which hitherto unseen effects can be expected.

### 5.1 Laser Cooling

The principle of laser cooling is best illustrated by a two-level atomic system (Meystre and Stenholm, 1985; Chu and Wieman, 1989). We consider an atom of mass $M$ moving along the $z$ axis with a velocity $v$. A photon of frequency $\omega$ traveling in the opposite direction can be absorbed if $\omega$ is appropriately Doppler shifted with respect to the resonance frequency $\omega_0$.

The photon momentum $h\nu/c$ changes the velocity of the atom by

$$\Delta v = h\nu/Mc. \tag{57}$$

We suppose that the excited atom can decay radiatively only back to the initial state. During this process, the atom also receives a velocity kick when it radiates a photon by spontaneous or stimulated emission. In the presence of a single laser beam, stimulated photons will be emitted in the same direction as the incoming photons, and as a consequence, the momentum transferred by the absorbed photon will be canceled. In contrast, the spontaneous photons will be emitted in random directions; the average momentum transfer is in this case zero, and there is thus overall a net momentum transfer from the radiation to the atoms. Because this process depends upon spontaneous emission, the radiation pressure force that results is often known as the spontaneous force.

The recoil depends on the energy of the photon ($h\nu$) and the mass $M$ of the atom ($\Delta v = h\nu/cM$). For instance, for sodium ($M = 23$ amu) and $\lambda = 589$ nm, the velocity change per photon absorbed is about 3 cm $s^{-1}$. If the initial atomic velocity is typical of room-temperature distributions (about $10^3$ m $s^{-1}$), the number of scattered photons required to stop the atoms will be $n_{\text{phot}} = v/\Delta v = 3 \times 10^4$. The cooling transition $a \rightarrow b$ must therefore be closed, in the sense that atoms in upper level $b$ may decay radiatively only to the initial state $a$. For sodium, the $3S_{1/2}$–$3P_{3/2}$ transition is suitable for such a cooling scheme, even though the presence of hyperfine structure renders the transition incompletely closed (optical pumping).

During laser cooling, atoms undergo a maximum deceleration given by

$$a = h\nu/2Mc\tau,$$

where $\tau$ is the lifetime of the upper level of the cycling transition and the factor 2 takes into account the fact that atoms spend only half of their time in the upper level. Again for sodium, $a = 10^6$ m $s^{-2}$, which corresponds to $10^5$ times $g$. This strong acceleration is sufficient to bring to rest a thermal sodium atom in 1 ms and over a distance of 0.5 m, which is quite reasonable on the laboratory scale.

An experimental apparatus suitable for laser cooling is shown in Fig. 35. A laser beam, appropriately detuned with respect to the atomic resonance, travels against an effusive atomic beam. A second laser beam, acting as an analysis beam, is roughly collinear with the cooling laser. When the laser frequency is tuned onto resonance, atoms absorb and re-emit photons that can be detected by a photomultiplier. The analysis beam is swept in order to probe the velocity distribution modified by the cooling beam. Part of the analysis beam is sent perpendicular to the atomic beam to provide a zero-velocity marker.

The magnetic coils in Fig. 35 produce a varying magnetic field along the atomic beam direction, which shifts the Zeeman sublevels so that the transition frequency between two Zeeman levels changes with position. With a suitable dependence of $B(z)$, the transition frequency for moving atoms can

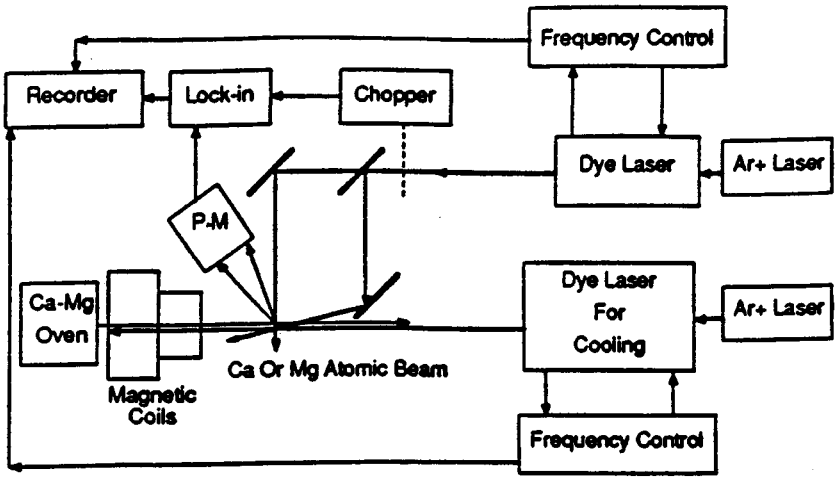


**FIG. 35.** Schematic diagram of the apparatus used for the laser cooling of neutral atoms (from Beverini *et al.*, 1989).

be resonant with the fixed laser-cooling frequency.

The early experiments on laser cooling of neutral atoms used a sodium beam chosen both because the resonance transition is closed and accessible to tunable single-mode dye lasers and because of its short radiative lifetime. Many atoms have since been manipulated with laser light, and in Fig. 36 we show the result of laser-cooling atoms of calcium using the transition $^1S_0$–$^1P_1$ at 422 nm.

## 5.2 Atom Traps

In the preceding section we have discussed a method of stopping the atoms in an atomic beam. Another aspect of atomic manipulation is confinement to a region of space where the atoms can then be investigated.

In 1985, Chu *et al.* demonstrated the possibility of cooling neutral sodium atoms in so-called optical molasses. Magneto-optical traps represent a refinement of this idea whereby atoms are localized at higher densities and cooled to temperatures limited by the atomic recoil energy.

**5.2.1 Magneto-optical Traps** The magneto-optical trap (MOT) (Raab *et al.*, 1986) depends upon two features: the Zeeman interaction with an inhomogeneous magnetic field, and the radiative selection rules that

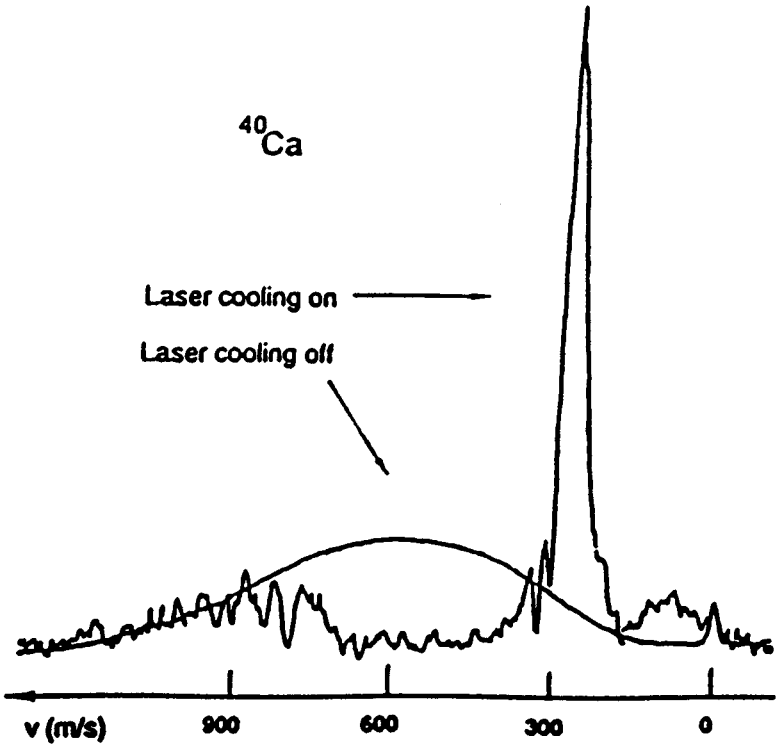


**FIG. 36.** Laser cooling of calcium observed in presence of magnetic field.

govern transitions between magnetic levels in an atom.

The basic principle of the MOT can be illustrated by considering a hypothetical atom with a spin $S = 0$ ($m_s = 0$) ground state and a spin $S = 1$ ($m_s = -1, 0, +1$) excited state. In a weak, inhomogeneous magnetic field $B(z) = bz$, the energy levels will be split through the Zeeman effect by an amount $\Delta E = \mu m_s bz$. In the presence of two counterpropagating waves with $\sigma^+$ and $\sigma^-$ circular polarizations (see Fig. 37), with a frequency tuned below the atomic resonance, an atom at $z > 0$ will absorb more $\sigma^-$ photons than $\sigma^+$ photons since the laser frequency is closer to the $\Delta m_s = -1$ transition frequency. Similarly, for an atom at $z < 0$, the Zeeman shift is reversed, and the atom will absorb more $\sigma^+$ photons. Because of the momentum carried by these photons, the position-dependent differential absorption leads to the presence of a force, which pushes atoms into the region $z = 0$. The scheme can be readily extended to three dimensions by using three pairs of counterpropagating beams along the $x$, $y$, and $z$ directions and a spherical quadrupole magnetic field, as shown in Fig. 37.

This type of trap can also be used for atoms with a more complicated hyperfine structure such as, for instance, sodium or cesium. Atomic samples with densities of $10^{10}$ atoms $cm^{-3}$ and at temperatures of a few tens of millikelvins have been obtained. At such low temperatures, atoms move with velocities of a few centimeters per second, which allows direct Doppler-free spectroscopic measurements. In Fig. 38 is shown a

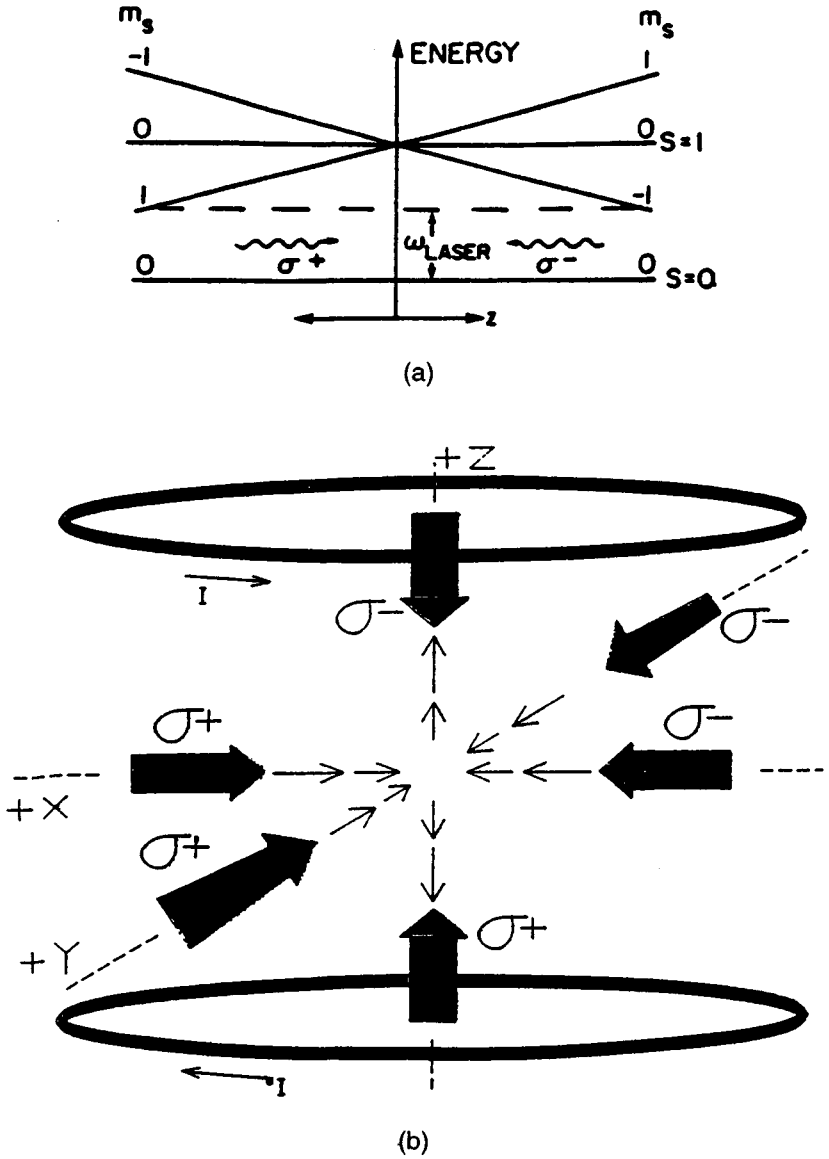


**FIG. 37.** Arrangement for a magneto-optical trap. (a) The energy-level scheme for an atom having spin $S = 0$ in the ground state and $S = 1$ in the excited state. (b) Experimental arrangement of a three-dimensional trap. (From Raab *et al.*, 1986.)

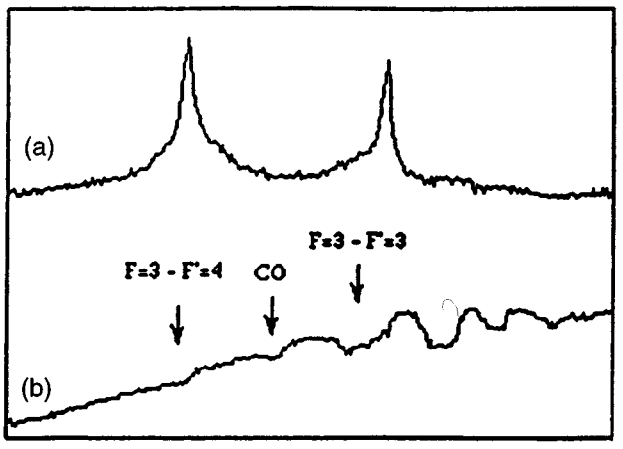


FIG. 38. (a) Resonant fluorescence from cold atomic cesium produced in a magneto-optic trap. (b) For comparison, the saturated absorption spectrum is shown.

spectrum of the cesium $6S_{1/2}(F = 3, 4)$–$6P_{3/2}(F = 3, 4)$ transition obtained by laser irradiation of a cloud of trapped atoms [Fig. 38(a)] and a conventional saturated absorption spectrum [Fig. 38(b)]. The linewidth observed with the cold atoms is about 30 MHz, somewhat wider than the natural width of the transition (5.3 MHz). This is essentially due to the saturating effect of the trapping laser. In order to improve the resolution, the atoms should be measured after switching off the trapping and repumping laser beams.

## GLOSSARY

**Absorption Spectroscopy:** The study of radiant energy that is characteristically absorbed by a particular atom or molecule.

**Bennet Hole:** The hole that is produced in the velocity distribution when narrow-band laser light is absorbed.

**Coherence:** One of the most important properties of the laser radiation. It is essentially related to the high spectral purity of the laser light. Coherence takes part also in the excitation of atomic or molecular transition when this is realized with laser sources.

**Doppler Linewidth:** The width of a spectral line caused by the Doppler effect.

**Doppler-Free Spectroscopy:** Spectroscopic techniques that allow elimination of the Doppler broadening. They are essentially based on two main approaches: velocity-selective saturation or counterpropagating two-photon absorption.

**Emission Spectroscopy:** The study of radiant energy that is characteristically emitted by atoms or molecules after a suitable excitation.

**Intracavity Spectroscopy:** High-sensitivity spectroscopic techniques where the atomic or molecular sample under investigation is inserted into a laser cavity or a passive cavity having a high quality factor.

**Laser:** An acronym for light amplification by stimulated emission of radiation. A device that emits a high-intensity, narrow-spectral-width, and highly directional beam of light by stimulated emission in an atomic or molecular system where a population inversion between two levels has been produced.

**Laser Beam:** The bright stream of light emitted by a laser. The near-zero divergence makes this beam extremely interesting for a wide variety of applications (surgery, communications, printing, physics, chemistry, etc.).

**Laser Cooling:** A method based on the scattering of near-resonant photons to slow atoms in an atomic beam to very low velocity.

**Laser Trapping:** A method based prevalently on laser radiation to trap neutral and ionized atoms in a small volume at extremely low kinetic energy and, hence, low temperatures.

**Linewidth:** The spread in wavelength of a spectral line. Usually it is measured as the full width at half maximum (FWHM).

**Multiphoton Spectroscopy:** Spectroscopic techniques based on the simultaneous absorption of two or more photons.

**Natural Linewidth:** The width of a spectral line caused by the finite lifetime of the levels.

**Optogalvanic Spectroscopy:** Spectroscopic techniques where atomic or molecular transitions are monitored through the variation of current of an electrical discharge when this is irradiated by resonant radiation.

**Optoacoustic Spectroscopy:** Spectroscopic techniques where atomic or molecular transitions are monitored through the detection of an acoustic wave produced by absorption of radiation.

**Saturation:** The condition reached in a two-level system in presence of resonant radiation when the populations of the two levels become equal.

**Spectral Line:** The response of a gas-phase sample obtained from the emission or absorption of radiation when the frequency is tuned around an atomic or molecular transition.

**Spectroscopy:** The branch of physics concerning the measurement of the emission and absorption spectra of atoms and molecules. According to the frequency range of the electromagnetic radiation, we speak of vacuum ultraviolet, ultraviolet, visible, infrared, or microwave spectroscopy.

**Spectrum:** The set of lines recorded after emission or absorption of radiation.

**Time-Resolved Spectroscopy:** Spectroscopic techniques that allow one to investigate fast relaxation processes involving the levels excited with a short-pulse laser.

**Two-Photon Spectroscopy:** Spectroscopic technique where a transition forbidden in the dipole approximation can be induced by the absorption of two counter-propagating photons.

## Works Cited


Abella, I. D. (1962), *Phys. Rev. Lett.* **9,** 453–455.

Amin, S. R., Caldwell, C. D., Lichten, W. (1981), *Phys. Rev. Lett.* **47,** 1234–1238.

Andrä, H. J. (1975), in G. zu Putlitz, E. W. Weber, A. Winnacker (Eds.), *Atomic Physics,* Plenum Press, New York.

Barbieri, B., Beverini, N., Sasso, A. (1990), *Rev. Mod. Phys.* **62,** 603–644.

Battaglia, A., Gozzini, A., Polacco, E. (1959), *Nuovo Cim.* **14,** 1076–1081.

Bell, A. G. (1881), *Philos. Mag.* **11,** 308.

Beverini, N., Giammanco, F., Maccioni, E., Strumia, F., Vissani, G. (1989), *J. Opt. Soc. Am. B* **6,** 2188–2193.

Bjorkholm, J. E., Liao, P. F. (1974), *Phys. Rev. Lett.* **33,** 128–131.

Bjorkholm, J. E., Liao, P. F. (1976), *Phys. Rev. A* **14,** 751–760.

Bloembergen, N., Levenson, M. D., Salour, M. M. (1974), *Phys. Rev. Lett.* **32,** 867–869.

Brossel, J., Cagnac, B., Kastler, A. (1954) *J. Phys. Radium* **15,** 6–8.

Bruzzese, R., Sasso, A., Solimeno, S. (1989), *Riv. Nuovo Cimento* **12** (7).

Cagnac, B., Grynberg G., Biraben, F. (1973), *J. Phys. (Paris)* **34,** 845–858.

Chu, S., Wieman, C. (Eds.) (1989), Special issue on Laser Cooling and Trapping of Atoms, *J. Opt. Soc. Am. B* **6,** 2018–2278.

Corney, A. (1977), *Atomic and Laser Spectroscopy,* Clarendon Press, Oxford.

de Angelis, M., Inguscio, M., Julien, L., Marin, F., Sasso, A., Tino, G. M. (1991), *Phys. Rev. A* **44,** 5811–5819.

Demtroeder, W. (1981), *Laser Spectroscopy,* Springer Series in Chemical Physics, Springer-Verlag, Berlin Heidelberg.

Ernst, K, Inguscio, M. (1988), *Riv. Nuovo Cim.* **11** (2).

Evenson, K. M. (1981), *Faraday Disc. R. Soc. Chem.* **71,** 7–14.

Fornaca, G., Gozzini, A., Strumia, F. (1963), in R. Servant, A. Charru (Eds.), *Electronic Magnetic Resonance and Solid Dielectric,* North Holland Publ. Comp., Amsterdam, p. 554.

Gianfrani, L., Sasso, A., Tino, G. M., Marin, F. (1991), *Nuovo Cim. D* **13,** 1221–1234.

Goeppert-Mayer, M. (1931), *Ann. Phys. (Leipzig)* **9,** 273–294.

Hänsch, T. W., Toschek, P. (1970), *Z. Phys.* **236,** 213–244.

Hänsch, T. W., Levenson, M. D., Schawlow, A. L. (1971), *Phys. Rev. Lett.* **26,** 946–949.

Hänsch, T. W., Schawlow, A. (1975), *Opt. Commun.* **13,** 68–69.

Hänsch, T. W. (1977), in: N. Bloembergen (Ed.), *Proceedings of the International School of Physics "Enrico Fermi," Course LXIV, Nonlinear Spectroscopy,* Amsterdam: North-Holland, p. 17.

Hänsch, T. W., Lee, S. A., Wallenstein, R., Wieman, C. (1975a), *Phys. Rev. Lett.* **34,** 307–309.

Hänsch, T. W., Schawlow, A., Series, G. W. (1975b). *Sci. Am.* **240** (3), 94–110.

Hurst, G. S., Payne, M. G., Kramer, S. D., Young, J. P. (1979), *Rev. Mod. Phys.* **51,** 767–819.

Letokhov, V. S., Chebotaev, V. P. (1977), *Nonlinear Laser Spectroscopy,* Springer Series in Optical Science, Springer Verlag, Berlin, Heidelberg, New York.

McFarlane, R. A., Jr., Bennet, W. R., Jr., Lamb, W. E. (1963), *Appl. Phys. Lett.* **2,** 189–190.

Meystre, P., Stenholms, S., (Eds.) (1985), special issue on Mechanical Effects of Light, *J. Opt. Soc. Am. B* **2,** 1706–1860.

Minguzzi, P., Profeti, S., Tonelli, M., di Lieto, A. (1982a), *Opt. Commun.* **42,** 237–240.

Minguzzi, P., Tonelli, M., Carrosi, A. (1982b), *J. Mol. Spect.* **96,** 294–305.

Penning, F. (1928), *Physica (The Hague)* **8,** 13–23.

Pinard, M., Aminoff, C. G., Laloë, F. (1979), *Phys. Rev. A* **19,** 2366–2370.

Raab, E., Prentiss, M., Cable, A., Chu, S., Pritchard, D. (1986), *Phys. Rev. Lett.* **59,** 2631–2634.

Shapiro, S. L. (1977), *Ultrafast Light Pulse,* Topics in Applied Physics, Vol. 18, Springer, Berlin, Heidelberg, New York.

Siegman, A. E. (1971), *An Introduction to Lasers and Masers,* McGraw-Hill, New York.

Sorem, M. S., Schawlow, A. L. (1972), *Opt. Commun.* **5,** 148–151.

Svanberg, S. (1992), *Atomic and Molecular Spectroscopy,* Springer Series on Atoms and Plasma, Springer-Verlag, Berlin, Heidelberg.

Svelto, O. (1976), *Principles of Lasers,* Plenum Press, Heyden, London, New York.

Szöke, A., Javan, A. (1963), *Phys. Rev. Lett.* **10,** 521–524.

Tam, A. C. (1986), *Rev. Mod. Phys.* **58,** 381–431.

Teets, R. E., Kowalski, F. V., Hill, W. T., Carlson, N. W., Hansch, T. W. (1977), in: A. H. Zewail (Ed.), *Advances in Laser Spectroscopy I,* SPIE Proceedings No. 113, Bellingham, WA: SPIE, p. 409.

Vasilenko, L. S., Chebotaev, V. P., Shishaev, A. V. (1970), *Zh. Eksp. Teor. Fiz. Pis'ma Red.* **12,** 161–165 [*JETP Lett.* **12,** 113–116].

Yariv, A. (1975), *Quantum Electronics,* Wiley, New York.

Wieman, C., Hänsch, T. W. (1976), *Phys. Rev. Lett.* **36,** 1170–1173.

Wineland, D., Dehmelt, H. (1975), *Bull. Am. Phys. Soc.* **20,** 637.

## Further Reading

Corney, A. (1977), *Atomic and Laser Spectroscopy,* Clarendon Press, Oxford.

Demtroeder, W. (1981) *Laser Spectroscopy,* Springer Series in Chemical Physics, Springer-Verlag, Berlin, Heidelberg.

Svanberg, S. (1992), *Atomic and Molecular Spectroscopy,* Springer Series on Atoms and Plasma, Springer-Verlag, Berlin, Heidelberg.

Svelto, O. (1976), *Principles of Lasers,* Plenum Press, Heyden, London, New York.

Yariv, A. (1975), *Quantum Electronics,* Wiley, New York.

# SPECTROSCOPY, MOLECULAR

See MOLECULAR SPECTROSCOPY

# HIGH SENSITIVITY TRACE GAS MONITORING USING SEMICONDUCTOR DIODE LASERS

C. Corsi[†], and M. Inguscio[††]

[†]Università degli Studi di Firenze
Dipartimento di Neuroscienze
Viale Pieraccini 6
50139 Firenze, Italy

[††]European Laboratory for Nonlinear Spectroscopy (LENS) and
INFM-Istituto Nazionale Fisica della Materia
Largo E. Fermi 2
50125 Firenze, Italy

## 1. INTRODUCTION

In recent years semiconductor diode lasers in the visible near-infrared have been applied to high sensitivity gas detection for a variety of environmental, medical and industrial applications.

The advantage of laser-based gas sensor with respect to conventional electro-chemical and semiconductor point sensors resides in their characteristics of non-intrusiveness, high gas selectivity, high detection speed and low cost.

In particular, great attention has been attracted by InGaAs-InP Distributed Feed-Back (DFB) diode lasers, operating at room temperature. Thanks to the knowledge and technology developed for telecommunication diode lasers emitting around 1.3μm and 1.5μm, these lasers can be easily designed to emit single mode almost anywhere in the region between 1μm and 2μm.

This spectral region is of particular interest because of the presence of molecular overtone vibrational bands for many important gases, like for instance, $CO_2$, CO, $H_2S$, HCl, HF, $NH_3$, $CH_4$, $H_2O$, NO, $N_2O$.

Although the transition strengths are at least one order of magnitude weaker than those for the fundamental bands in the mid-infrared, this problem is compensated, in real applications, by the advantages coming from the reduced opacity of the atmosphere and from the possibility of connecting the lasers with optical fiber systems, developed for telecommunication purposes.

Furthermore diode lasers are particularly suited for high-sensitivity absorption spectroscopy because they show much smaller amplitude noise than most other laser sources. In addition, diode lasers can easily be modulated at frequencies up to several GHz.

*Optical Sensors and Microsystems: New Concepts, Materials, Technologies*
Edited by Martellucci et al., Kluwer Academic / Plenum Publishers, New York, 2000.

This allows to apply various detection techniques[1,2,3] such as low-wavelength modulation spectroscopy (LWM) and frequency modulation spectroscopy (FM)[4,5] depending on the sensitivity level necessary to be reached.

In principle, sensitivities near to the fundamental quantum limit (shot-noise limit) are possible. In practice, quantum-limited sensitivity has proven to be difficult to obtain, due to a number of technical noise sources.

The noise sources can be divided in detector noise, noise due to amplitude fluctuations of the laser field and optical noise due to interference fringes.

### 1.1 Detector noise

There are three major components in a photodetector noise: Johnson (thermal) noise, detector shot noise, and 1/f-noise.

Johnson noise is due to the thermal fluctuations of the charge carrier density within the resistor itself. The thermal noise current can be expressed as:

$$i_T = \left( \frac{4KT\Delta\nu}{R} \right)^{\frac{1}{2}} \qquad (1)$$

where $K$ is the Boltzmann constant, $T$ the temperature, $\Delta\nu$ the detection bandwidth and $R$ the detector system resistance. The Johnson noise has a white frequency spectrum and can be reduced by cooling the detector.

Shot noise is due to quantum fluctuations of the radiation field. They give rise to fluctuations of the detected current in a photodetector and can be expressed by:

$$i_S = \left( 2e \cdot \frac{eP\eta}{h\nu} \cdot \Delta\nu \right)^{\frac{1}{2}} \qquad (2)$$

where $e$ is the electronic charge, $\eta$ is the quantum efficiency of the detector, $P$ is the incident power and $\nu$ is the photon energy. Shot noise is also white and independent of the modulation frequency but is proportional to the square root of the laser power. For optical powers in the mW range the output noise-voltage of the photodetector is dominated by shot noise rather than by Johnson noise.

Often devices show various sources of other noise mechanisms. In many cases this additional noise shows a 1/f dependence, but unfortunately no theoretical analysis are available. An empirical expression for the 1/f noise current is given by:[6]

$$i_{1/f} = \left( \frac{C \cdot \Delta\nu}{f^a} \right)^{\frac{1}{2}} \left( \frac{eP^b\eta}{h\nu} \right) \qquad (3)$$

where $C$ is a proportional factor, $a$ and $b$ are constants close to unity. The 1/f noise depends on the manufacturing processes, in particular on electric contacts and surfaces. It dominates the detector noise for frequencies below 1 kHz and drops below the Johnson and shot noise levels at higher frequencies. The rms 1/f noise current shows an approximately linear dependence on the photocurrent and therefore on the light intensity.Since all three detector noise sources depend on the detection bandwidth $\Delta\nu$ a reduction of the bandwidth results in a noise-reduction. It is also convenient to work at higher frequencies where the 1/f-detector noise has become lower than the shot noise.

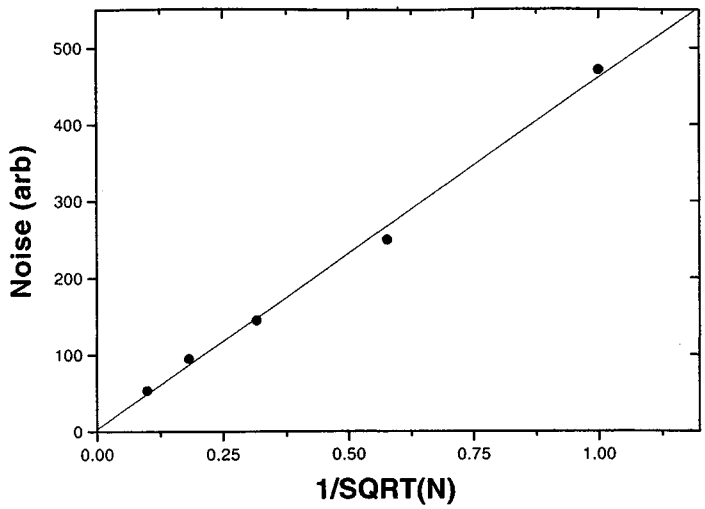


**Figure 1.** Improving the signal to noise ratio decreasing the detection bandwidth, by means of signal averaging. In figure the signal noise is plot versus the inverse of the square root of the number of averages, which is proportional to the detection bandwidth, for a DFB laser at 1578 nm.

## 1.2 Laser Excess Noise

In practice, the sensitivity of absorption measurements is often limited by excess-noise which is due to fluctuations of the laser power. The fluctuations are generated by external effects like current and temperature instabilities, mechanical vibrations, or optical feedback as well as by intrinsic noise sources, such like photon and carrier density fluctuations and partition noise. The external noise sources can be minimized by battery-driven or highly stabilized current sources together with proper alignment, ar-coatings, and optical isolators. The intrinsic noise depends mostly on the manufacturing process and design and on the operating conditions, like temperature and current.

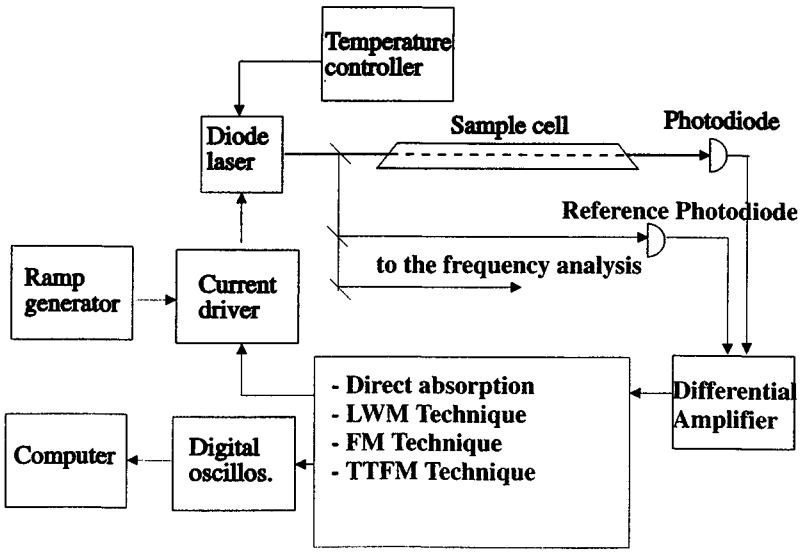


**Figure 2.** Schematic view of a laboratory set-up for a semiconductor diode laser spectrometer.

Several investigations of amplitude-noise characteristics of lead-salt lasers[7] and DFB and DBR-lasers[8] have shown that in most cases the laser excess-noise exhibit a 1/f dependence with cut-off frequencies ranging between 1 and 100 Mhz. The rms current at the detector caused by the laser-excess noise can be expressed as:

$$i_{ex} = \left(\frac{\Delta\nu}{f^{a}}\right)^{\frac{1}{2}} \left(\frac{eP_{ex}\eta}{h\nu}\right) \qquad (4)$$

where a defines the frequency dependence of the laser-excess noise and ranges between 0.8 and 1.5, $P_{ex}$ defines the magnitude of the laser power fluctuations at 1 Hz in a 1 Hz detection bandwidth. $P_{ex}$ is approximately proportional to the laser power and depends on the intrinsic noise of the diode laser and on the external effects of the particular measurement system. As in the case of detector noise, laser excess noise is detection bandwidth dependent and can be reduced with appropriate techniques.

### 1.3 Residual Amplitude Modulation

Frequency modulation of diode lasers results in a simultaneous amplitude modulation, since not only the wavelength depends on the current but also the laser power. This residual amplitude modulation (RAM) becomes often the main noise source in high-sensitive absorption measurements. The RAM can be reduced using a dual beam subtraction method, in which the laser beam is split in a reference beam and a probe beam, which are detected by the same kind of photodiodes.

It is important that the amplifier have the same quantum efficiency, the same gain and the same frequency response. Therefore all electronic components have to be selected with great care to avoid manufactural differences of photodiodes and electric components, such as resistance, operational amplifiers and capacities.

### 1.4 Interference Fringes

Every transmitting element in the optical path, such as beamsplitters, lenses, absorption cell windows or the laser collimator itself can create Fabry-Perot fringes. These optical fringes often exhibit a free spectral range (FSR) comparable to the linewidth of absorption lines when the laser is scanned across the lines. They appear as periodic oscillations with sufficient amplitudes to obscure weak absorptions signals. Interference fringes arise from reflections between parallel surfaces in the optical path and the transmission depend on the laser wavelength. Any scanning of the wavelength results in an amplitude variation if resonant structures appear in the path. The free spectral range between two fringes can be expressed as:

$$FSR = \frac{c}{2nl} \qquad (5)$$

where $n$ is the refractive index of air and $l$ is the distance between the optical surfaces. The distance $l$ ranges typically between 1 m and 5 mm, which corresponds to resonances at a distance of 150 MHz and 30 GHz, respectively.

There are several possibilities to minimize these etalon effects. For example, if the free spectral range of the fringes is very different compared to the width of the absorption feature they can be removed by filtering the detected signal. However, for spacings comparable to the linewidths the fringes can only be removed by a careful design of the experimental set-up.

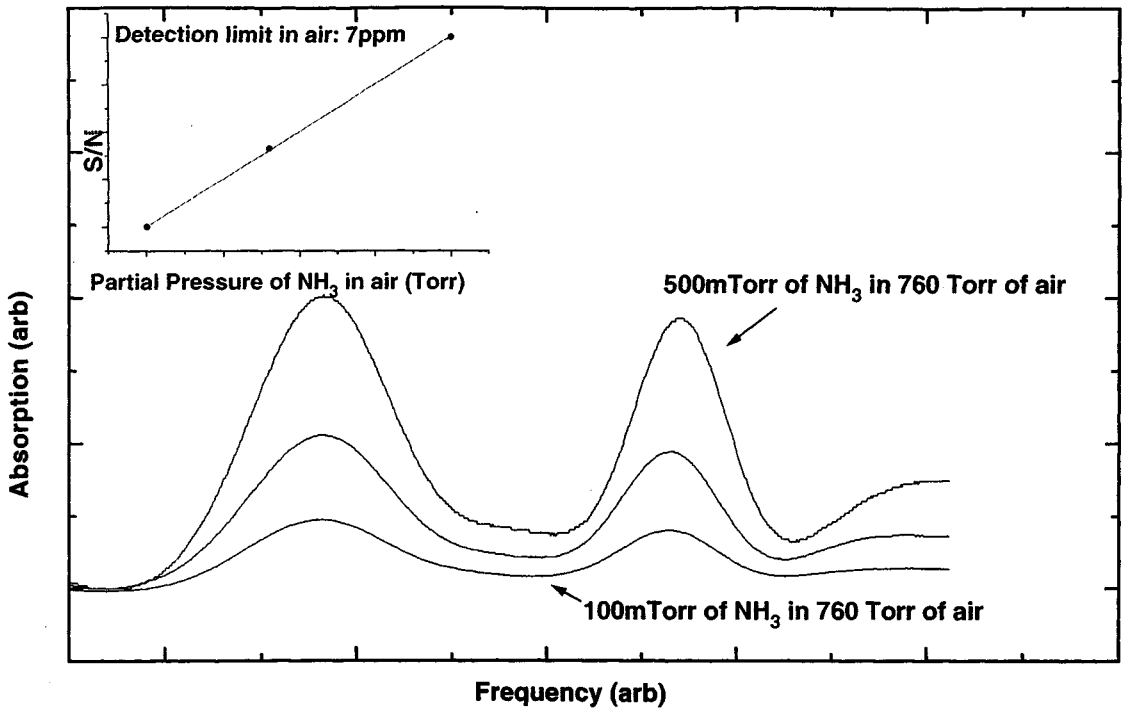


**Figure 3.** Second derivative profiles of different pressures of $NH_3$ in air: a detection limit of 7 ppm×m in air is extrapolated. The combination band of ammonia at 1.5μm is investigated, with a laser at 1494 nm.

Whenever possible, transmissive optics should be avoided or anti-reflection coated optics should be used.

It is important to note that only detector 1/f noise and laser excess noise depend on the detection frequency, while all noise sources discussed so far depend on the detection bandwidth $\Delta\nu$. Therefore, high sensitivity detection can be achieved by increasing the detection frequency (to a value for which the laser excess noise is lower than the shot- and Johnson noise) and by reducing the detection bandwidth.

## 1.5 Detection Techniques

In general, in a direct absorption measurements, the small changes in the transmitted amplitude, arising from gas traces, have to be distinguished on a large background, resulting in a poor sensitivity.

Frequency modulation techniques are based on a fast modulation of the laser emission in the frequency domain resulting in an amplitude modulation of the ligth intensity. By means of phase sensitive detection is then possible to extract only the absorbed signal from the background of the transmitted power. An additional increase in sensitivity is due to the fact that the detection frequency can be moved to larger values, in order to reduce the laser amplitude fluctuations.

The modulation techniques are divided according to the modulation frequency.

In low wavelength modulation spectroscopy (LWM), the laser frequency is modulated at a relatively low frequency (hundreds of kHz), which is small compared to the width of the line to be probed. The observed signal arises from the difference in the absorption of different sidebands which probe simultaneously the absorption line. The signal is then demodulated, at n times the modulation frequency. Usually, first (n=1) and second (n=2) derivative detection are used.

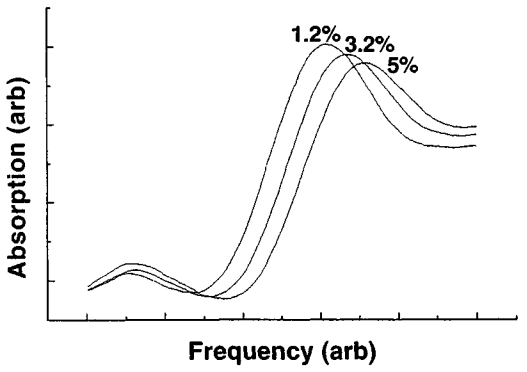


**Figure 4.** Second derivative absorption signal of CO at the exit of a catalytic exhaust with a DFB laser at 1578 nm.

In frequency modulation spectroscopy (FM), the laser is modulated at much higher frequencies, that range usually between 100 MHz and several GHz, comparable with the width of the absorption features, and produce sidebands which are widely spaced in frequency. In this technique, only one sideband is absorbed at a time, giving rise to a heterodyne beat signal at the modulation frequency. The detection frequency is moved in a region where the laser excess noise presents its minimum value and, in addition, the selective absorption of the sidebands results in a larger detected signal.

In order to retain a similar sensitivity for atmospheric pressure broadened absorption profiles, the laser must be modulated at frequencies in excess of one Ghz. Electronics for heterodyne detection at these frequencies can be complicated. The problem can be simplified by using two-tone frequency modulation spectroscopy (TTFM).[9] The laser emission is simultaneously modulated at two distinct but closely spaced frequencies, $\nu_1+\nu_2$ and $\nu_1-\nu_2$, once more comparable to the line-width of interest ($\nu_1$~a few GHz for pressure broadened profiles and $\nu_2$~few MHz). The heterodyne beat signal is then obtained at the much lower frequency $2\nu_2$, eliminating the need of high speed detectors and electronics. Such detection frequency can be anyway maintained sufficiently large (a few MHz) to avoid the 1/f excess noise and reach the same noise level as in the FM technique.

It has to be noted that such high modulation frequency can be obtained only in semiconductor diode laser by means of the injection current. Electro-Optical modulators (EOM) could be a possible solution for other laser sources, but efficient modulation at frequencies above 1 GHz are not very easy to be reached.

Further improvement in sensitivity can be obtained by means of a double beam configuration, in which amplitude fluctuations can be canceled out, achieving a shot-noise limited detection.

### 1.6 Bandwidth reduction

Another important parameter that greatly influences the sensitivity of the apparatus is the electronic detection bandwidth of the signal. Indeed, many noise sources (shot-noise, Johnson noise, laser excess noise) depend on it, in particular they decrease proportionally to the square root of the bandwidth.

For example, an appropriate filtering of the signal can result in an enhancement of the sensitivity. In addition, by means of a signal averaging, the noise can be further reduced, as if the bandwidth was decrease according to the relation:[7]

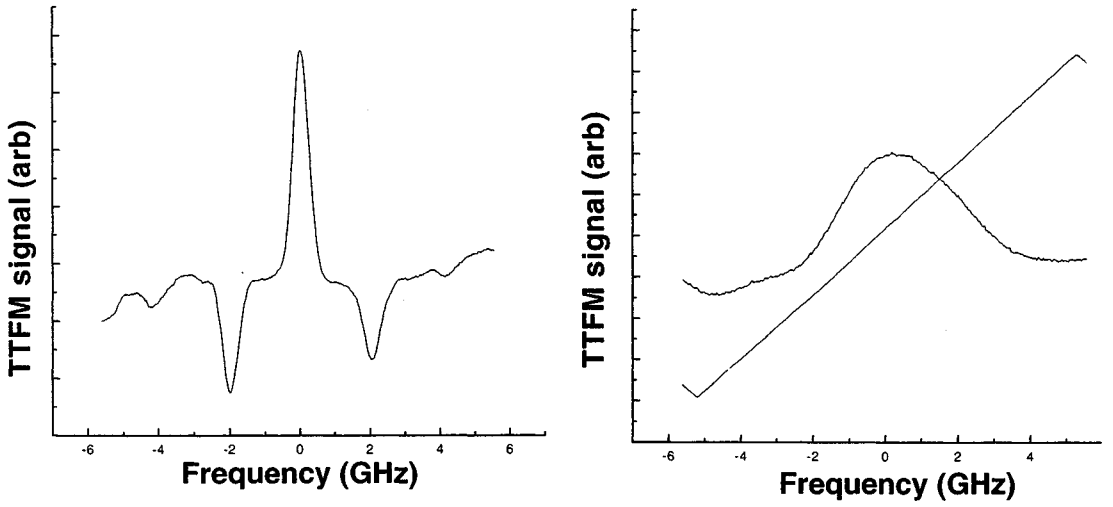


**Figure 5.** Two-tone signal from 90 mTorr of pure $H_2S$ and b) in an atmosphere of air (1Hz detection bandwidth), with a DFB laser at 1578 nm.

$$\Delta\nu_{eff} = \frac{\Delta\nu}{n} \tag{6}$$

where $n$ is the number of averages. This effect has been verified experimentally with a DFB diode laser at 1578 nm, as can be seen in Figure 1.

## 2. EXPERIMENTAL SET-UP

In Figure 2. an experimental laboratory setup of a typical tunable diode laser sensor is shown. Different diode lasers are used, depending on the gas under study. The emission frequency is selected with an appropriate control of laser temperature and current in order to match the chosen molecular line. A current ramp of about 10 mA amplitude is added to the injection current, leading to continuous sweep of the laser frequency of several GHz, which allows to record the whole selected line with one current scan.

The output beam of the laser is collimated and splitted into three parts: one is used for the frequency control, the second one is used to detect the unabsorbed light intensity and the third one is used to detect the transmitted light intensity.

The absorbed and reference signals are amplified and subtracted from each other to avoid the background slope due to the amplitude modulation produced by the current scan.

The sample cell, a 1.5 m long Pyrex tube, is pumped out to $10^{-4}$ Torr and filled with the gas sample.

This simple experimental set-up is used to extract atmospheric relevant broadening parameters with the advantage of a straightforward interpretation of the broadened absorption profile.[10]

For high sensitivities measurements LWM and TTFM techniques are used.

In the low wavelength modulation apparatus an ac component at $\omega_0$=3.5 kHz is added to the injection current, the absorbed signal is demodulated at a frequency $2\omega_0$ by means of a lock-in amplifier.

In the two-tone frequency modulation scheme the signal from a synthesizer at $\nu_1$=2.04 GHz is mixed with that at $\nu_2$=5.35 MHz of a function generator.

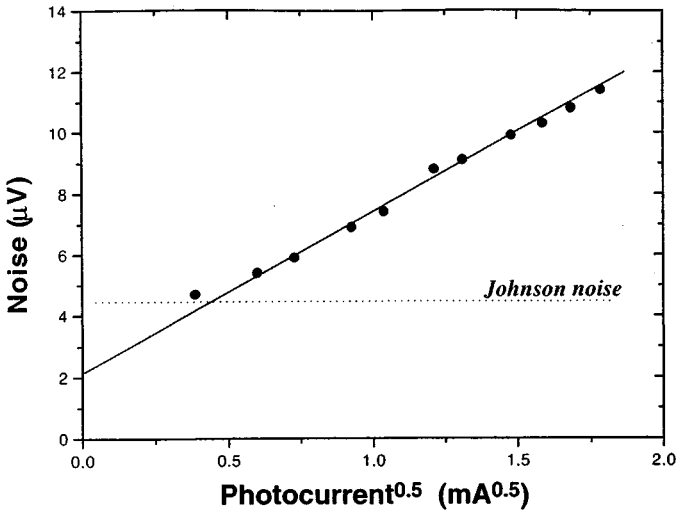


**Figure 6.** Noise power as a function of the optical power incident on the photo-detector. The linear dependence indicates that the sensitivity is shot-noise limited, since other noisesources depend in a different way on the optical power.

The output, at $\nu_{mod}$=2 Ghz±5.35 MHz is coupled to the laser diode current by means of a high pass filter. The signal of the function generator is frequency doubled and is mixed in a phase detector with the filtered and amplified absorption signal coming from an InGaAs-PIN photo-diode. The output of the phase-detector, which is proportional to the Fourier component of the signal from the photo-diode at $\nu_{det}$, is low pass filtered (100 Hz), amplified and recorded on a digital oscilloscope.

To perform a quantum limited detection a careful attention to experimental details like amplifiers has to be paid. In particular, for the balanced dual-beam set-up used in our application, it is of fundamental importance that the probe signal and the reference signal are detected with the same kind of photo-diodes and amplified with the same kind of amplifiers.

**Table 1.** Comparison between minimum detectable concentrations in air obtained with different detection techniques.

| | $\lambda$ | Detection limit in air | | |
|---|---|---|---|---|
| | nm | ppm×m | | |
| $NH_3$ | 1494.35 | | 7 (LWM) | |
| CO | 1579.74 | 500 (AD) | 170 (LWM) | 7 (TTFM) |
| $CO_2$ | 1579.57 | 800 (AD) | 260 (LWM) | 10 (TTFM) |
| $H_2S$ | 1577.32 | 400 (AD) | 130 (LWM) | 4 (TTFM) |
| $O_2$ | 760.89 | | 1000 (LWM) | |
| HCl | 1742.3 | | 0.5 (LWM) | |

To avoid manufactural differences of resistances or capacitance they have to be tested and chosen carefully. For that reason a low-noise pre-amplifier circuit for the photo-diodes was especially designed to work for detection frequencies between 1 and 40 MHz.

The preamplified output signals of the photo-detector are combined in a 180° rf hybrid, which shifts one signal by 180° before adding it to the other one, eliminating in this way all coherent fluctuations of the two beams. A quantitative description of our quantum limited dual beam spectrometer can be found elsewhere.[11]

With all the detection techniques listed before a series of signal to noise ratio measurements at different total and partial gas pressures are performed. The minimum detectable gas pressure is then obtained by a nonlinear fitting procedure, extrapolating the value at which the signal to noise ratio becomes unity.

## 3. RESULTS AND DISCUSSION

The sensitivity limits from the three detection techniques are reported using the absorption lines of some interesting molecules in the 1μm-2μm region (Table 1.).

### 3.1 Ammonia $NH_3$

The combination band $\nu_1+2\nu_4$ at 1.5μm has been investigated. Low wavelength modulation spectroscopy has been performed on the strongest component at $\lambda$ = 1494.35 nm using a DFB diode laser (Fig.3). A minimum detectable concentration of 7 ppm×m of ammonia in air has been achieved.This low detection limit is important for monitoring the $NH_3$ concentration in various applications. Selective Catalytic Reduction (SCR) of $NO_x$ with ammonia represents the most effective technology currently available for deep $NO_x$ removal. Furthermore, alteration in $NH_3$ concentration in the breath can indicate severe epatic failure.

### 3.2 Carbon Monoxide CO, Carbon Dioxide $CO_2$ and Hydrogen Sulphide $H_2S$

These three molecules have, in the region around 1578 nm, overlapping overtone bands: 3ν (CO), $2\nu_1+2\nu_2+\nu_3$ ($CO_2$)[12] and $\nu_1+\nu_2+\nu_3$ ($H_2S$)[13]. By using one single semiconductor diode laser and a TTFM scheme, a minimum detectable absorption of $5\times10^{-7}$ is achieved. This corresponds at a minimum detectable concentration in air of 7 ppm×m for CO, 10 ppm×m for $CO_2$ and 4 ppm×m for $H_2S$.

CO and $CO_2$ are important in combustion processes and exhaust gases control (Figure 4.), while $H_2S$ detection is fundamental for security on sour-oil-rigs (Figure 5.).

Furthermore a TTFM spectrometer is a powerful tool for non-invasive diagnostic of human breath, where detection of the isotopic ratio $^{12}CO_2/^{13}CO_2$ can give information of the presence of Helicobacter Pylori in the stomach.

### 3.3 Molecular Oxygen $O_2$

A magnetic dipole transition of the $b^1\Sigma_g^+$ (ν'=0)←$X^3\Sigma_g^-$ (ν''=0)--band at 761nm is studied. A low wavelength modulation scheme is used, but a sensitivity of only 1000 ppm×m is achieved, because the transitions' line-strengths in this forbidden band are more than one order of magnitude weaker than those of the other molecules investigated.

**Table 2.** Self-broadening and Air-broadening coefficients for the gases under study (* measured at 1.65 μm).

| | λ | Self-broadening | Air-broadening |
|---|---|---|---|
| | (nm) | (MHz/Torr) | (MHz/Torr) |
| $NH_3$ | 1494.35 | 37(3) | 4.0(2)* |
| CO | 1579.74 | 3.95(9) | 3.67(8) |
| $CO_2$ | 1579.57 | 4.1(3) | 3.42(7) |
| $H_2S$ | 1577.32 | 6.7(2) | 3.09(9) |
| $O_2$ | 760.89 | 2.04(2) | 1.92(5) |
| HCl | 1742.3 | 8.6(4) | 2.9(5) |

### 3.4 Hydrogen Chloride HCl

The first overtone band (2ν) at 1.77μm is investigated[14] with a low wavelength modulation and two-tone frequency modulation apparatus. Sensitivity of 0.5 ppm×m is reached. Monitoring of HCl is very important in the emitted gases of waste incinerator.

For the shot-noise limited detection the absorption spectrometer has been tested using $H_2S$ as a target gas, once the noise sources are minimized and the optimal working conditions are found. We have measured the rejection ratio using the difference method.

We have demonstrated that the used dual beam configuration can suppress laser noise by more than 25 dB, in the region of interest near 10 MHz. Then we have measured the difference of the two channels, using the 180° combiner, and the sum using the 0° combiner, that is only 5 dB over the difference. So, taking in account the rejection ratio we concluded that we have reached the shot-noise level. The detection limit of $H_2S$ in air was found to be approximately 500 ppb over 1 meter path-length.

As an additional check to the reached shot-noise limit, the light noise was measured as a function of the square root of the optical power incident on the photo-detector (see Figure 6.). In addition, pressure broadening parameter are measured for all these molecules. Results are listed in Table 2.

## 4. CONCLUSION

The achieved quantum limited sensitivity demonstrate that using distributed feedback diode lasers in combination with two-tone frequency modulation spectroscopy is a powerful technique for gas detection. It is possible to detect traces gases in air with a sensitivity on a ppm-level over a 1-meter path-length for some molecules of industrial, medical and environmental interest.

The natural combination with fiber optics technology make these sensors attractive for a large variety of "in situ" measurements.

ACKNOWLEDGMENTS. Many collegues and visitors have contributed to the progress in diode laser spectroscopy at Lens. We are indebted to them all: R. Benedetti, F. D'Amato, P. De

Natale, M. De Rosa, K. Ernst, M. Gabrysch, K. Giulietti, L. Lorini, F. Marin, G. Modugno, F.S. Pavone, N. Pique, M. Prevedelli, M. Snels.

We want to thank Prof. M. Rosa-Clot and SIT (Science Industry and Technlogy) for stimulating help in the transfer of our knowledge to industry.

This work has been supported by ASI contract ARS96107, ECC contract ERB FMGE CT 950017 and the Fire & Gas project N. OG-0269-95.

## REFERENCES

1. F.S. Pavone, "Diode lasers and their applications in spectroscopy", *Rivista del Nuovo Cimento*, **Vol 19**: 1-42(1996)
2. F.S. Pavone, M. Inguscio, "Frequency- and Wavelength-Modulation Spectroscopies: Comparison of Experimental Methods Using an AlGaAs Diode Laser", *Appl. Phys. B*, **56**:118-122 (1993)
3. M. Gabrysch, "High-Sensitivity Spectroscopy Using Semiconductor Diode Laser in the Visible and Near Infrared Spectral Region", Ph.D. Thesis, Heidelberg 1997
4. G.C. Bjorklund, "Frequency-modulation spectroscopy: a new method for measuring weak absorptions and dispersions", *Opt. Lett.* **5**, no.1: 15-17 (1980)
5. J.A. Silver, "Frequency-modulation spectroscopy for trace species detection: theory and comparison among experimental methods", *App. Opt.*, **31** no. 6: 707-717 (1992)
6. H.I. Schiff, G.I. Mackay, J. Bechara "Air Monitoring by Spectroscopic Techniques", John Wiley & Sons (1994)
7. P. Werle, F. Slemr, M. Gehrtz and C. Brauchle, "Quantum limited FM-spectroscopy with a lead salt diode laser", *Appl. Phys.* **B 49**: 99 (1989)
8. W.H. Richardson, Y. Yamamoto, "Quantum correletion between the junction-voltage fluctuation and the photon-number fluctuation in a semiconductor laser", *Phys. Rev. Lett.* **66**, 1963 (1991)
9. G.R. Janik, C.B. Carlisle, T.F. Gallagher, "Two-tone frequency-modulation spectroscopy", *J. Opt. Soc. Am.*, **B3**: 1070-1074 (1986)
10. C. Corsi, M. Gabrysch, M. Inguscio, "Detection of molecular oxygen at high temperature using a DFB-diode-laser at 761 nm", *Opt. Comm.*, **128**: 35-40 (1996)
11. C. Corsi, M. Gabrysch, F. Marin, G. Modugno "Quantum noise limited detection with semiconductor diode laser", *App. Phys. B*, special issue on "Environmental Trace Gas Detection Using Laser Spectroscopy" (1998)
12. M. Gabrysch, C. Corsi, F.S. Pavone, M. Inguscio, "Simultaneous detection of CO and $CO_2$ using a semiconductor DFB diode laser at 1.578 μm", *App. Phys. B*, **B65**: 75-79 (1997)
13. G. Modugno, C. Corsi, M. Gabrysch and M. Inguscio, "Detection of $H_2S$ at the ppm level using a telecommunication diode laser", *Opt. Comm.* in press
14. C. Corsi, S. Czudzynsky, F. D'Amato, M. De Rosa, K. Ernst, M. Inguscio, "Detection of HCl on the first and second overtones using semiconductor diode lasers at 1.7 μm and 1.2 μm", in press.

4

La Rivista del Nuovo Cimento
della Società Italiana di Fisica
1999

G. M. TINO and M. INGUSCIO

# Experiments on Bose-Einstein condensation

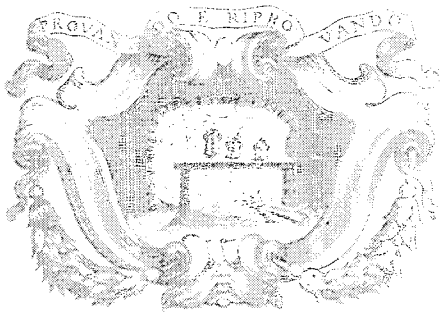

Editrice Compositori

Bologna

# La Rivista del Nuovo Cimento
## della Società Italiana di Fisica



Contribution to *Rivista del Nuovo Cimento* is by invitation only. Papers may be written in English, French, German, Italian or Spanish.
Manuscripts submitted for publication should be sent in duplicate and only to **The Director of Il Nuovo Cimento, via Castiglione 101, I-40136 Bologna, Italy**. Each copy, clearly type-written or printed, must be complete with a set of high-resolution original drawings and complete references according to the ISO style. A signed SIF copyright-transfer form should be included with the submission, and will be required before publication. Forms can be downloaded from the SIF www site (`www.sif.it`), where the style guide is available, together with the LaTeX macros to prepare the manuscript according to the style of *Il Nuovo Cimento*.
The electronic version of the paper in final form (exactly matching the paper version) can be sent to the Editorial Office in Bologna, either by e-mail at `cimento@sif.it` or on disquette at the address above. To ensure portability between the different installations and systems used it is highly recommended that authors adhere to the following guidelines:
• **TeX, LaTeX and plain text**. The files should contain only printable ASCII characters, *i.e.* with codes between 32 and 127. LaTeX with the package `cimento` (available at `www.sif.it`) is the preferred choice; standard LaTeX without low-level formatting is also good. All non-standard files necessary to process the document should be sent along with the paper. The files may be transmitted as simple e-mail messages, provided the line length does not exceed 80 characters per line and they do not contain characters with codes below 32 or above 127; otherwise an encoding is required.
• **MS-Word, WordPerfect, etc.** Use of word-processing software is discouraged; papers will undergo partial retyping (*e.g.* equations). The files produced should always be encoded. Sending as attachment should perform an automatic encoding.
• **Figures** should be in separate files, and so should be different parts of the same figure.
EPS (Encapsulated Postscript) is the recommended format for the figures. In order to produce the postscript files, whenever possible printer drivers ("printing to file") should be avoided in favour of translation/exportation. Program/driver options should be set for: no preview, ASCII encoding, EPS format. Postscript files should always be encoded for mailing.
TIFF, GIF, BMP, PICT and other common image formats are acceptable as well. They always require encoding.
• **Compression**. Large files should be archived and/or compressed before encoding with public domain software such as tar for archiving, gzip for compressing and uuencode for encoding. Other formats may be processed as well.
**Proof-reading** - Normally, proofs are sent to the author only once, unless second proofs are explicitly requested. In this case the author will be charged US$ 3 per page. Corrections should be made on proofs using clear conventional signs. (It is of no use to send corrected files, since original files have undergone changes during the production procedure.) The aim of proof-reading is to correct errors which might have appeared in the production procedure, not to modify the contents of the paper. Once proofs are corrected, they must be returned to the Editorial Office as soon as possible.
**Reprints** - Reprints can be requested by returning to the Editorial Office the filled-in form that is sent with the proofs. The costs of the reprints and of charges for author's corrections will be invoiced by **Editrice Compositori, via Stalingrado 97/2 - 40128 Bologna.**

G. M. TINO and M. INGUSCIO

# Experiments on Bose-Einstein condensation

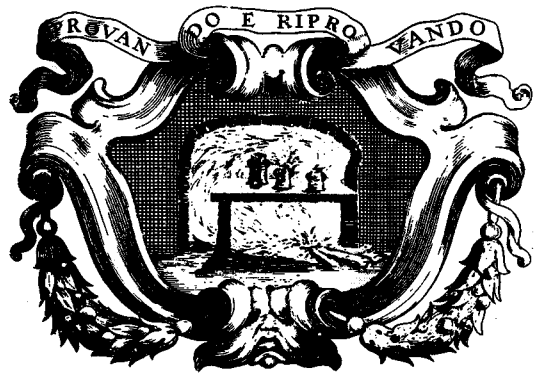

RIVISTA DEL NUOVO CIMENTO VOL. 22, N. 4 1999

# Experiments on Bose-Einstein condensation

G. M. TINO[1] and M. INGUSCIO[2]

([1]) *Dipartimento di Scienze Fisiche dell'Università di Napoli and Istituto Nazionale di Fisica della Materia, Complesso Universitario di Monte S. Angelo via Cintia, I-80126 Napoli (Italy)*

([2]) *Istituto Nazionale di Fisica della Materia, European Laboratory for Nonlinear Spectroscopy and Dipartimento di Fisica dell'Università di Firenze Largo E. Fermi 2, I-50125 Firenze (Italy)*

(ricevuto il 27 Maggio 1998)



## 1. – Introduction

Bose-Einstein condensation (BEC) is a purely quantum phenomenum first predicted by A. Einstein in 1924 [1, 2]. A gas of non-interacting identical particles described by a

 

wave function symmetric under the exchange of any two particles, should undergo a phase transition when the de Broglie wavelength becomes comparable to the spacing between particles. Under these conditions, the wave packets overlap and the indistinguishability of the particles becomes important. Particles described by a symmetric wave function are called bosons from S.N. Bose who was the first to study their statistical behaviour in the case of photons [3]. Bosons obey Bose-Einstein statistics. As is well known, the symmetrization postulate of quantum mechanics admits only another class of particles, those described by an antisymmetric wave function, which are called fermions and follow Fermi-Dirac statistics [4, 5]. If the temperature of a gas of bosons is lowered, below a transition temperature a macroscopic fraction of the particles should suddenly occupy the single lowest-energy quantum mechanical state. The condition for the transition is that $n\Lambda_{\mathrm{dB}}^3 = 2.612$ [6], where $n$ is the density of particles, and $\Lambda_{\mathrm{dB}} = h/\sqrt{2\pi m k_{\mathrm{B}} T}$ is the thermal de Broglie wavelength, with $h$ Planck's constant, $m$ the mass of particles, $k_{\mathrm{B}}$ Boltzmann's constant, and $T$ the gas temperature (the quantity $n\Lambda_{\mathrm{dB}}^3$ is usually called phase-space density and a system of identical particles for which $n\Lambda_{\mathrm{dB}}^3 \sim 1$ is referred to as a quantum-degenerate system). In fact, this prediction had never been tested directly although quantum degeneracy is at the origin of the behaviour of superfluid helium and exciton gases in semiconductors. A comprehensive review of experimental and theoretical work on BEC before 1995 can be found in [7].

In 1995, BEC was first observed directly by E. A. Cornell and collaborators in a gas of $^{87}$Rb atoms [8] and by W. Ketterle's group in a gas of Na atoms [9]. Evidence of BEC in a gas of $^{7}$Li was also reported in [10, 11]. These important results were achieved after several years of experimental efforts initially focused on atomic hydrogen. The observation of BEC in hydrogen was prevented by the presence of collisional processes leading to losses of atoms from the sample and by the difficulty in the detection of the atoms. In fact, the success of experiments of BEC on alkali atoms was the result of the combination of methods of magnetic confinement and evaporative cooling, mainly developed for hydrogen, with the techniques of laser cooling and trapping which are particularly efficient for alkali atoms. Also important was the occurrence of favourable collisional parameters and the possibility of easy optical diagnostics of the atomic sample.

This paper describes these recent experiments of BEC in dilute vapors of alkali atoms. Since the first observation of BEC, an amazing number of experimental and theoretical papers have been published. Because of this rapid development, it is impossible to give a complete bibliography and some of the results discussed here will necessarily become obsolete soon. An updated bibliography and information on recent results can be found at the Internet site http://amo.phy.gasou.edu:80/bec.html/. The purpose of this paper is to summarize the experimental methods that allowed the achievement of BEC, in several laboratories now, and to describe the main results obtained so far in the study of what can be considered as a new state of matter.

## 2. – Cooling and trapping of atoms

In recent years there was a dramatic progress in cooling and confinement of neutral atoms using electromagnetic fields. Cooling was achieved by using optical fields from laser sources (laser cooling) or by selective ejection of more energetic atoms from a trapping region using microwave radiation (evaporative cooling). Wall-free confinement of the cold atoms was accomplished by using laser beams (optical traps), by static or slowly varying magnetic fields (magnetic traps), or by a combination of the two (magneto-optical traps).

In this section we describe these cooling and trapping techniques with particular

emphasis on the methods which have been used so far to achieve Bose-Einstein condensation. The important "ingredients" of the experiments which have been successful so far are magneto-optical trapping, cooling in optical molasses, magnetic trapping, and evaporative cooling.

2·1. *Laser cooling and trapping of atoms.* – The field of laser cooling and trapping of atoms has been one of the most active fields of research in physics in the past decade. Starting from the initial proposals that dated back to the seventies, several methods were developed which allowed to reach lower and lower temperatures. The study of the cooling processes became of interest in its own right as new mechanisms were discovered. In 1997, the Nobel Prize in Physics was awarded to C. Cohen-Tannoudji, S. Chu and W. D. Phillips for their important contributions in the development of methods to cool and trap atoms with laser light. It is beyond the scope of this review to describe in detail the different methods developed and the results obtained by the many groups in the world that have been involved in the research in this field. In this section, we only briefly describe the techniques of laser cooling and trapping that were important in the experiments in which Bose-Einstein condensation was achieved. A comprehensive review on both experimental and theoretical work in this field can be found in [12-16].

2·1.1. Slowing of an atomic beam. When an atom with mass $m$ absorbs or emits a photon with frequency $\nu$, because of conservation of total momentum its velocity changes by the recoil velocity $v_r = h\nu/(mc) = h/(m\lambda)$. For the $D_2$ transition in sodium atoms, $\lambda = 589$ nm, $m = 23$ a.m.u., $v_r = 3$ cm/s. For cesium, $\lambda = 852$ nm, $m = 133$ a.m.u., $v_r = 3.5$ mm/s. This change in velocity is small but if several photons are scattered, a considerable change in the atomic velocity can result. For example, a sodium atom moving with a velocity $v_0 \sim 1000$ m/s interacting with a laser beam propagating in the opposite direction would stop after the absorption of $v_0/v_r \sim 33000$ photons. In the case of a thermal cesium beam ($v_0 \sim 300$ m/s) about 86000 photons are required to stop the atoms.

The absorption of each photon is followed by spontaneous emission. Because the emission direction is random, spontaneous emission has no effect, on the average, on the atomic velocity. The acceleration of the atom depends on the rate of scattering of photons. For high intensity of the light, an absorption-emission cycle requires a time of the order of the excited-state lifetime $\tau$. For the transitions considered above, $\tau \sim 20$ ns. Therefore atoms can be stopped in a few milliseconds.

In order to describe the process in more detail, a simple model can be considered of a two-level atom interacting with a plane light wave propagating in the direction $\mathbf{n}$ with frequency $\nu_L$ and intensity $I$ (fig. 1). The lower and upper states of the atom have energies $E_g$ and $E_e$, respectively, separated by the quantity $E_e - E_g = h\nu_A$.

The number of absorption-emission cycles in one second is given by the rate of spontaneous emission $1/\tau$ times the probability of occupation of the excited level, given by

$$p_e(\boldsymbol{v}) = \frac{1}{2}\frac{I/I_0}{1 + (I/I_0) + (4/\Gamma^2)[\delta - (\nu_L/c)\boldsymbol{v}\cdot\boldsymbol{n}]^2}, \tag{1}$$

where $\delta = \nu_L - \nu_A$, $I_0$ is the saturation intensity, and $\Gamma = 1/(2\pi\tau)$ is the natural width of the atomic resonance.

The effect of the exchange of momentum between the atom and the radiation field is that the atom experiences a force $\mathbf{F}_{sp}$ called spontaneous force or radiation pressure

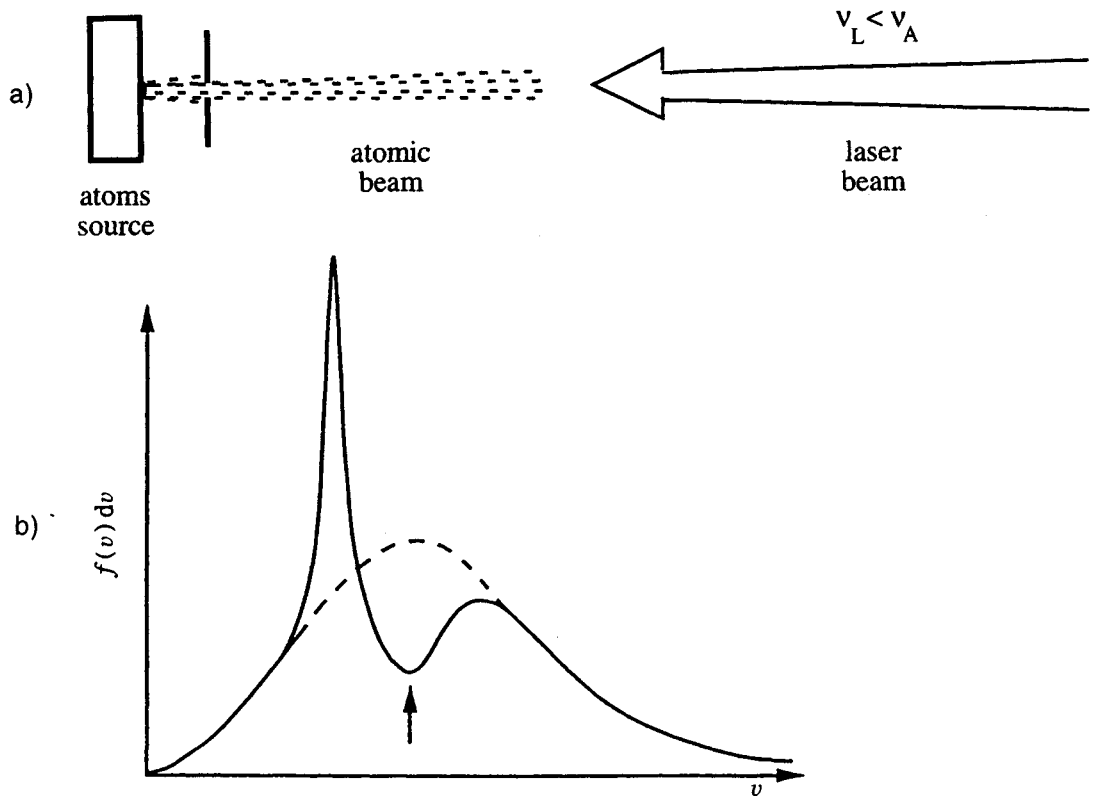


Fig. 1. – Slowing of an atomic beam using laser light. a) Simplified scheme of the apparatus; b) velocity distribution of the atoms with no laser (dashed line) and in the presence of a fixed-frequency counterpropagating laser beam (continuous line).

force. This force is given by the change of momentum of the atom in the unit of time, that is by the momentum of a photon times the number of absorption-emission cycles in the unit of time:

$$\mathbf{F}_{\mathrm{sp}}(\boldsymbol{v}) = \boldsymbol{n}\frac{h\nu_{\mathrm{L}}}{c}\frac{1}{2\tau}\frac{1}{2}\frac{I/I_0}{1+(I/I_0)+(4/\Gamma^2)[\delta-(\nu_{\mathrm{L}}/c)\boldsymbol{v}\cdot\boldsymbol{n}]^2}\,. \tag{2}$$

Equation (2) gives the average force on the atom over several absorption cycles. This expression is valid if changes of the quantity $\delta_{\mathrm{eff}} = [\delta - (\nu_{\mathrm{L}}/c)\boldsymbol{v}\cdot\boldsymbol{n}]^2$ can be neglected in the time interval considered.

Slowing of an atomic beam with a counterpropagating laser beam is efficient if the laser frequency is smaller than the atomic resonance frequency in order to compensate for the Doppler shift. As can be seen from eq. (2), the spontaneous force is most substantial when $[\delta + \nu_{\mathrm{L}}(v/c)] \ll \Gamma$. For a given laser frequency, only atoms with a velocity within an interval of width $\Delta v = \Gamma c/\nu_{\mathrm{L}}$, called the capture range, will be slowed down. Figure 1 shows the change in the atomic velocity distribution produced by a counterpropagating laser beam with frequency $\nu_{\mathrm{L}} < \nu_{\mathrm{A}}$. Atoms in the velocity capture range are slowed and their velocity distribution is narrower. Therefore, this scheme produces not only slowing but also cooling of the atoms. The problem of this scheme is that only a small fraction of the atoms interact with the laser. Also, the process stops when the atoms, because of the change in velocity, are no longer in resonance.

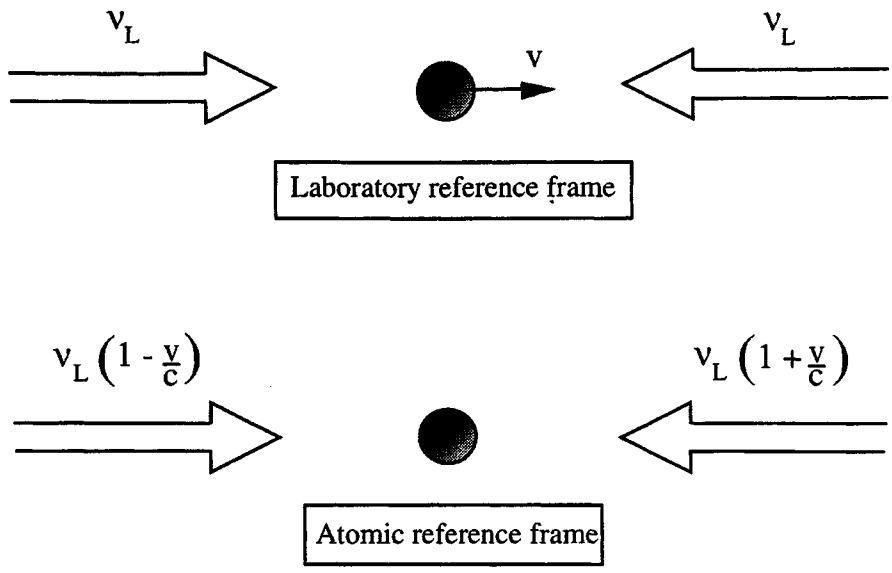


Fig. 2. – Scheme for 1-dimensional cooling of atoms in optical molasses.

Two methods have been devised to solve these problems. The first method is called laser chirping [17]: The laser frequency $\nu_L$ is changed in time, typically in the form of a succession of ramps, so that groups of atoms see the laser in resonance until they reach the final velocity. The second method exploits a static space-varying magnetic field to tune the frequency $\nu_A$ [18]. The advantage of the laser chirping method is its simplicity that does not require particular changes in the atomic beam apparatus. It was further simplified by the recent advent of diode lasers whose frequency can be easily varied at a high rate. However, with this method, only "bunches" of atoms interact with the laser and eventually the slowed atoms are not localized but they are spread along the beam length. In the second scheme, instead, the nonuniform magnetic field can be designed so that almost every atom will see the fixed-frequency laser in resonance starting from a position which depends on the initial velocity. If the magnetic field is properly designed, a noticeable fraction of the atoms can be slowed down with this method and brought at a given velocity at the end of the magnet. The drawback of this scheme is that a large solenoid is required, whose shape must be accurately optimized. Also the presence of an intense magnetic field can represent a limit in some experiments.

The above methods are both used in present beam-slowing experiments and the choice of one method or the other depends on the particular requirements of the experiment.

**2·1.2.** Optical molasses. The possibility of cooling an atomic gas using laser radiation was first proposed by T. W. Hänsch and A. L. Schawlow in 1975 [19]. They pointed out that if a moving atom is irradiated with counterpropagating laser beams that are tuned slightly below the atomic resonance frequency, the Doppler shift will cause the atom to absorb preferentially photons moving opposite to its velocity (fig. 2). As discussed above, the atom will slow down. In a gas, this process will produce a cooling of the gas. The kinetic energy of the atoms is dissipated and converted into energy of the electromagnetic field.

If stimulated emission of photons is neglected, using eq. (2) the force on the atoms

can be written as the sum of the forces produced by each of the laser beams:

$$F_{\mathrm{sp}}(v) = \frac{h\nu_{\mathrm{L}}}{c}\frac{1}{2\tau}\left[\frac{I/I_0}{1+(4/\Gamma^2)[\delta-(v/c)\nu_{\mathrm{L}}]^2} - \frac{I/I_0}{1+(4/\Gamma^2)[\delta+(v/c)\nu_{\mathrm{L}}]^2}\right]. \tag{3}$$

In the limit of small atomic velocity ($v < \Gamma c/2\nu_{\mathrm{L}}$), the force can be written as

$$F_{\mathrm{sp}}(v) \sim h\frac{\nu_{\mathrm{L}}^2}{c^2}\frac{8\delta}{\Gamma}\left[\frac{I/I_0}{[1+(2\delta/\Gamma)^2]^2}\right]v = -\alpha v\,. \tag{4}$$

For low velocities, the force on the atoms depends linearly on velocity as in a viscous medium. This suggested the name optical molasses for this cooling configuration. The same scheme can be extended to three dimensions using three pairs of counterpropagating laser beams in three orthogonal directions. An optical molasses was first demonstrated experimentally by S. Chu and coworkers in 1985 with sodium atoms [20].

The minimum temperature expected for the atoms in optical molasses can be estimated, with the model considered above, taking into account two effects: The first is the cooling effect produced by the viscous force. The second is a heating of the atoms due to the random direction in which photons are absorbed and emitted. The temperature of the atomic sample at which these two effects balance is

$$k_{\mathrm{B}}T = \frac{h\Gamma}{4}\left(\frac{\Gamma}{2\delta}+\frac{2\delta}{\Gamma}\right). \tag{5}$$

The minimum temperature is obtained for $\delta = -\Gamma/2$ and is given by

$$k_{\mathrm{B}}T_{\mathrm{D}} = \frac{h\Gamma}{2}. \tag{6}$$

$T_{\mathrm{D}}$ is called Doppler limit. Typical values of $T_{\mathrm{D}}$ are 240 $\mu$K for sodium and 120 $\mu$K for cesium.

An important reference temperature for laser-cooled atomic gases is the so-called recoil temperature. Because the exchange of momentum between atoms and radiation takes place by discrete amounts, corresponding to the single photon momentum, the minimum spread of the atomic energies cannot be smaller than the energy corresponding to the single photon recoil. The recoil temperature $T_{\mathrm{r}}$ is therefore defined by

$$\frac{1}{2}k_{\mathrm{B}}T_{\mathrm{r}} = \frac{1}{2m}\left(\frac{h\nu_{\mathrm{L}}}{c}\right)^2. \tag{7}$$

$T_{\mathrm{r}}$ is 2.4 $\mu$K for sodium and 197 nK for cesium.

**2·1.3.** Sub-Doppler temperatures in optical molasses. Accurate measurements of the temperature of the atoms in optical molasses, first performed by W. Phillips and coworkers by time-of-flight methods [21], showed that the temperature was much smaller than the expected Doppler limit temperature and not far from the recoil limit. This unexpected result was explained by J. Dalibard and C. Cohen-Tannoudji [22] and by S. Chu and coworkers [23]. They developed a theory of sub-Doppler laser cooling taking into account light-induced shifts of the atomic levels and optical-pumping effects.

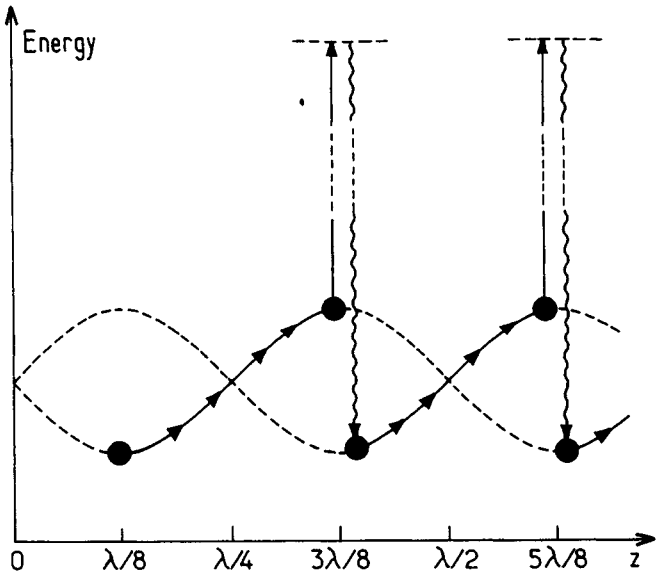


Fig. 3. – Mechanism leading to sub-Doppler cooling of atoms in 1-D optical molasses for two counterpropagating laser beams with orthogonal linear polarizations. The so-called Sisyphus cooling is an effect of the position-dependent light shift of the levels and of optical pumping.

A mechanism leading to sub-Doppler cooling can be qualitatively understood considering a 1-D model in which atoms having, for example, an angular momentum $J_g = 1/2$ in the lower state and $J_e = 3/2$ in the upper state interact with two counterpropagating laser beams with orthogonal linear polarizations. The polarization of the resulting field varies with position. Figure 3 shows the light-shifted atomic levels. The shift of a given Zeeman sublevel depends on the quantity $I/\delta$ and on the excitation probability for atoms in that level. Since this probability depends on the light polarization, the position-dependent polarization of the light leads to a position-dependent shift of the atomic levels. The combined effect of the spatially dependent light shift of the levels and of optical pumping is at the origin of the cooling mechanism. An atom starting, for example, at $z = \lambda/8$ in the $g_{-1/2}$ state and moving to the right, will climb the potential hill so that part of its kinetic energy will be converted into potential energy. If the velocity is sufficiently small, near the top of the hill the atom will be optically pumped into the $g_{+1/2}$ state. The potential energy gained at the expense of kinetic energy is dissipated in this spontaneous Raman anti-Stokes process. Optical pumping is then the mechanism allowing dissipation of energy and cooling of the atoms. This cooling effect was called Sysiphus cooling because, as in the Greek myth, the atoms are forced to continuously climb potential hills. The minimum temperature predicted by this model is of the order of the light-induced splitting of the levels. A linear dependence on $I/\delta$ is then expected.

Optical molasses are often realized with a light polarization scheme different from the one considered above. The two counterpropagating laser beams have opposite circular polarizations. Also in this case, sub-Doppler temperatures can be reached. The mechanism can be understood as follows: for two counterpropagating beams with opposite circular polarization and same amplitude, the resulting field is linearly polarized with the polarization vector rotating along the standing wave thus forming a helix with a pitch $\lambda$. It was shown in [22] that with this polarization configuration, the combined effect of the polarization rotation, light shift, and optical pumping produces a motion-induced

difference in the population of the ground-state Zeeman sublevels. This gives rise to an imbalance between the radiation pressures of the two beams and therefore to a friction force. This mechanism only works for $J \geq 1$ in the ground state.

The cooling mechanisms described above both depend on the presence of a light polarization gradient. However, since different processes lead to cooling in the two cases, different values for the friction and diffusion coefficients result. The steady-state temperatures are instead found to be about the same and to be proportional to the quantity $I/\delta$. This behaviour was confirmed experimentally for three-dimensional molasses down to temperatures of a few $\mu$K [24], corresponding to about ten times the recoil temperature.

2·1.4. Magneto-optical trapping of atoms. The magneto-optical trap (MOT) is nowadays a common method to confine and cool neutral atoms. In particular, it played a crucial role in BEC experiments. It was first proposed by J. Dalibard and demonstrated experimentally in [25].

A MOT consists of a combination of a set of laser beams and a quadrupole magnetic field. It is usually realized with six laser beams, which form three orthogonal pairs each made of two counterpropagating beams with opposite circular polarizations, intersecting in the zero point of the magnetic field generated by two parallel coils with currents flowing in opposite directions.

The basic mechanism can be understood, in the frame of a model similar to the one for Doppler cooling, by considering the 1-dimensional scheme shown in fig. 4. For simplicity, we consider an atom with a $J = 0$ ground state and a $J = 1$ excited state. The magnetic field, that is null at the center and has a magnitude proportional to the distance from the trap center, produces a position-dependent Zeeman splitting of the levels, as shown in the figure. If the laser frequency $\nu_{\mathrm{L}}$ is smaller than the atomic resonance $\nu_{\mathrm{A}}$ and the polarizations of the laser beams are chosen as indicated in the figure, atoms will experience a force towards the center of the trap. In fact, an atom displaced to one side with respect to the position where the magnetic field is null, will preferentially absorb photons from the laser beam coming from that direction and will be pushed towards the origin. As for optical molasses, the force on an atom can be written, in the low intensity limit, as the sum of the forces due to each of the beams. In this case, however, the Zeeman shift of the levels must be taken into account. In the limit of a small atomic velocity $v$ and a small Zeeman frequency shift $\kappa z$, the force can be written as

$$F_{\mathrm{sp}}(v) \sim h\frac{\nu_{\mathrm{L}}}{c}\frac{8\delta}{\Gamma}\left[\frac{I/I_0}{[1+(2\delta/\Gamma)^2]^2}\right]\left[\frac{\nu_{\mathrm{L}}}{c}v + \kappa z\right]. \tag{8}$$

The motion of an atom is therefore that of a damped harmonic oscillator. The important characteristic of the MOT is that the atoms are not only confined but their kinetic energy is also dissipated as in atomic molasses. In fact, it was found [26] that sub-Doppler mechanisms due to polarization-gradient effects also play an important role in a MOT, leading to an increase of the confining force and to temperatures below the Doppler cooling limit. Atoms can be collected in a MOT from a slowed atomic beam as in [25] or from the room temperature vapor in a cell, as first demonstrated in [27].

The rate of change in the number $N$ of trapped atoms is given by

$$\frac{\mathrm{d}N}{\mathrm{d}t} = R - \gamma N - \beta \int n^2 \mathrm{d}V\,, \tag{9}$$

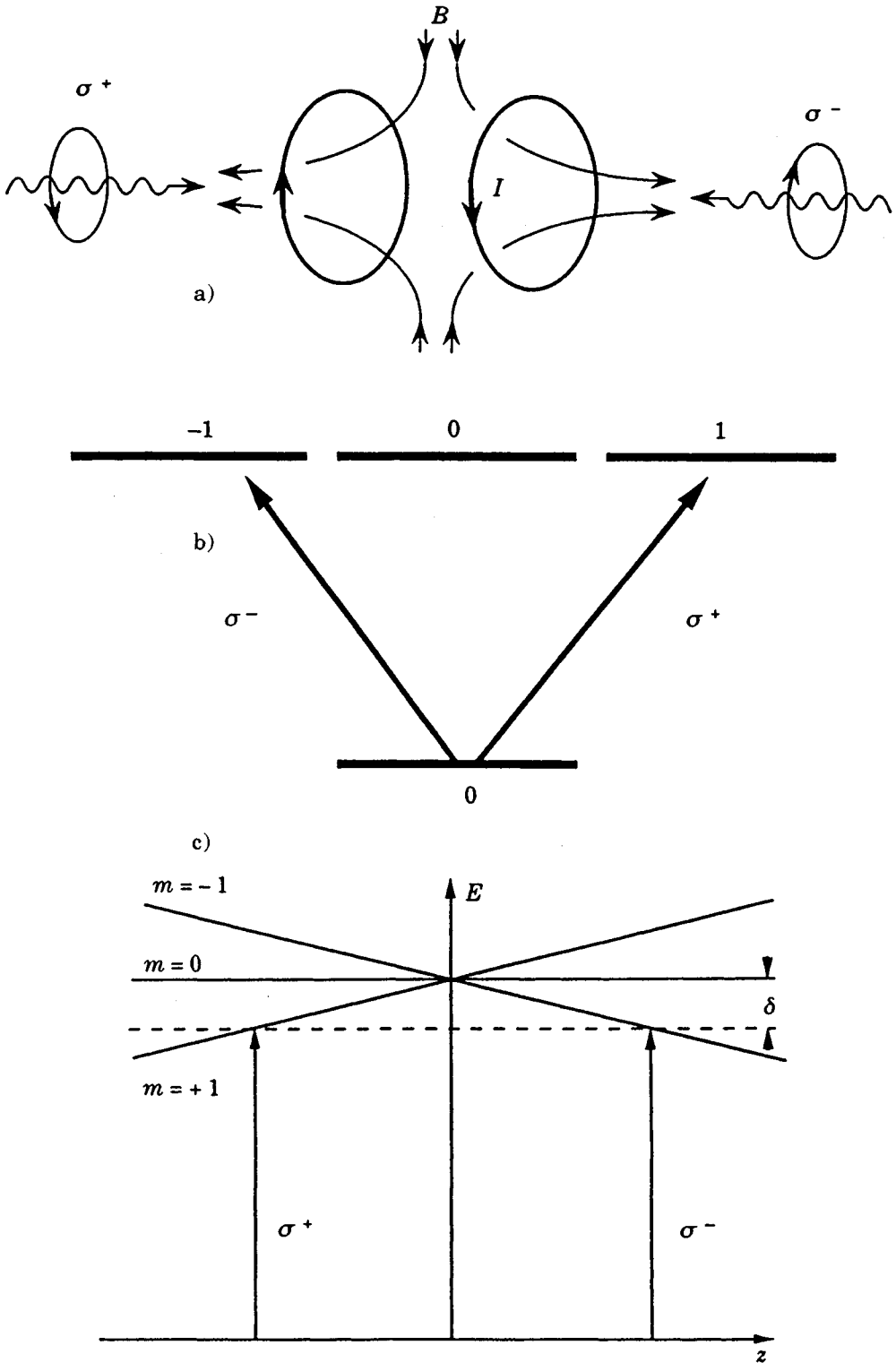


Fig. 4. – Magneto-optical trapping. a) 1-dimensional scheme of the experimental set-up for a magneto-optical trap. b) Transition scheme. c) 1-dimensional model of the MOT.

where $R$ is the collection rate, $\gamma$ is the loss rate due to collisions of the trapped atoms with background gas, and the last term gives the loss rate associated with collisions between trapped atoms with a density $n$ and loss coefficient $\beta$. In the case of a vapor-cell trap, if the last term in eq. (9) is neglected, the steady-state number of trapped atoms is $N_s = R/\gamma$. The rate $R$ at which atoms with a velocity smaller than the capture velocity of the trap $v_c$ enter the volume $V$ defined by the intersection of the laser beams is [27]

$$R = \frac{nV^{2/3}\, v_c^4}{2} \left(\frac{m}{2KT}\right)^{3/2}, \tag{10}$$

where $n$ is the density of the atoms in the vapor, $T$ is the temperature of the cell, and $m$ is the atomic mass. The capture velocity of the trap can be calculated as the maximum velocity for which an atom can be stopped within a distance equal to the laser beams diameter [28]. A rough estimate can be obtained considering a constant photon scattering rate $r = 1/2\tau_n$ where $\tau_n$ is the excited-state lifetime. The stopping distance for an atom with initial velocity $v$ is $l_{\text{stop}} = v^2/2rv_r$, where $v_r$ is the recoil velocity. By imposing that the stopping distance equals the trapping beams diameter $d$, one gets

$$v_c = \sqrt{\frac{d\, v_r}{\tau_n}}. \tag{11}$$

Equations (10) and (11) show that the loading rate $R$ is proportional to $d^4$. The loss rate $\gamma$ due to collisions of the trapped atoms with the hot atoms in the background vapor is given by $\gamma = n\sigma(3KT/m)^{1/2}$, where $\sigma$ is the collisional cross-section. The number $N$ of trapped atoms is then given by

$$N = \sqrt{\frac{1}{6}} \frac{\pi\, d^4\, v_r^2}{\tau_n^2\, \sigma} \left(\frac{m}{2KT}\right)^2. \tag{12}$$

In the case of a Cs MOT, $\tau_n = 30$ ns, $\sigma = 2 \times 10^{-13}\,\text{cm}^2$ [27], $v_r = 3.5$ mm/s; if the laser beams have a diameter of 1 cm and the MOT is loaded from a room temperature vapor, one gets $N \approx 5 \times 10^9$ atoms which is of the right order of magnitude compared to what can be obtained experimentally in these conditions.

An important quantity, especially for BEC experiments, is the density of the trapped atoms. The maximum density of atoms that can be achieved in a MOT is limited by two main factors: first, the collisions between ground-state and excited-state atoms contributing to the $\beta n^2$ loss term in eq. (9) become important at the atomic densities typically obtained in MOTs; the second limit is due to repulsive forces between trapped atoms caused by reabsorption of scattered photons. Above a critical value of density, an increase of the number of trapped atoms gives a larger cloud with no increase of density. This represents also a limiting factor for the maximum number of atoms that can be confined in a MOT. In [29], a scheme called *dark-spot* trap was demonstrated that allowed a noticeable increase in the density of trapped atoms. The key idea is to isolate the cold atoms from the trapping light. This is obtained by optically pumping the atoms in the center of the trap into a state where they do not interact with the trapping laser. This scheme allows an increase of both the number of trapped atoms and their density. More than $10^{10}$ atoms can be confined in a dark-spot trap at densities of about $10^{12}\,\text{atoms/cm}^3$.

The maximum phase-space density obtained with the methods of laser cooling and trapping described above is in the range $10^{-5}$–$10^{-4}$.

2'1.5. Other schemes for laser cooling and trapping of atoms. In the effort towards the achievement of BEC in atomic gases, several methods have been developed to increase the phase-space density in a sample of atoms. Here, we only focus on the methods that were used in the experiments in which condensation was observed so far. In these experiments, a combination of optical cooling and trapping methods and of other techniques based on magnetic trapping and evaporative cooling was used. However, the possibility of reaching quantum degeneracy conditions with purely optical schemes cannot be excluded. Amongst the methods which look more promising in this prospect, are trapping by optical dipole traps and subrecoil cooling schemes such as Raman cooling and velocity-selective coherent population trapping.

The dipole trap is an optical trap based on the dipole force acting on an atom in the presence of nearly resonant light with a nonuniform intensity. This force is not caused by the scattering of photons due to spontaneous emission but can be considered as the effect of processes of absorption-stimulated emission of photons. In the dressed-atom picture, the dipole force arises from the spatially varying shift of atomic levels produced by a light field with a nonuniform intensity profile. For a laser frequency smaller than the atomic resonance frequency, the atoms will be attracted towards high-intensity regions. In contrast, for a positive detuning the atoms will be repelled from the high-intensity regions. A dipole trap was first realized in [30] using a single, red-detuned, focused laser beam. At the focus, the intensity has an absolute maximum such that three-dimensional confinement is possible.

Since no cooling mechanism is present in this trap, only atoms colder than the trap depth can be loaded into it. Also, the lifetime of the atoms in the trap is limited by the heating due to absorption and spontaneous emission of photons. The heating rate can be reduced by using large values of detuning for the trapping beam. Indeed, the photon scattering rate is proportional to $I/\delta^2$ while, for a large detuning, the trap depth depends on $I/\delta$. With the so-called far-off-resonance trap (FORT), trap depths of the order of mK can be obtained with lifetimes of several seconds [31]. Recently, a hybrid electro-optical dipole trap was demonstrated [32]; a static electric field was used to increase the confinement along the axial direction of the focused laser beam, that is a weak-confinement direction in the single-beam dipole trap. Blue-detuned dipole traps are also interesting and have been demonstrated [33]. In these traps, atoms can be confined by the repulsive walls created with the blue-detuned light and kept in regions where light is virtually absent.

Optical dipole traps have several positive features: they allow confinement of atoms at very high densities and in extremely small volumes. Contrary to the case of magnetic traps, the atoms in a dipole trap are not polarized. This can be of particular importance in experiments where mixed-spin systems are studied. Light traps can be quickly switched on and off. They can allow the confinement of atoms for which magnetic traps cannot be used. The main drawbacks of these traps are the high intensity required in order to use large values of detuning, and the need for good spatial stability of the trapping laser beam.

Of particular interest is the possibility of combining trapping in optical dipole traps and subrecoil cooling methods. Two cooling methods have been demonstrated leading to atomic samples where the velocity spread is smaller than the atom's recoil velocity after emission of a photon: velocity-selective coherent population trapping (VSCPT) [34-36]

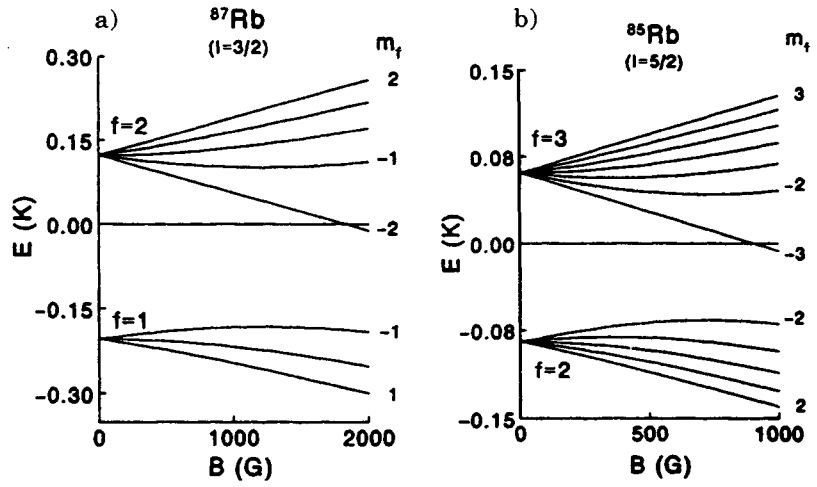


Fig. 5. – Energy of the Zeeman components of the hyperfine levels in the ground state of $^{87}$Rb and $^{85}$Rb as a function of the magnetic field.

and Raman cooling [37-40]. These cooling methods are both based on the idea of letting the atoms randomly scatter photons until they fall by spontaneous emission into a velocity-selective state which is no longer coupled to the laser field. In VSCPT, a c.w. light field tuned to a $J_g = 1 \rightarrow J_e = 1$ transition produces a velocity-selective dark state. This state is a linear superposition of magnetic substates having different linear momenta. In Raman cooling, on the other hand, the light field is pulsed. Atoms are pushed towards $v = 0$ with a sequence of laser pulses which induce velocity-selective Raman transitions followed by resonant excitation and spontaneous emission. Appropriate choice of laser pulse shape and detuning prevents atoms with $v \sim 0$ from being further excited. While VSCPT requires a specific type of atomic transition, Raman cooling can be applied to any three-level system with two long-lived states.

Raman cooling of atoms in a dipole trap was demonstrated in [41]. Sodium atoms were cooled down to a temperature of about 1 $\mu$K with a density of $4 \times 10^{11}$ atoms/cm$^3$, corresponding to a factor $\sim 400$ in phase space density from BEC.

2·2. *Magnetic trapping.* – Magnetic traps consist of an inhomogeneous magnetic field with a local minimum. Atoms with a non-zero magnetic moment $\boldsymbol{\mu}$ in an inhomogeneous magnetic field $\mathbf{B}$ have an interaction energy given by $W = -\boldsymbol{\mu} \cdot \mathbf{B}$ and experience a force $\mathbf{F} = \nabla(\boldsymbol{\mu} \cdot \mathbf{B})$. The direction of the force depends on the orientation of the magnetic moment with respect to the field. If the atomic motion is adiabatic (the atom does not change Zeeman sublevel), it can be described by a local potential given by the atomic magnetic moment times $\mid \mathbf{B} \mid$. In the presence of a minimum of the magnetic field $\mid \mathbf{B} \mid$, atoms which are in a state whose energy increases with increasing magnetic field experience a restoring force towards the minimum region and can be trapped. Since for a static magnetic field only minima can exist in free space [42], only atoms in low-field-seeking states can be trapped. Figure 5 shows the energy of the Zeeman components of the ground state of $^{87}$Rb and $^{85}$Rb atoms as a function of the magnetic field. Magnetostatic traps work for $^{87}$Rb atoms in $\mid F = 1, m = -1\rangle$ and $\mid F = 2, m = 1, 2\rangle$ states and for $^{85}$Rb atoms in $\mid F = 2, m = -1, -2\rangle$ and $\mid F = 3, m = 1, 2, 3\rangle$ states.

A magnetic trap was first used by W. Paul to confine neutrons [43]. Magnetic trapping of neutral atoms was first demonstrated for Na [44]. More recently, magnetic traps were

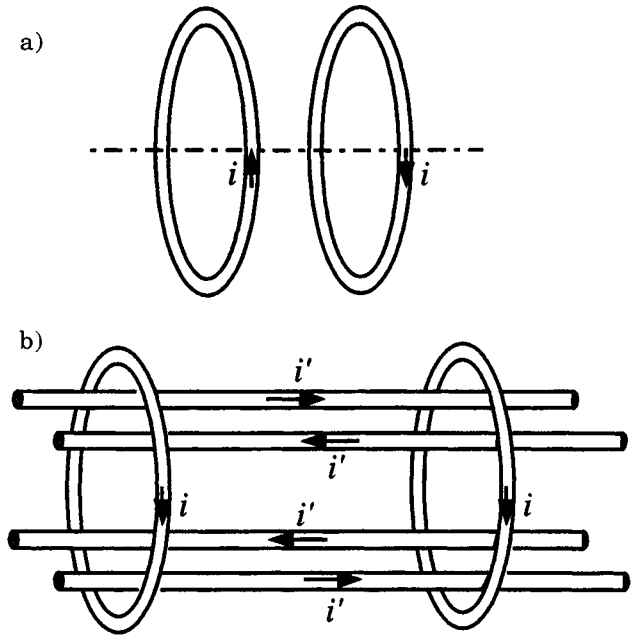


Fig. 6. – (a) Scheme of a quadrupole trap. (b) Scheme of a Ioffe-Pritchard trap.

used to confine H [45,46], Li [11], Na [47,48], K [49], Rb [50,51], Cs [27,52], and Eu [53].

Compared to magneto-optical traps, magnetic traps allow the confinement of the atoms at much lower temperatures because the effects due to radiation are absent (for example, the photon recoil limit). Magnetic traps are, however, much shallower than MOTs. The typical depth can be estimated considering a magnetic trap made of two parallel coils with currents flowing in opposite directions. As discussed in the following, such a configuration produces a field which is zero at the trap center and increases linearly around it. For a system of $\sim 2$ cm radius coils separated by $\sim 3$ cm carrying a current of $\sim 500$ At, the axial field gradient at the trap center is of the order of 100 G/cm and the lowest threshold is $\Delta B \sim 100$ G. Since the magnetic moment of a ground-state alkali atom is $\mu \approx \mu_{\mathrm{B}}$, atoms can be trapped only if $k_{\mathrm{B}}T < \mu_{\mathrm{B}}\Delta B \approx 10^{-25}$ J, corresponding to a temperature of about 10 mK. Compared with atoms emerging from a thermal beam or a vapor at 300 K, it is clear that atoms must be pre-cooled before being loaded into a magnetic trap.

It must be noted that since magnetic traps are conservative traps, an independent mechanism is required to cool the atoms once they are in the trap. The methods demonstrated so far are evaporative cooling, which is described in detail in the next section, and sympathetic cooling via elastic collisions with another cold species in the trap (see sect. **3**·6).

**2**·2.1. Quadrupole traps. The simplest scheme to realize a magnetic trap is the anti-Helmholtz configuration schematically shown in fig. 6a. This configuration produces a spherical-quadrupole magnetic field crossing a zero at the center and varying linearly around it. For two coils with radius $R$ separated by a distance $A$ and a current $I$ flowing, the field components in cylindrical coordinates are [54]

$$B_z = 2cz, \quad B_\rho = -c\rho, \quad B_\phi = 0, \tag{13}$$

where $c = 3\mu_0 IAR^2/2(A^2 + R^2)^{5/2}$.

The potential energy for an atom in the trap is given by

$$W = \mu \mid \mathbf{B} \mid = \mu c\sqrt{4z^2 + \rho^2}\,. \tag{14}$$

This type of trap was used in the initial experiments of atom trapping. In addition to the simplicity of the construction, it offers the advantage of a tight confinement of the atoms compared to other traps, discussed in the following, which are characterized by a parabolic minimum around a finite bias field.

A serious drawback of this trap becomes apparent, however, when it is used in combination with evaporative cooling. As the temperature of the atoms is lowered and their density increases, a loss of atoms from the trap is observed. This loss mechanism is due to the so-called Majorana spin-flips.

**2·2.2.** Losses due to Majorana spin-flips. As the atoms move in a magnetic trap, they experience a magnetic field changing direction in a complicated way. In order for the atoms to be trapped, the atomic magnetic moments must be oriented so that they are attracted towards the field minimum region. If the magnetic field changes slowly, the atomic magnetic moment precesses around the field and follows it adiabatically. The adiabaticity condition is violated if the Larmor frequency is smaller than the rate of change of the field direction. This is in fact the case for atoms passing close to the zero-field point in the center of a quadrupole trap. The probability of nonadiabatic transitions for a beam of oriented atoms crossing a region where the magnetic field goes to zero was calculated by E. Majorana [55]. Atoms in a quadrupole trap can undergo a spin-flip transition from one Zeeman sublevel to another and be lost from the trap [56]. The loss rate $1/\tau_0$ caused by this effect can be estimated as follows [50]. If an atom with velocity $v$ and mass $m$ passes near the center of the trap with a minimum distance $b$, it can undergo a nonadiabatic spin-flip if the Larmor frequency is smaller than the rate of change of the magnetic field direction $v/b$. For a radial gradient of the field $\partial B_r/\partial r = B'_q$, the Larmor frequency is $\sim \mu b B'_q/\hbar$. Loss then occurs within an ellipsoid of radius $b_0 \sim (v\hbar/\mu B'_q)^{1/2}$. The loss rate is given by the flux through this ellipsoid, that is, the density of atoms $N/l^3$ times the area of the ellipsoid $\sim b_0^2$ times the velocity $v$, where $N$ is the number of trapped atoms and $l$ is the radius of the atom cloud. The mean velocity and cloud size are related by the virial theorem: $mv^2 \sim \mu l B'_q$. It follows that $\tau_0 \sim (m/\hbar)l^2$. For $^{87}$Rb atoms, for example, $m/\hbar$ is about $10^5\,\mathrm{s/cm^2}$. The loss rate increases as the atoms are cooled and spend more time at the bottom of the trap near the zero-field point. In order to reduce losses due to spin-flips, different schemes were invented that prevent the atoms from crossing a zero-field region. They are briefly described in the following.

**2·2.3.** The time-averaged orbiting potential (TOP) trap. In the first experiment in which Bose-Einstein condensation was observed [8], a magnetic trap, named TOP trap, was used which had been invented trying to overcome the storage time limitation due to spin-flip losses while keeping the advantage of tight confinement of a quadrupole trap [50].

The idea of the TOP trap is to add to the quadrupole magnetic field a continuously changing bias field that moves the location of the field zero around much faster than the atoms can follow. In ref. [50] this was realized by adding to the static quadrupole field, produced by two horizontal coils in anti-Helmholtz configuration, a small magnetic field $B_{\mathrm{TOP}} \sim 10$ G, rotating in the horizontal plane with a frequency $\omega_{\mathrm{TOP}}$ of the order of

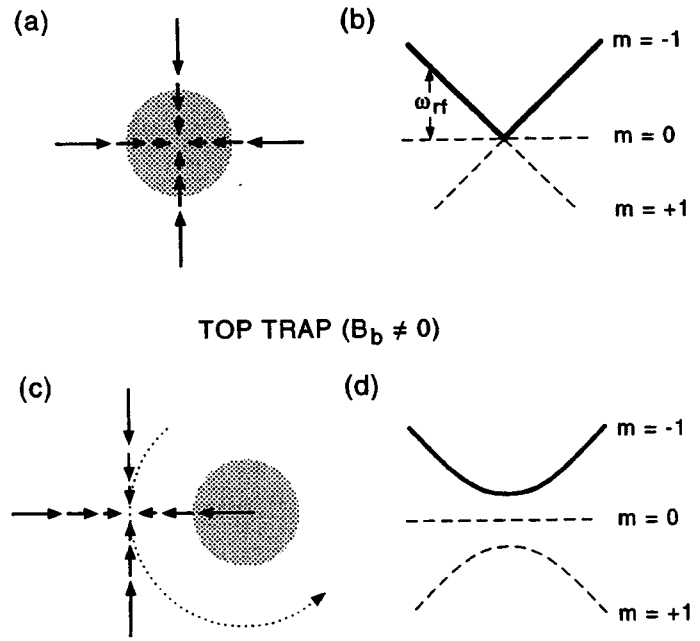


Fig. 7. – Comparison of magnetic-field configuration and resulting potential for a quadrupole trap (a, b) and for a time-averaged orbiting potential (TOP) trap (c, d). (From W. Petrich *et al.* (1995), with permission.)

10 kHz (fig. 7). The value of $\omega_{\mathrm{TOP}}$ must be much smaller than the Larmor frequency for atoms in the bias field and much larger than the oscillation frequency of the atoms in the trap:

$$\omega_{\mathrm{L}} \propto B_{\mathrm{TOP}} \gg \omega_{\mathrm{TOP}} \gg \omega_{\mathrm{vib}} . \tag{15}$$

The motion of the atoms is then governed by the time average of the instantaneous potential. It can be shown [50] that, using cylindrical coordinates with $z$ indicating the axis of the quadrupole trap, the resulting potential energy has the form

$$W_{\mathrm{TOP}}(\rho, z) \simeq \mu B_{\mathrm{TOP}} + \frac{\mu B_q'^2}{4B_{\mathrm{TOP}}}(\rho^2 + 8z^2) . \tag{16}$$

The trap is therefore harmonic to lowest order and the magnetic field in the center of the trap is $B_{\mathrm{TOP}} \neq 0$.

2·2.4. The optical-plug trap. Another successful method to "plug the hole" leading to losses in quadrupole traps makes use of the optical dipole force to repel the atoms from the central region of the trap. This method was used in the first experiment in which Bose-Einstein condensation was observed in a gas of sodium atoms [9]. The optical plug was created by an $Ar^+$ laser beam tightly focused at the point of zero magnetic field. The blue-detuned far-off-resonance light produced a light-shift repulsive barrier that prevented the atoms from crossing the zero-field region in the trap. As for the other trapping schemes, the atoms were cooled by rf-induced evaporation. The potential experienced by the atoms is then a combination of the magnetic trapping potential, the repulsive potential due to the laser beam and the effect due to the rf. The resulting potential is shown in fig. 8.

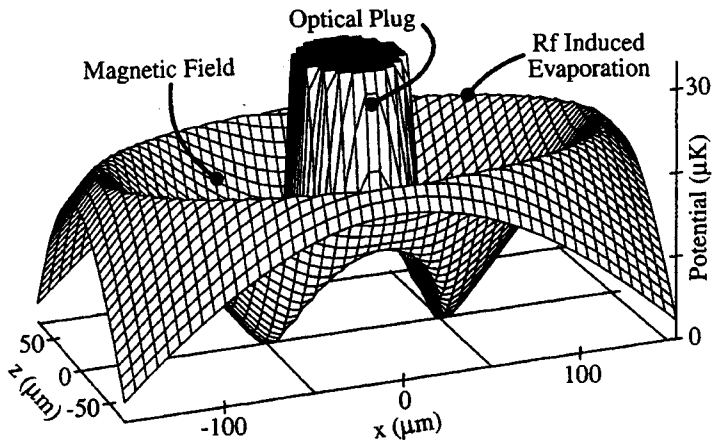


Fig. 8. – Adiabatic potential for an optical-plug trap. The total potential is a combination of the magnetic quadrupole trapping potential, the repulsive potential of the laser plug, and the energy shifts due to the rf. (From K. B. Davis *et al.* (1995), with permission.)

2·2.5. The Ioffe-Pritchard–type traps. The trap called Ioffe-Pritchard (IP) trap was one of the first schemes to be suggested for trapping atoms [57]. It is similar to the Ioffe configuration introduced earlier for plasma confinement [58]. The basic scheme of this trap is shown in fig. 6b. It is made of two coils with parallel current, producing a so-called bottle field, and four straight conductors with current in alternating directions producing a quadrupole field for transverse confinement. If we use cylindrical coordinates with $z$ indicating the axial direction, in proximity of the center the field components are [54]

$$\begin{aligned} B_z &= c_1 + c_3(z^2 - \rho^2/2) + \dots , \\ B_\rho &= -c_3 z\rho + c_2\rho\cos(2\phi) + \dots , \\ B_\phi &= -c_2\rho\sin(2\phi) + \dots , \end{aligned} \tag{17}$$

where $c_1$, $c_2$ and $c_3$ are coefficients which can be calculated using the expressions for the field produced by a coil and by a straight conductor.

The resulting field $|\,\mathbf{B}\,|$ is given by

$$|\,\mathbf{B}\,|^2 = c_1^2 + 2c_1c_3z^2 + [c_2^2 - c_1c_3 - 2c_2c_3z\cos(2\phi)]\rho^2 + c_3^2(z^4 + \rho^4/4) + \dots \tag{18}$$

With proper choice of the configuration, the origin can be made a minimum for motion in any direction. The resulting potential is harmonic with a nonzero bias field at the origin:

$$W = \mu\left[c_1 + c_3z^2 + \frac{1}{2}\left(\frac{c_2^2}{c_1} - c_3\right)\rho^2\right] . \tag{19}$$

In this case, an atom passing near the center of the trap never finds a vanishing field and spin-flips can be suppressed. For this purpose, the Larmor frequency for atoms in the bias field must be larger than the vibrational frequency of the atoms in the trap:

$$\omega_{\mathrm{L}} \propto B_{\mathrm{IP}} \gg \omega_{\mathrm{vib}} , \tag{20}$$

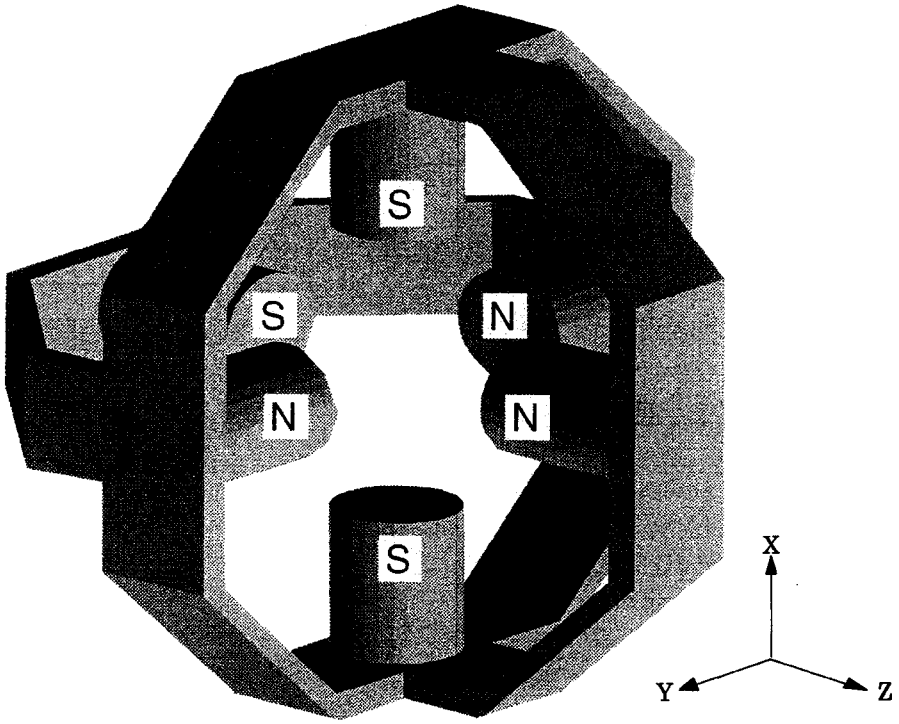


Fig. 9. – Magnetic trap made of six permanent magnet cylinders. (Figure courtesy of R. Hulet.)

where $B_{\mathrm{IP}}$ is the bias field at the center of the trap (given by the $c_1$ term in eq. (17)). A bias field $B_{\mathrm{IP}}$ of a few Gauss is typically sufficient.

In fact, in recent experiments of BEC, trap schemes that can be considered as variants of an IP trap were used. One is called "baseball" trap because it is made of coils following the pattern of the seams on a baseball [51]. Another scheme is called "cloverleaf" trap, again because of the shape of the coils [48]. These schemes will not be described in detail here for brevity.

**2·2.6.** Permanent-magnets traps. Intense fields and tight field curvatures can be easily obtained using permanent magnets. A trap made of permanent magnets was used in the experiment of BEC of $^7$Li [10, 11] (fig. 9). In this experiment, the trap oscillation frequencies were of the order of 150 Hz with a bias field of about 0.1 T. As discussed in subsect. **2·3**, a large value of the field curvature, that is of oscillation frequency, makes evaporative cooling more efficient. On the other hand, permanent magnets have the disadvantage that the magnetic fields cannot be changed. This can be a serious limitation, for example, for the observation of the condensate.

**2·2.7.** Comparison of magnetic traps. Several factors must be taken into account for a comparison of the different schemes of magnetic traps for atoms. In experiments aiming to achieve BEC by evaporative cooling, it is important to reach the highest collisional rate after the atoms have been compressed in the magnetic trap while keeping the Majorana spin-flips to a negligible level. Important issues are also the simplicity of construction and the possibility of optical access. This latter considerations limited the use of traps made of superconducting magnets to hydrogen experiments where cryogenic systems are used.

If the geometric mean of the field curvatures is considered as a relevant figure of merit, a quantitative comparison can be made of TOP and IP traps [8,48]. The magnetic field gradient $B'$ and curvature $B''$ produced by a coil of radius $R_c$ at a distance $\sim R_c$ are

$$(B')_z \simeq \frac{B_0}{R_c}, \qquad (B'')_z \simeq \frac{B_0}{R_c^2} \simeq \frac{B'}{R_c} \simeq \frac{B'^2}{B_0}, \tag{21}$$

where $B_0$ is the field at the center of the coil. This gives a good estimate of the axial curvature in the IP trap. From eq. (18) it can be seen that the curvature of the radial field is given by

$$(B'')_{x,y} \simeq \frac{B'^2}{B_{\mathrm{IP}}}, \tag{22}$$

where $B_{\mathrm{IP}}$ is the bias field at the center of the trap.

For the TOP trap, eq. (16) gives a curvature

$$(B'')_{\mathrm{TOP}} \simeq \frac{B'^2}{B_{\mathrm{TOP}}}. \tag{23}$$

The quantities to be compared are therefore

$$(B''_x B''_y B''_z)_{\mathrm{IP}} \simeq \frac{B'^6}{B_0 B_{\mathrm{IP}}^2}, \qquad (B''_x B''_y B''_z)_{\mathrm{TOP}} \simeq \frac{B'^6}{B_{\mathrm{TOP}}^3}. \tag{24}$$

Equations (15) and (20) indicate that in order to avoid spin-flips, the minimum $B_{\mathrm{TOP}}$ of a TOP trap must be much larger than $B_{\mathrm{IP}}$ of an IP trap. Therefore for comparable field gradient $B'$, the radial curvature of the TOP trap is smaller than that of an IP trap (typically by two orders of magnitude). In the axial direction, instead, the curvature of the TOP trap is typically hundred times larger than that of an IP trap. The geometric mean of the curvatures is then usually better in an IP trap than in a TOP trap.

**2·3.** *Evaporative cooling of trapped atoms.* – Evaporative cooling of a gas of trapped atoms is based on the selective removal of atoms which have an energy higher than the average energy per atom and on rethermalization of the sample by collisions. Since the average energy of the atoms remaining in the trap is reduced in this process, the new equilibrium state of the gas corresponds to a lower temperature. As described in the following, methods have been demonstrated to force the cooling to proceed at a given rate. With optimized evaporative procedures, it is possible to achieve a dramatic reduction of the gas temperature and, more important for BEC experiments, an increase of the phase-space density by 5-6 orders of magnitude.

Evaporative cooling was first proposed [59] and demonstrated [60] in the effort to achieve BEC of atomic hydrogen. The technique was later extended to alkali atoms [50, 47] and, in combination with laser cooling, played a key role in the recent experiments on BEC.

Different methods of evaporative cooling have been demonstrated [61]. In the experiments on alkali atoms in which BEC was observed so far, rf-induced evaporation was used. An rf field was used to induce spin-flip transitions from trapped to untrapped states. The resonance frequency depends on the local magnetic field. Excitation can then

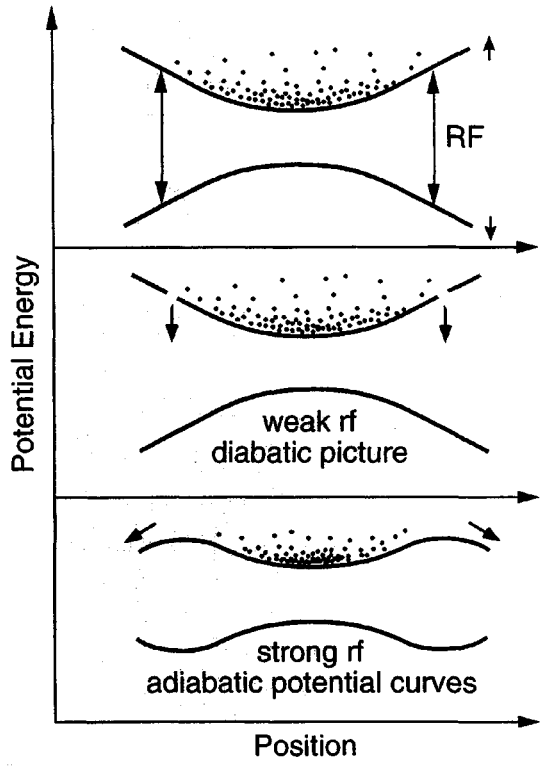


Fig. 10. – Rf-induced evaporative cooling. (Figure courtesy of W. Ketterle.)

be energy-selective taking advantage of the connection between position and potential energy for the atoms in the trap (fig. 10).

In this subsection, we discuss some general features of the process and give the general scaling laws and the relevant parameters following essentially the presentation in [61]. Several detailed studies of evaporative cooling of trapped atoms have been published. An accurate overview on the subject can be found in [61,62].

We consider a sample initially made of $N$ trapped atoms at a temperature $T$. The atoms are confined by a three-dimensional potential $U(r) \propto r^{3/\delta}$. Cases of particular interest for the present discussion are the linear potential ($\delta = 3$) and the parabolic potential ($\delta = 3/2$)([1]). The average energy per atom is given by

$$E = \left(\frac{3}{2} + \delta\right) k_{\mathrm{B}} T . \tag{25}$$

As mentioned above, evaporative cooling works by "cutting the edge" of the confining potential so that high-energy atoms can escape. We indicate the depth of the resulting potential with $\epsilon_t = \eta k_{\mathrm{B}} T$ and the average energy of the removed atoms with $(\eta + k) k_{\mathrm{B}} T$. If $\mathrm{d}N$ atoms escape from the trap, the energy of the $N' = N - \mathrm{d}N$ atoms remaining in

([1]) For an anisotropic potential, $U(x,y,z) = a \mid x \mid^{1/\delta_1} + b \mid y \mid^{1/\delta_2} + c \mid z \mid^{1/\delta_3}$ with $\delta = \delta_1 + \delta_2 + \delta_3$.

the sample is reduced by

$$dE = dN\left[(\eta + k) - \left(\frac{3}{2} + \delta\right)\right] k_B T . \tag{26}$$

Rethermalization by collisions leads to a new temperature $T' = T - dT$, given by the condition

$$N'\left(\frac{3}{2} + \delta\right) k_B T - dE = N'\left(\frac{3}{2} + \delta\right) k_B T' . \tag{27}$$

From eqs. (26),(27), neglecting second-order terms in $dN\, dT$, it follows that

$$\frac{dT}{T} = \alpha \frac{dN}{N} , \tag{28}$$

where

$$\alpha = \frac{\eta + k}{\frac{3}{2} + \delta} - 1 . \tag{29}$$

$\alpha$ is a crucial parameter in the evaporative cooling process, giving the temperature change per particle lost. In particular, if $\alpha$ is kept constant during the process, eq. (28) is easily integrated and gives

$$\frac{T_1}{T_2} = \left(\frac{N_1}{N_2}\right)^{\alpha} . \tag{30}$$

Note that $\eta \gg 1 \longrightarrow \alpha \gg 1$; eq. (30) shows then how efficient evaporative cooling can be. Equation (30) also shows that in the evaporation process $T$ is no longer independent of $N$. The scaling laws for the relevant physical quantities can then be expressed in terms of the number of atoms in the sample, by taking the dependence on $N$ and $T$ of these quantities for atoms in equilibrium in a confining potential and replacing $T$ by $N^{\alpha}$. The results are shown in table I. From the scaling laws in the table, it is possible to determine for which values of $\alpha$, and consequently of $\eta$, evaporative cooling works efficiently. A first consideration is that in order to have an increase of the phase-space density $D$ when the number of atoms in the trap is reduced, the exponent of $N$ in the expression of $D$ must be negative, that is

$$\alpha > \frac{1}{\delta + \frac{3}{2}} . \tag{31}$$

Another condition to be fulfilled is that the evaporation does not lead to a reduction of the collisional rate $n\sigma_{el}v$, which would slow down the process. The reduction of $v$ must be compensated by an increase of the density $n$. Table I shows that this is the case if

$$\alpha > \frac{1}{\delta - \frac{1}{2}} . \tag{32}$$

This regime is called "runaway evaporation". Conditions (31) and (32) indicate that efficient evaporation requires a value of $\eta$ as large as possible. This is in agreement

TABLE I. – *Dependence of relevant physical parameters on the number of trapped atoms $N$ during evaporation.*

| | |
|---|---|
| Temperature, $T$ | $\propto N^{\alpha}$ |
| Volume, $V$ | $\propto N^{\alpha\delta}$ |
| Density, $n$ | $\propto N^{(1-\alpha\delta)}$ |
| Average velocity, $v$ | $\propto N^{\alpha/2}$ |
| Elastic collision rate, $n\sigma v$ | $\propto N^{[1-\alpha(\delta-\frac{1}{2})]}$ |
| Phase space density, $D$ | $\propto N^{[1-\alpha(\delta+\frac{3}{2})]}$ |

with the intuitive argument that the larger the energy of the evaporating particles, the larger the temperature change. On the other hand, a large value of $\eta$ implies a low rate of evaporation. If the evaporation time is too long, other mechanisms such as collisions or Majorana spin-flips can produce losses of atoms from the trap. Optimization of the evaporative cooling then requires a compromise between efficiency and speed of the evaporation process taking into account the unavoidable loss mechanisms. It is beyond the scope of this review to analyze this problem in detail. An analytical expression for the rate of evaporation can be easily obtained, however, following an argument given in [61]. This rate can then be compared with the rate of losses of atoms from the trap. The argument is the following: For a large value of $\eta$, the rate of evaporation of the atoms is the same as the rate of production of atoms with energy larger than $\eta k_{\mathrm{B}}T$. The evaporation rate can be written as the number of atoms with energy higher than $\eta k_{\mathrm{B}}T$ times the elastic collision rate $1/\tau_{\mathrm{el}}$. The number of atoms with $E > \eta k_{\mathrm{B}}T$ in the untruncated Boltzmann distribution can be approximated with $2N\sqrt{\eta/\pi}\exp[-\eta]$. The elastic collision rate is given by $n_0\sigma v$, where $n_0$ is the density of the particles, $\sigma$ is the elastic collision cross-section, and $v = \sqrt{2\eta k_{\mathrm{B}}T/m} = \sqrt{\pi\eta}\bar{v}/2$ is the velocity of atoms with energy $\eta k_{\mathrm{B}}T$. The rate of evaporation can therefore be written as

$$\dot{N} = -Nn_0\sigma\bar{v}\eta e^{-\eta} = -\frac{N}{\tau_{\mathrm{ev}}}. \tag{33}$$

Equation (33) gives the rate of change of the number of atoms due to evaporation. The loss of atoms due to background gas collisions or other loss mechanisms can be taken into account by considering an exponential decay of the number of atoms with a time constant $\tau_{\mathrm{loss}}$. The rate of change of the collisional rate can then be written as

$$\frac{1}{n\sigma v}\frac{\mathrm{d}}{\mathrm{d}t}(n\sigma v) = -\left[\frac{1-\alpha(\delta-\frac{1}{2})}{\tau_{\mathrm{ev}}} + \frac{1}{\tau_{\mathrm{loss}}}\right]. \tag{34}$$

In order to have a constant or increasing collisional rate during evaporation, the term in the square bracket must be null or negative, that is

$$\frac{\tau_{\mathrm{ev}}}{\tau_{\mathrm{loss}}} \leq \alpha\left(\delta-\frac{1}{2}\right)-1 \rightarrow \frac{\tau_{\mathrm{loss}}}{\tau_{\mathrm{el}}} \geq \frac{\tau_{\mathrm{ev}}}{\tau_{\mathrm{el}}}\frac{1}{\alpha\left(\delta-\frac{1}{2}\right)-1}. \tag{35}$$

The quantity $\tau_{\mathrm{ev}}/\tau_{\mathrm{el}}$ can be easily calculated in the limit of large $\eta$ considered above,

giving

$$\frac{\tau_{ev}}{\tau_{el}} \approx \frac{\sqrt{2}e^{\eta}}{\eta}. \tag{36}$$

For arbitrary values of $\eta$, this ratio can be written in terms of generalized gamma functions.

Equation (35) shows that efficient evaporative cooling requires the rate of elastic collisions to be much larger than the rate of collisions causing losses of atoms from the trap (typical numbers in the experiments are $\tau_{loss} \approx 200 - 500$ times $\tau_{el}$).

Two kinds of collisions are responsible for atom losses from magnetic traps: collisions with background gas and inelastic collisions. Losses due to background gas collisions can be reduced by reducing the pressure of background gas. Ultra-high vacuum chambers are indeed used in the experiments. Inelastic collisional processes can be either binary collisions, such as dipole relaxation and spin relaxation, or three-body recombination. Since evaporative cooling is based on collisions, a high density is required; inelastic collisions are then unavoidable. The situation is however quite different for different atoms depending on their collisional parameters. The success of BEC experiments on alkali atoms, compared with the experiments on hydrogen, is due to the fact that alkali atoms have a much larger elastic cross-section. Since the rate of inelastic collisions is roughly the same as in hydrogen, the ratio of "good" to "bad" collisions is much larger for alkali atoms. An analysis of the relevance of different kinds of collisions for different atoms is beyond the scope of this review. A comprehensive treatment of the subject can be found in [61] and references therein.

## 3. – Studies of Bose-Einstein condensates

**3·1.** *Experimental procedure to achieve BEC.* – In the previous section, the ingredients of BEC experiments were presented, that is the methods to cool and trap the atoms. Here, we describe the way these ingredients were put together in the first experiments in which BEC was observed. Table II gives a synthetic view of the general scheme of a BEC experiment with the possible variations demonstrated in the different laboratories. The procedure to observe BEC can in fact be divided into four main steps.

The first step is laser cooling and trapping of the atoms. This was accomplished by using a single vapor-cell MOT, or a laser-slowed atomic beam, or a double-MOT apparatus in which the atoms are loaded in a first MOT from the vapor and then transferred into a second, high-vacuum, chamber. In the first experiments, a dark-spot MOT was used to increase the atoms density. A molasses phase can be used to reduce the temperature of the atoms before loading them into the magnetic trap. In this first step a large gain in phase-space density is obtained. For example, the phase-space density in a room temperature vapor of Rb at a pressure of $10^{-10}$ Torr is of the order of $10^{-20}$. After laser cooling and confinement, a value in the range $10^{-6}$–$10^{-5}$ can be reached.

The second step is the magnetic trapping of the atoms: This is the aspect in which the different experiments have more differentiated. As described in subsect. **2·2**, several schemes have been developed to achieve a tight confinement of the atoms and to avoid losses due to Majorana spin-flips. The trap configuration must also be suitable for evaporative cooling of the atoms in the trap. An important stage in this phase is the adiabatic compression of the trapped atoms. After loading, the atoms in the trap are adiabatically compressed by increasing the trap curvature. This leads to an increase

TABLE II. – *Experimental procedures used to study Bose-Einstein condensation in atomic gases.*

| | |
|---|---|
| 1) Laser cooling and trapping | Single vapor-cell (JILA) [8]<br>Slowed atomic beam (MIT, Rice) [9,48,11]<br>Double-MOT (JILA) [51] |
| 2) Magnetic trapping | TOP (JILA) [8]<br>Optical plug (MIT) [9]<br>Permanent magnets (Rice) [11]<br>Cloverleaf (MIT) [48]<br>Baseball (JILA) [51] |
| 3) rf-induced evaporative cooling | (JILA, MIT, Rice) |
| 4) Optical imaging | Absorption imaging (JILA, MIT) [8,9,48,51]<br>Dark-ground imaging (MIT) [63]<br>Polarization imaging (Rice) [11] |

of the temperature and density of the atoms, with the phase-space density remaining constant. The increased rate of elastic collisions obtained in this way is important to achieve the necessary conditions of rethermalization in the evaporative cooling process.

The third important stage is indeed evaporative cooling. In all of the experiments where BEC was obtained so far, atoms in the magnetic trap were cooled with evaporative cooling by using rf-induced evaporation. As mentioned in subsect. **2**˙3, the magnetically trapped atoms are irradiated with rf radiation. The rf frequency is tuned near the resonance frequency for transitions between nearby Zeeman sublevels. This produces spin-flip transitions from trapped to untrapped states. Since higher-energy atoms can reach higher-field regions of the trap, spin-flip resonance frequencies are more shifted than for colder atoms. By varying the frequency of the rf field, colder and colder atoms are eliminated from the trap. As discussed in subsect. **2**˙3, if the right procedure is followed, this process can give an increase of the phase-space density of several orders of magnitude and eventually allows to reach the condition for BEC (phase-space density $\sim$ 1).

Once conditions for BEC have been reached, a proper observation method must be used. For this fourth stage, the methods demonstrated so far are based on absorption imaging and phase-contrast imaging. The basic idea and experimental realization of these detection methods are described in the next subsection.

In order to give a specific example of an experimental procedure to reach BEC, we can describe the way followed in the first, now almost "historical", realization at JILA [8]. About $10^7$ $^{87}$Rb atoms were first collected in a dark-spot MOT from the room temperature vapor in a glass cell. Because of the very low pressure of Rb in the cell ($10^{-11}$ Torr), the loading of the MOT took about 300 s. The trapped atoms were compressed and cooled to 20 $\mu$K by adjusting the field gradient and laser frequency. The laser beams were then switched off and the magnetic trap (a TOP trap in this experiment), was quickly switched on. The magnetically trapped atoms were compressed by adiabatically increasing the quadrupole field. This produced a sample of $4 \times 10^6$ atoms in the trap with

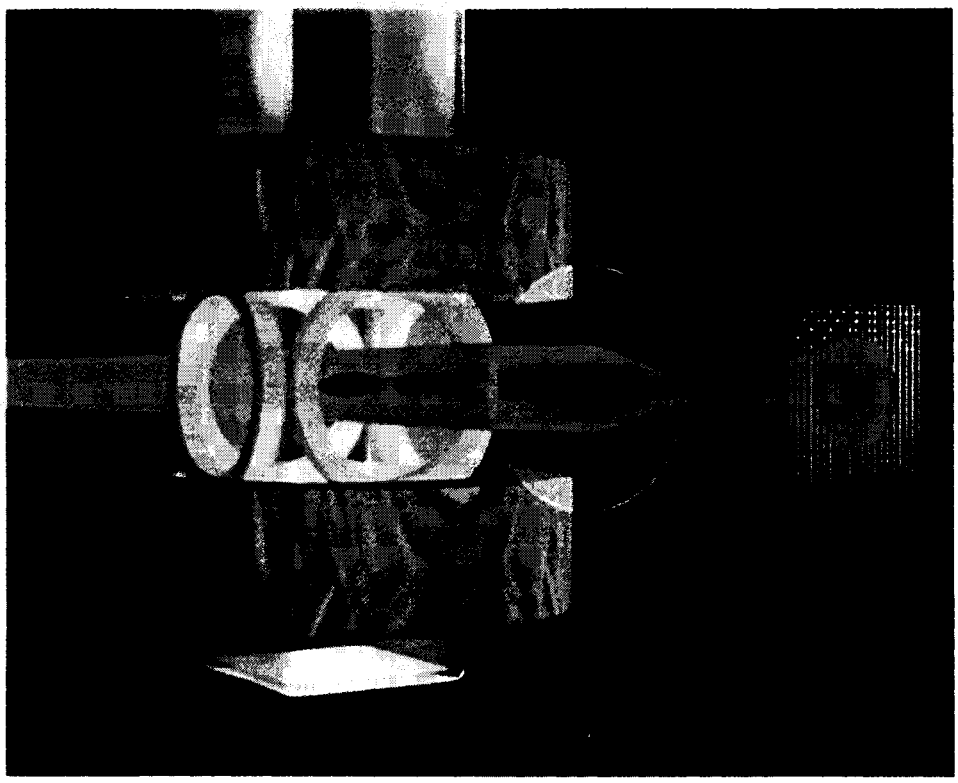

Fig. 11. – Absorption imaging method. (Figure courtesy of S. Wieman.)

a temperature of about 90 $\mu$K and an average density of about $2 \times 10^{10}$ atoms/cm$^3$. The trap had an axial oscillation frequency of 120 Hz. Evaporative cooling was then applied for about 70 s. During this time, the rf frequency was ramped down from the initial value to the final value that determined the final temperature. At the end of the evaporative cooling, the magnetic trap was switched off, letting the atoms expand freely. After 60 ms of expansion, the cloud was observed using an absorption imaging technique. The atoms were irradiated with a resonant laser beam for 20 $\mu$s and the shadow produced by the atoms was imaged on a charge-coupled-device (CCD) array, as described in the following.

**3·2.** *Observation of a Bose condensate.* – As mentioned above, in the experiments performed so far, at the end of the cooling process the atoms distribution was observed by imaging with an optical probe. Two major approaches have been followed: The first is absorption imaging of the sample, the second is based on the detection of refractive effects caused by the atoms.

Absorption imaging was used, for example, in [8, 9]. The atoms were illuminated with a short pulse of resonant light and the shadow of the cloud was imaged onto a CCD detector (fig. 11). Because of the high optical density ($D \approx 100$–$300$) of the atom cloud, however, quantitative measurements could not be performed by direct imaging of the atoms in the trap. At the end of the evaporative cooling, the cloud was allowed to expand by switching off the trapping fields and the absorption image was recorded after a time of several milliseconds. The larger size of the sample after the expansion also reduces spatial resolution requirements for the optical system. A result is shown in fig. 12. This method of observation corresponds to a 2-dimensional time-of-flight measurement of the

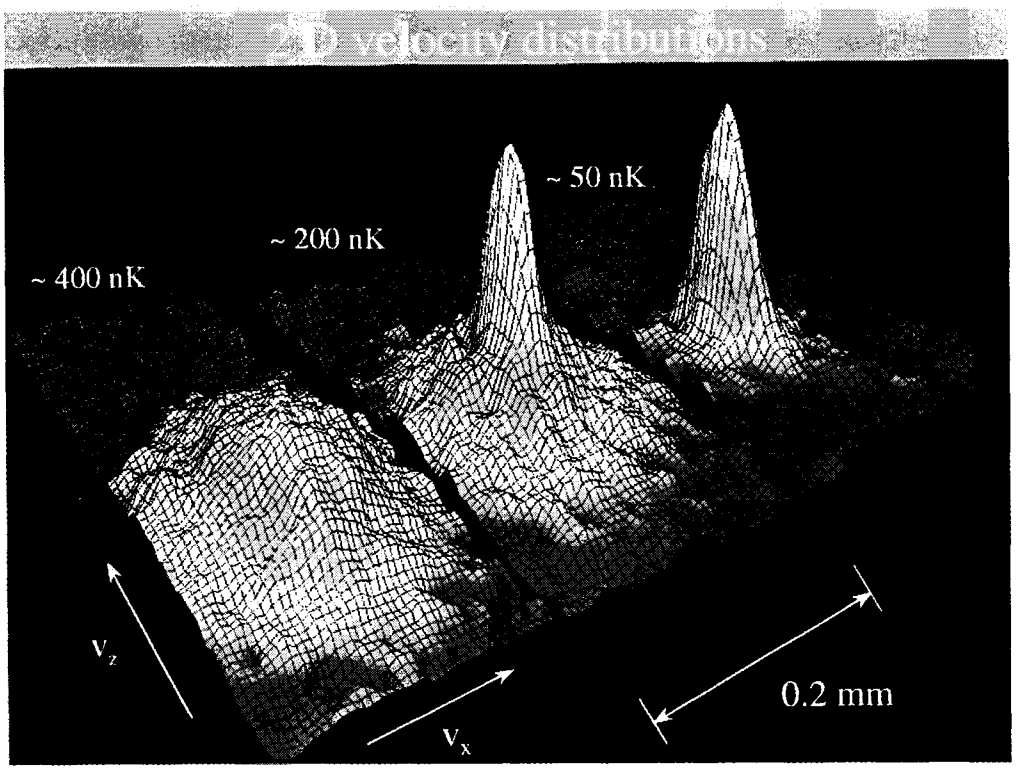


Fig. 12. – False-color images showing the velocity distribution of a sample of cold $^{87}$Rb atoms. Left: before condensation, center: just after the transition, right: for a nearly pure condensate. Images were recorded by the absorption imaging method after releasing the atoms from the trap and letting them expand freely. (Figure courtesy of E. A. Cornell.)

velocity distribution. The recorded image gives the initial velocity distibution of the atoms in the trap. However, for a harmonic confining potential, the spatial distribution and the velocity distribution are the same. From a single image, information can then be extracted on the density and the temperature of the atoms in the trap. This method is obviously a destructive observation method because each atom scatters several photons while being probed, heating the gas. Experiments are therefore performed by repeated cycles of load-evaporation-probing.

An alternative method to observe the condensate was demonstrated in [63]. By using a so-called dark-ground imaging technique [64], the dispersively scattered light was observed. In the dark-ground imaging technique, a collimated probe beam is sent through a weakly absorbing sample (fig. 13). The coherently scattered light is collected with a lens system and imaged onto a camera. The probe beam is blocked after passing the sample by inserting a small opaque object at the position where the beam comes to a focus. If $\mathbf{E}_0$ is the electric field of the incident probe beam, after passing through the sample it acquires a spatially dependent phase $\beta = \varphi + i\alpha/2$ so that the transmitted electric field is given by $\mathbf{E} = \mathbf{E}_0\, e^{i\beta}$. When the opaque object is inserted to block the incident beam, the resulting intensity is given by $I_s = E_0^2 \mid e^{i\beta} - 1 \mid^2$. In the case $\alpha \ll \mid \varphi \mid \ll 1$, the resulting signal is $I_s \approx E_0^2\varphi^2 = I_0\varphi^2$.

Dispersive imaging offers two important advantages with respect to absorption imaging. First, because the signal depends on the phase shift $\varphi$, it is possible to detune the frequency of the probe light from resonance at values for which the optical density is

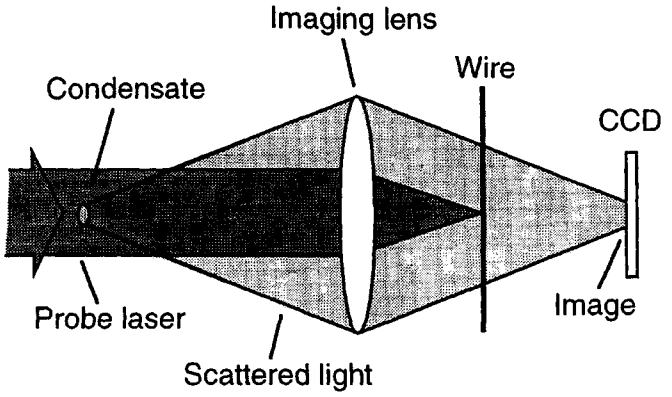


Fig. 13. – Schematic of dark-ground imaging method.

small. This allows probing of dense clouds of atoms directly in the trap. Second, dispersive imaging can be a nondestructive detection method. In [63], it was demonstrated that by probing the condensate with a pulse of off-resonant light, several consecutive images of the same condensate could be taken with no observable deterioration of the signal (fig. 14). Indeed, in dispersive scattering the photons are elastically scattered by a small angle. Also, if a light pulse duration longer than the oscillation period in the trap is used, no momentum is transferred to the atoms on the average.

When the phase shift $\varphi$ is small, the dark-ground signal is small because it depends on $\varphi^2$. A signal linear in $\varphi$ can be obtained by a phase-contrast imaging method [11,65]. *In situ* imaging allowed the MIT group to observe the propagation of sound in a condensate,

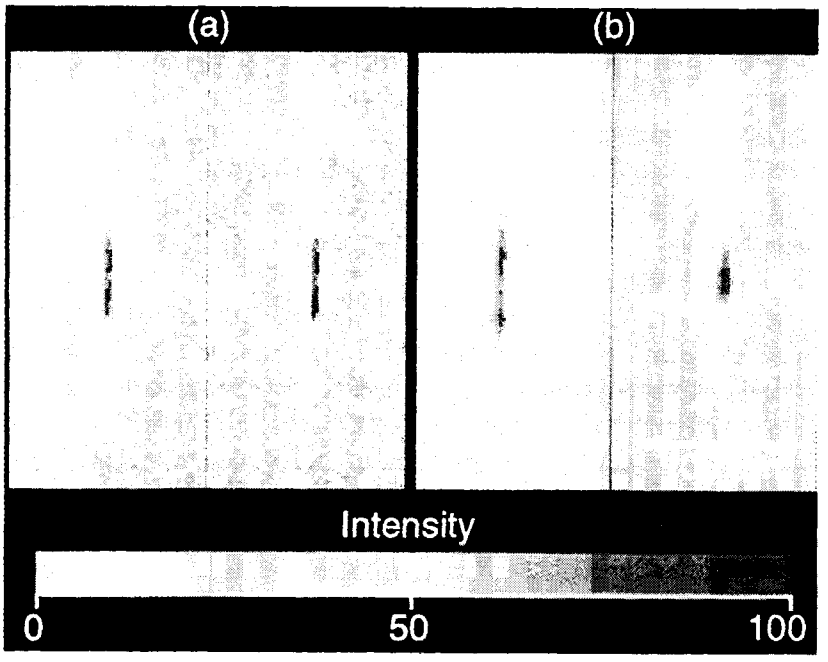


Fig. 14. – Nondestructive observation of a condensate. (A) Images of the same condensate taken 1 s apart. (B) Two pictures taken 6 s apart during decompression of the cloud. (From M. R. Andrews *et al.* (1996), with permission.)

to study the formation of the condensate and to directly observe the collective excitations. In [11], the birefringence of the sample of atoms polarized in the trap magnetic field was probed using a linearly polarized laser beam. After passing through the atomic sample, the polarization of the probe beam was analyzed with a polarizer. The intensity of the transmitted light was measured with a photodetector. This detection method allowed *in situ* imaging of condensates with only $\sim 10^3$ atoms.

Some remarks can be made concerning dispersive imaging detection methods. As discussed above, they can be considered as nondestructive detection methods. In fact, the phase of the condensate is changed under the effect of light. Only the number of atoms in the condensate can be measured in this way. Also, one could expect light scattering to be affected by the quantum degenerate state of the atoms. Such effects are negligible, however, under typical experimental conditions [66].

**3·3.** *Measurement of energy and ground-state occupation as a function of temperature.* Images of the ultra-cold atoms as the one shown in fig. 12, obtained by resonant absorption imaging, contain a wealth of information about important thermodynamic quantities. The integrated area under the distribution gives the total number, $N$, of atoms in the sample. The number of atoms in the ground state of the system, $N_0$, can be obtained from the integrated area under the narrow feature centered on zero velocity. The mean square radius of the expanded cloud as a function of time gives the mean square velocity, that is average energy, of the atoms. The temperature, $T$, can also be extracted from the analysis of the images. From the data on mean energy as a function of temperature, the specific heat can be determined, that is an important quantity in the study of phase transitions. At high densities of condensed atoms, the repulsive mean-field energy becomes important and can be measured.

In the work reported in ref. [67], a series of images of ultra-cold clouds of $^{87}$Rb atoms were analyzed to extract the ground-state occupation and the mean energy as a function of temperature. The number of atoms in the ground state was defined as the number of atoms contributing to the central feature in the optical-depth images. The condensate shape was fit with a 2-d Gaussian. The width, aspect ratio and peak height were found to be functions only of the number of atoms in the feature. The procedure gave consistent values of $N_0$ for temperatures down to about one half of the transition temperature. The temperature was determined by fitting a Gaussian to the high-energy tail of the velocity distribution. This procedure is based on the assumptions that the high-energy part of the velocity distribution remains in thermal equilibrium with the central part of the cloud and that it can still be described by a Maxwell-Boltzmann distribution because the density of the atoms in the outer part of the cloud is lower. Figure 15 shows the data obtained for the ground-state fraction $N_0/N$ as a function of scaled temperature $T/T_0$. The scale temperature, $T_0$, is the critical temperature for a noninteracting gas in the thermodynamic limit. The solid line in the figure shows the behaviour expected for the ideal gas of bosons in an anisotropic potential in the limit of infinite number of atom: $N_0/N = 1 - (T/T_0)^3$. The dotted line shows the curve calculated including finite-number corrections [68,69]. The dashed line is, instead, a least-squares fit of the data with the function $N_0/N = 1 - (T/T_c)^3$, with $T_c$ as a parameter. The fit gives a value for the critical temperature $T_c = 0.94(5)T_0$. The accuracy of the data is however too low to show a difference between $T_c$ and $T_0$. An accurate measurement of the critical temperature would allow to test theories taking into account mean-field [70,71] or many-body [72] interaction effects.

From the same images analyzed to measure the ground-state fraction, information

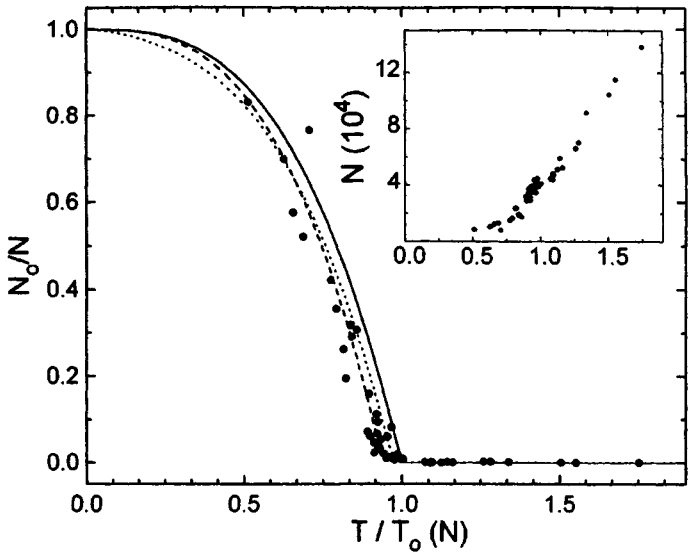


Fig. 15. Total number of atoms (inset) and ground-state fraction as a function of scaled temperature $T/T_0$. (From J. R. Ensher *et al.* (1996), with permission.)

on the energy and specific heat was obtained. The specific heat is usually defined as the temperature derivative of the energy per particle at constant pressure or constant volume. In this case it is given by the slope of the scaled energy *vs.* temperature plot with the confining potential held constant. The result is shown in the inset of fig. 16 and compared with the specific heat of other relevant systems. The data indicate the presence of a step in the specific heat near the empirical transition temperature. The observed step is smaller than the one predicted by a finite-number, ideal-gas theory [68,69]. The difference can be explained as an effect of interactions.

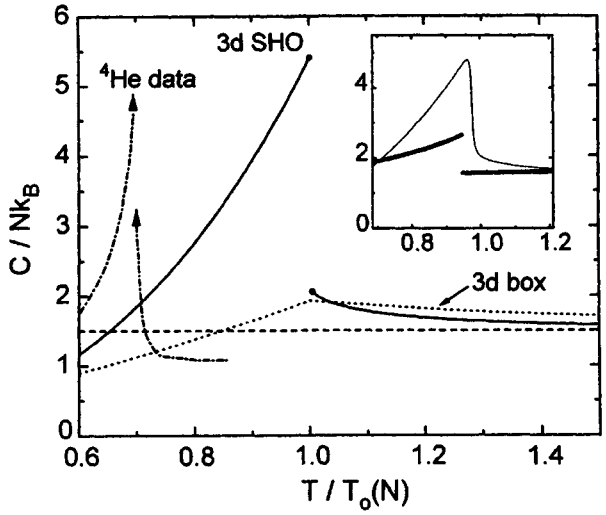


Fig. 16. – Specific heat as a function of scaled temperature $T/T_0$ for various theories and experiments. The inset shows the experimentally determined specific heat (bold line) and the theoretical prediction for a finite number of ideal bosons in a harmonic trap. (From J. R. Ensher *et al.* (1996), with permission.)

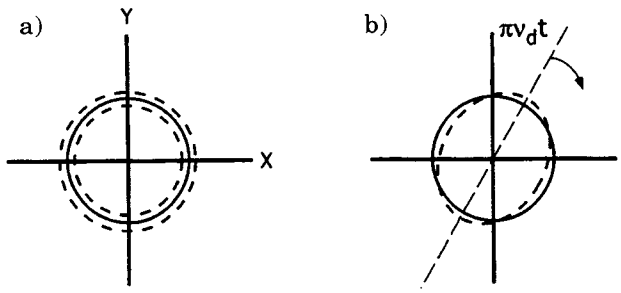


Fig. 17. – Equipotential contours for the two trap perturbations corresponding to the $m = 0$ and $m = 2$ collective modes. (From D. S. Jin *et al.* (1996), with permission.)

A related work was performed at MIT on trapped Na atoms [48]. The dependence of the condensate fraction on temperature and the interaction energy as a function of the number of atoms in the condensate were investigated. The study of the effect of interaction energy was made possible by the high density of atoms achieved in the new "cloverleaf" trap. The measured interaction energy per atom showed a good agreement with the $N_0^{2/5}$ behaviour expected from the theory.

**3·4.** *Study of collective excitations and propagation of sound in a Bose-Einstein condensate.* – The collective excitations of the Bose-Einstein condensate have been studied both by the JILA group and by the MIT group. The excitation of the lowest collective modes of the condensates in the trap was achieved by a time-dependent perturbation of the magnetic trap potential. For a noninteracting gas, all modes have frequencies which are integer multiples of the trap frequency. Deviations from this behaviour are expected as an effect of interatomic interactions. In the mean-field picture, the interaction term in the Gross-Pitaevskii equation depends on $Na\sqrt{\nu}$, where $N$ is the number of atoms, $a$ is the scattering length and $\nu$ is the trap frequency. The normal modes of the condensate can be classified by a quantum number $m$ that gives the angular momentum projection in the direction of the trap symmetry axis. In [73] the $m = 0$ and $m = 2$ modes of a dilute condensate of $^{87}$Rb were investigated and their frequency measured as a function of the interaction strength. The $m = 0$ mode corresponds to an oscillation in radial size. The $m = 2$ mode resembles an ellipse whose major axis rotates in the plane orthogonal to the trap axis (fig. 17). The measured frequencies for the two excitation modes as a function of the interaction strength are shown in fig. 18. In the figure, the experimental data are compared with the theoretical predictions based on mean-field theory. The measured frequencies deviate from the harmonic trap values showing a fairly good agreement with theoretical calculations.

A similar experiment was performed by the MIT group on a sodium condensate. They studied $m = 0$ oscillations. The measured frequency 30.0(2) Hz agreed with the theoretical prediction $\sqrt{5/2}\,\nu_z$ [74]. The oscillations observed in this experiment showed a damping with a decay time, for a nearly pure condensate, of 250(40) ms for the oscillation at $\sim$ 30 Hz. Measurements on a thermal cloud ($T/T_c \approx 2$) gave a damping time of 80 ms for oscillations at a frequency of 35(4) Hz = $1.2(2)\nu_z$.

The dependence of the damping rate and of the oscillation frequencies on the sample temperature was studied in [75, 76]. In particular, temperatures were investigated for which both condensate and noncondensate atoms are present, a regime which is not well understood theoretically. In [75], the $m = 0$ and $m = 2$ modes were studied with the

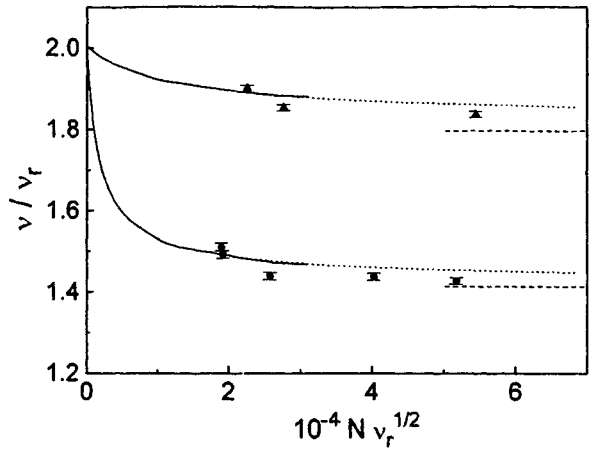


Fig. 18. – Measured frequencies for the $m = 0$ (triangles) and $m = 2$ (circles) excitation modes as a function of the interaction strength. Lines show the result of mean-field calculations. (From D. S. Jin *et al.* (1996), with permission.)

same technique used in [73]. The main results of this work can be summarized as follows (fig. 19): A temperature-dependent shift of the excitation frequencies of the condensate can be observed, with the two modes shifting in opposite directions. In addition, for the $m = 0$ mode, a sharp feature in the temperature dependence is observed at $T \approx 0.62\, T_c$. This feature is not observed for the $m = 2$ mode. For both the $m = 0$ and $m = 2$ condensate excitations the damping rate quickly decreases with decreasing temperature. The two decay rates show the same behaviour. Interestingly, at temperatures where both condensed and noncondensed atoms are present, the condensate excitations are observed to decay more rapidly than the ones of noncondensed atoms. In the MIT experiment [76], collective excitations of the Bose gas at nonzero temperatures were studied for large condensates and in conditions corresponding to the hydrodinamic limit. The hydrodynamic oscillation of the thermal cloud, corresponding to the first sound, was observed. Also, an antisymmetric oscillation of the thermal cloud and the condensate, analogous to the out-of-phase second sound mode in liquid helium was identified. The results of this work cannot be completely explained with presently existing models and will certainly require a deeper investigation.

The propagation of sound in a dilute Bose-Einstein condensate was studied in [65]. Density perturbations were excited using the dipole force of a focused, blue-detuned laser beam. The propagation of sound waves was observed by recording rapid sequences of nondestructive phase contrast images.

The speed of sound $c(r)$ is given by [77-79]

$$c(r) = \sqrt{\frac{n(r)U}{2m}}, \tag{37}$$

where $n(r)$ is the local density, $m$ is the mass of the particles and $U = 4\pi\hbar^2 a/m$ gives the interaction of bosons with scattering length $a$. The basic idea of the experiment reported in [65] is schematically shown in fig. 20. A condensate was formed, as in the other experiments described above, with the atoms confined in a magnetic trap. At time $t = 0$, the blue-detuned laser beam was switched on or off. The beam was focused at the center of the trap. The wavelength used (514 nm) was far enough from the sodium resonance

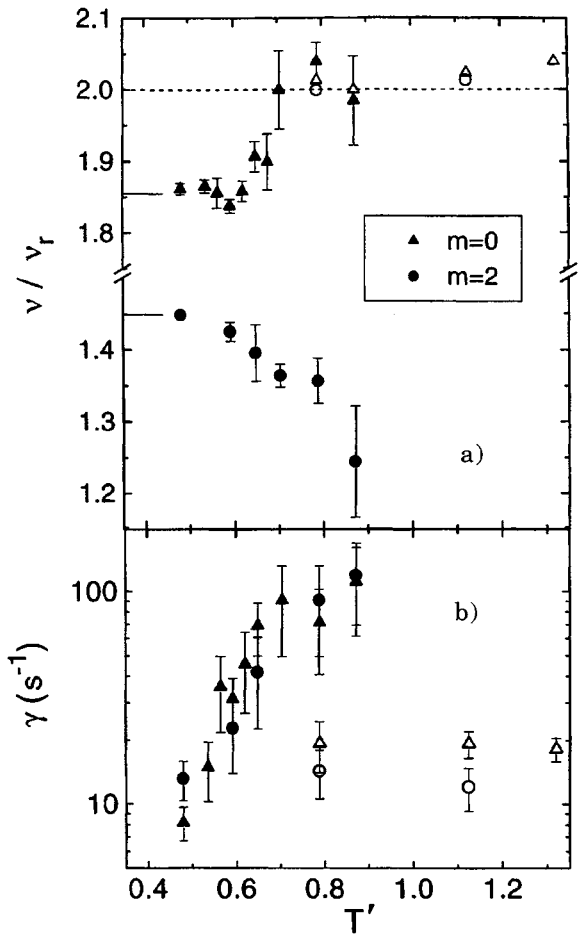


Fig. 19. – Temperature-dependent excitation spectrum: (a) Frequencies for $m = 0$ (triangles) and $m = 2$ (circles) modes in the case of the condensate (solid symbols) and noncondensate (open symbols) clouds. (b) Damping rate. (From D. S. Jin *et al.* (1997), with permission.)

at 589 nm to make heating from spontaneous emission negligible. If the laser beam was switched on after producing the condensate, the effect was to push the atoms out from the center of the trap creating two density peaks that propagated outward. If the focused laser beam was kept on during the evaporative cooling and switched off after the formation of the condensate, negative density perturbations were generated propagating outward with the same speed. The speed of sound was determined by measuring the position of the density peaks as a function of time. The resulting value was in good agreement with the value expected from eq. (37) (fig. 21).

**3·5.** *Condensation of atoms with attractive interactions.* – The experiments that first clearly showed BEC in dilute gases were performed on $^{87}$Rb [8] and $^{23}$Na [9]. Both these atomic species have a positive $s$-wave scattering length $a_s$, indicating that for cold atoms the interatomic interaction is repulsive. Evidence for Bose-Einstein condensation of $^{7}$Li, an atom for which $a_s$ is known to be negative, was first published in [10] and later confirmed in [11] with more accurate values for the number of condensate atoms. In the mean-field theory, the interaction energy is given by $U = 4\pi\hbar^2 a_s n/m$, where $n$ is the density and $m$ is the mass of the atoms. If $a_s < 0$, the energy decreases with increasing $n$, so the condensate is not stable and tends to collapse. For atoms in a confining potential,

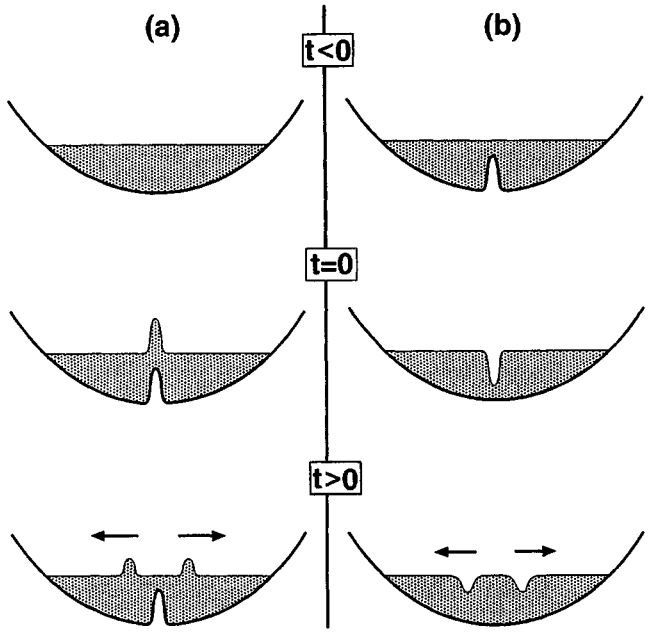


Fig. 20. – Scheme for the excitation of positive (a) or negative (b) density perturbations in a condensate using a focused, blue-detuned laser beam. The perturbations propagate at the speed of sound. (From M. R. Andrews *et al.* (1997), with permission.)

recent theories predicted, however, that the kinetic zero-point energy can balance the attractive interaction and lead to a metastable condensate with only a small number of atoms in the condensate [80, 81].

The experiment reported in [11] gave results in agreement with theoretical predictions. As discussed in subsect. **3**˙2, a phase-contrast technique was used to observe the atoms directly in the trap. In this experiment, a permanent-magnet trap was used, so that only *in situ* imaging was possible. For temperatures between 120 and 330 nK, the maximum condensate number was found to be between 650 and 1300. This result is consistent with what is expected from theory for the trap used in this experiment. Work is actually in

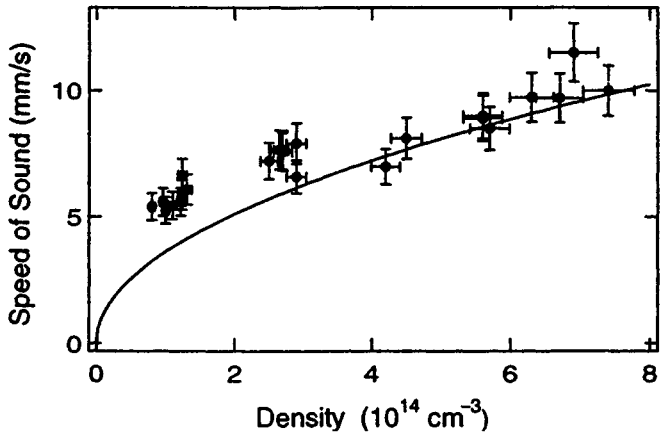


Fig. 21. – Speed of sound *vs.* condensate peak density. The solid line is the theoretical prediction. (From M. R. Andrews *et al.* (1997), with permission.)

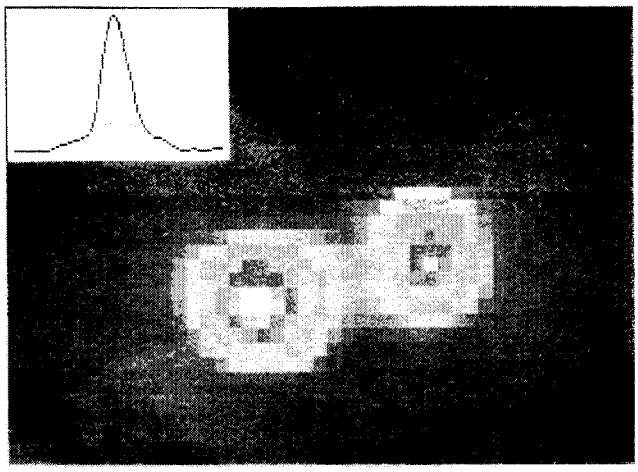

Fig. 22. – Absorption image showing two $^{87}$Rb condensates produced by evaporative cooling of atoms in the $|\ 1,-1\rangle$ state and sympathetic cooling of atoms in the $|\ 2,2\rangle$ state. (From C. J. Myatt *et al.* (1997), with permission.)

progress to study the effect of attractive interactions on BEC also for other atoms, such as $^{85}$Rb, for which the $s$-wave scattering length is predicted to be negative.

A related subject under investigation is the observation of the so-called Feshbach resonances [82] in the scattering length of alkali atoms [83]. Such resonances could allow to control the magnitude or even the sign of the scattering length by applying external magnetic, optical or radio-frequency fields. Feshbach resonances were recently observed in an experiment performed at MIT on Bose-Einstein condensates of Na atoms [84]. A key ingredient in this experiment was the possibility of confining the condensate in an optical dipole trap [85]. It was predicted indeed that Feshbach resonances in Na would be observed for a relatively small applied magnetic field only for atoms in high-magnetic-field seeking states. Since these atoms cannot be trapped in magnetic traps, they were confined using the optical trap. The occurrence of the resonances was detected by two methods: The enhancement in the rate of inelastic collisions was detected as an increase of the losses of atoms from the trap as the magnetic field was swept across the resonance. Also, a clear evidence for a dispersive variation of the scattering length around the resonance was obtained by measuring the interaction energy for the trapped condensate *vs.* magnetic field by the time-of-flight absorption imaging method.

**3·6.** *Production of two condensates by sympathetic cooling.* – In [51], a cooling method called sympathetic cooling was used to produce two overlapping condensates made of $^{87}$Rb atoms in two different spin states. In sympathetic cooling, an atomic species is cooled via collisions with another species at a lower temperature. This method was first developed to cool ions in ion traps [86]. It had never been used before to cool neutral atoms, where interactions are in general weaker. In the experiment reported in [51], the two species corresponded to $^{87}$Rb atoms in the $|\ F=1, m=-1\rangle$ and $|\ F=2, m=2\rangle$ spin states. Trapped atoms in the $|\ F=1, m=-1\rangle$ state were cooled, by evaporative cooling, down to Bose-Einstein condensation as in other experiments described above. In this case, however, atoms in the other spin state were left in the trap and observed at the end of the cooling process. Figure 22 shows the absorption image recorded by probing the atoms in $F=2$ and the atoms in $F=1$. In this case, the trap axis was slightly tilted with respect to the horizontal plane so that gravity produced a separation of the two

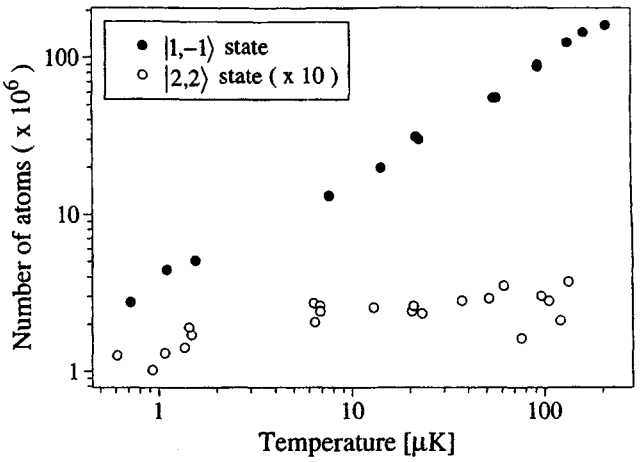


Fig. 23. – Number of atoms in the $|\ 1,-1\rangle$ and $|\ 2,2\rangle$ states for different temperatures during the sympathetic-evaporative cooling process. (From C. J. Myatt *et al.* (1997), with permission.)

condensates. With a well-aligned trap, however, nearly perfectly overlapping condensates were obtained. Because of the different magnetic moments, evaporative cooling acts preferentially on the atoms in the $|\ F=1, m=-1\rangle$ state which are less tightly confined in the trap. Therefore the evaporative cooling process leaves the initial number of atoms in the $|\ F=2, m=2\rangle$ state nearly unchanged (fig. 23). The study of the behaviour of the condensates provided important information on collisional parameters. By measuring the densities and loss rates for the atoms in the two states for various overlapping conditions, it was possible to determine the rate constant for binary inelastic collisions such as spin-exchange collisions. Another interesting result came from the observation that in the presence of the two condensates, the $|\ F=2, m=2\rangle$ condensate was displaced upward from its equilibrium position because of interaction with the $|\ F=1, m=-1\rangle$ condensed atoms. This provided an indication that the interaction between the two condensates is repulsive.

The demonstration of the possibility of cooling a sample of atoms down to quantum degeneracy using sympathetic cooling is of great interest because of possible applications to other species. In particular, sympathetic cooling might allow the achievement of quantum degeneracy conditions in a gas of fermionic atoms. For spin-polarized fermionic atoms, in fact, simple evaporative cooling is not efficient because $s$-wave collisions are not possible for atoms in the same state. Also, the two fermionic atoms for which experiments are presently in progress, namely $^6$Li [87] and $^{40}$K [88], have a low natural abundance so that it is important to use a cooling technique which does not require a large initial number of atoms. More generally, sympathetic cooling may enable the achievement of Bose-Einstein condensation of atoms for which evaporative cooling does not work efficiently.

**3·7.** *The coherence properties of the condensate and the "atom laser".* – A gas of bosons all occupying the same state is described by a macroscopic wave function that is the solution of the nonlinear Schrödinger equation. Therefore, a Bose condensate should show coherence properties analogous to the ones of laser light. Such properties were investigated experimentally starting with the most striking effect, that is interference of the "matter waves" of two Bose condensates [89]. In this experiment, Na atoms were confined in a trap created by focusing a blue-detuned light sheet at the center of a "cloverleaf"

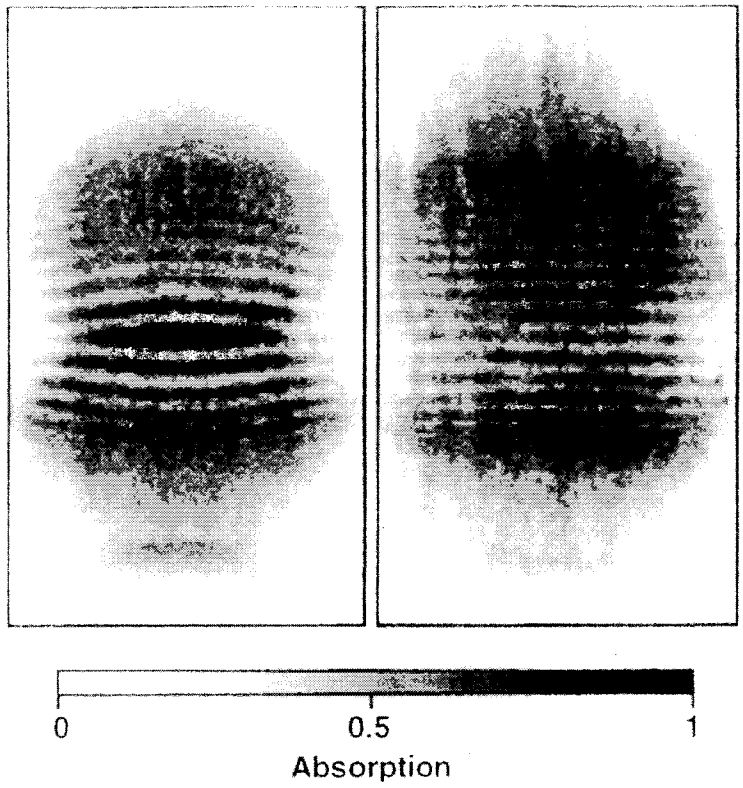


Fig. 24. – Interference of two expanding condensates, for two different powers of the light sheet used to produce the double condensate. (From M. R. Andrews *et al.* (1997), with permission.)

magnetic trap. The combination of magnetic force and optical dipole force produced a double-well potential. After evaporative cooling, two separate Bose condensates were produced instead of the single cigar-shaped condensate usually produced in the simple magnetic trap. The distance between the condensates could be varied by changing the intensity of the laser light. The overlapping of the two condensates was obtained by switching off the trap and letting the condensates expand. The interference pattern was observed by absorption imaging. In order to increase the spatial resolution, only a thin slice of the cloud was observed. This was achieved by first optically pumping the atoms in the relevant part of the cloud into a given hyperfine state using a thin sheet of light and then probing the atoms in this state with a pulse of resonant light. Figure 24 shows the interference of two condensates as observed, after 40 ms of expansion, for two different intensities of the blue-detuned laser light in the trap. Nearly straight fringes can be observed with a contrast that, after calibration, was found to be in the range 50%–100%. The measured spacing between the fringes, $\sim$ 20 $\mu$m and $\sim$ 15 $\mu$m, respectively, was consistent with the value of the de Broglie wavelength $\lambda$ associated with the relative motion of the atoms

$$\lambda = \frac{ht}{md}, \tag{38}$$

where $h$ is Planck's constant, $m$ is the atomic mass, $d \sim 30$–$40$ $\mu$m was the initial spatial separation between the condensates and $t = 40$ ms was the expansion time before the observation. The slight curvature of the fringes in fig. 24a was attributed to the effect of

interactions which becomes nonnegligible for small separations of the two condensates. The main result of this work was to demonstrate the first-order coherence of a Bose condensate and long-range correlations over the extent of the condensate. The methods developed allowed for the first time to address experimentally the debated question of the phase of a Bose-Einstein condensate showing the existence of such a phase and the possibility of comparing the phases of two condensates.

Higher-order coherence properties of the condensate were studied in [90]. Starting from the analogy between the intensity fluctuations in a light beam and the density in an atomic sample, information on statistical correlations in a condensate was obtained by studying three-body recombination rates. Indeed, in [91] it was calculated that the rate of three-body recombination in a condensate for noninteracting atoms should be reduced by a factor 3! with respect to the corresponding rate in a thermal cloud with the same mean density. In the experiment reported in [90], collision rates were inferred from the loss rate of atoms from the trap. Three-body recombination processes could be distinguished from other loss processes by measuring the loss rate as a function of density. By comparing the data obtained for noncondensed and condensed samples, it was found that the three-body recombination rate was smaller in the case of a condensate by a factor 7.4 (2.0). The measured value is then in agreement with the theoretical value of 3! and demonstrates that density fluctuations are reduced in a condensate relative to a thermal gas. In the language of quantum optics, condensate atoms appear to be less bunched than thermal atoms.

Several papers have recently discussed the analogies between coherent matter and coherent light [92-96]. One of the most interesting prospects in this field is the realization of an "atom laser". In fact, atoms in a magnetic trap can be considered as analogous to photons in an optical cavity. The thermal cloud of ultracold atoms plays the role of the active medium and, in the experiments performed so far, evaporative cooling acts as the "excitation" mechanism which makes the atoms accumulate into a single state of the trap. It is obvious that, contrary to the photon case, the number of atoms cannot be amplified. However, the enhanced probability for bosons to occupy an already occupied state of the system can be seen as the analogue of an amplification mechanism. A key element in the realization of the "atom laser" is the possibility of coupling out particles in a coherent way. The simplest way to couple atoms out of the condensate is to switch off the trapping potential and let the atoms fall under the effect of gravity. A more controlled method was demonstrated in [97]. Rf radiation was used to create Bose condensates in a superposition of trapped and untrapped states. After producing a condensate of $5 \times 10^6$ sodium atoms in the $F = 1$, $m_F = -1$ ground state, a resonant rf magnetic field was switched on with a polarization orthogonal to the magnetic field at the trap center. This coupled a part of the trapped atoms into the $m_F = 0$ and into the $m_F = 1$ states. Atoms in the $m_F = 1$ state were repelled from the trap while the untrapped $m_F = 0$ atoms expanded freely while moving downward under the effect of gravity. The amplitude of the rf pulse could be adjusted to get an out-coupling of atoms between 0% and 100%. Interestingly, by varying the intensity of the rf pulse, Rabi oscillations were observed with the same Rabi frequency as for the single atom. Using subsequent rf pulses, multiple pulses of atoms out of the condensate were obtained (fig. 25). In the same work, another output coupler scheme was demonstrated using a nonadiabatic rf sweep through resonance to transfer atoms into the untrapped states. This scheme is less sensitive than the other to changes in the bias magnetic field of the trap. In the same work, the possibility of taking advantage of Majorana spin-flips as an out-coupling mechanism was also shown.

In [89], a test of the coherence of the pulses of atoms was performed. Pulses from two

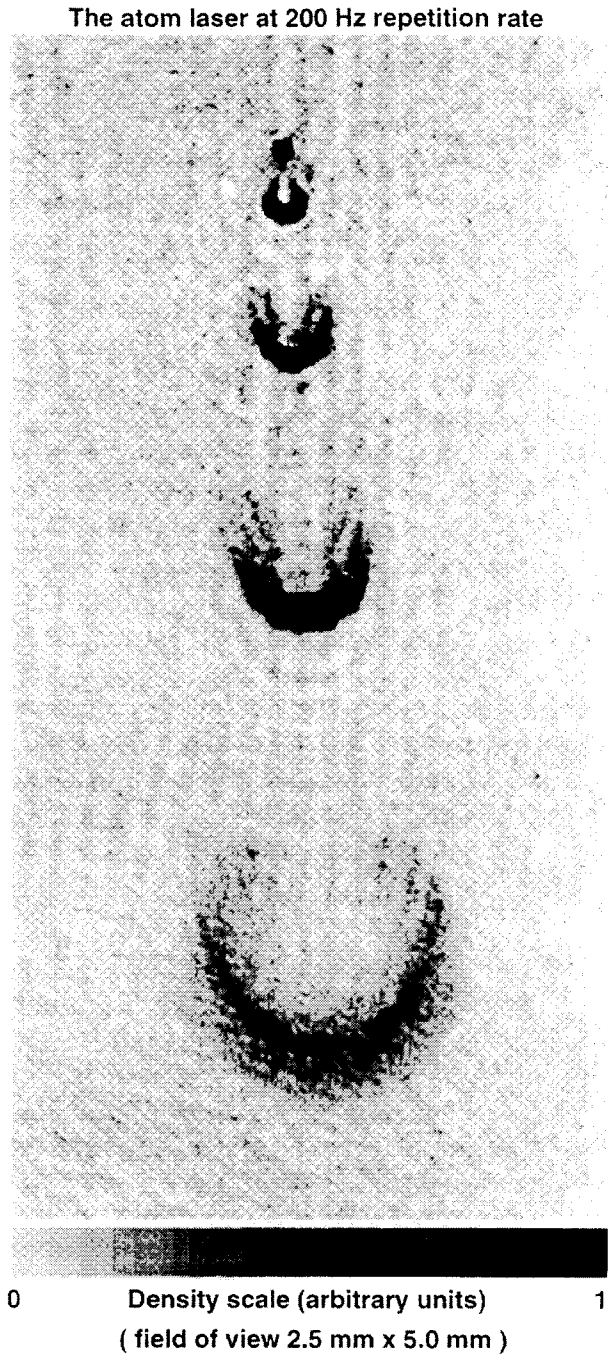


Fig. 25. – Atom laser. The figure shows successive pulses of coherent sodium atoms coupled out from a Bose-Einstein condensate. (Figure courtesy of W. Ketterle.)

separate condensates were combined and high-contrast interference fringes were observed. This completed the proof that a Bose condensate with an out-coupling mechanism such as the one just described can be considered as a realization of an "atom laser".

## 4. – Conclusions and future prospects

At the time of this writing, almost three years have passed since the first observation of BEC in atomic gases. The laboratories where BEC was first achieved had the possibility of investigating a wide range of interesting phenomena some of which had been predicted theoretically but never studied experimentally in such simple and well-controlled systems. During this time, several laboratories in the world have been trying to reproduce the experiments and to achieve BEC.

Recently, a few laboratories announced the observation of BEC: D. Heinzen's group at the University of Texas at Austin observed BEC of $^{87}$Rb atoms using a Zeeman-slowed atomic beam and evaporative cooling of the atoms in a TOP magnetic trap. L. Hau and collaborators at the Rowland Institute in Cambridge, MA, used a Zeeman-slowed atomic beam of Na and a Ioffe trap. The group of M. Kasevich, at Stanford University, achieved BEC of $^{87}$Rb atoms with a single vapor cell and a TOP trap. At the University of Konstanz in Germany, the group of G. Rempe observed BEC of $^{87}$Rb atoms in a double MOT apparatus with a Ioffe-type magnetic trap. In the laboratory of T. Hänsch at the University of Munich/MPI for Quantum Optics, BEC of $^{87}$Rb was achieved using a double-MOT apparatus and a Ioffe-type magnetic trap. The group of W. Phillips at NIST, Gaithersburg achieved BEC with sodium using a Zeeman-cooled atomic beam and a TOP trap. It is interesting to notice that in this experiment BEC was reached also by evaporating only with the "circle of death" of the TOP trap. At the Ecole Normale Superieure in Paris, J. Dalibard and colleagues observed BEC of rubidium atoms using an apparatus based on a double-MOT and a Ioffe-type magnetic trap.

The experimental results also stimulated a lot of theoretical work and several papers were published interpreting the new observations and proposing new possible experiments.

Amongst the future challenges one can envisage the achievement of BEC with other atoms. Of particular interest are H and He$^*$. Work is also in progress on K [49], Cs [52,98], and even on molecules [99].

The effect of interactions needs to be further investigated. The case of atoms with attractive interactions and the possibility of modifying the strength of the interaction by external fields are certainly important subjects to be further explored.

There are important phenomena that have been predicted theoretically and observed in other systems. Notable examples are vortices and second sound that have been widely investigated in superfluid helium. The study of these phenomena in the well-controlled conditions of experiments with dilute atomic gases will provide important information.

The possibility of manipulating the condensates should allow studies of tunnelling effects between two condensates and the observation of Josephson-type phenomena.

The future possibilities of atom lasers can be imagined considering the major impact that optical lasers had in several fields.

Finally, one of the most interesting prospects is to investigate the properties of an ultracold gas of fermionic atoms. At phase space densities similar to the ones achieved in BEC experiments, the behaviour of a degenerate Fermi gas may be studied and, at still lower temperatures, the superfluid phase transition could be observed [100-103]. Promising candidates which are presently investigated are $^6$Li [87] and $^{40}$K [88].

*Note added in proofs.* – After the completion of this review, many interesting papers appeared reporting new results in the investigation of BEC. An extensive review of the theory of BEC in trapped gases has been published in [104]. A discussion of recent

theoretical and experimental results can be found in the proceedings of the E. Fermi School on "Bose-Einstein condensation in atomic gases" held in Varenna in the summer 1998 [105]. During that School, the first evidence of BEC in atomic hydrogen was presented [106].

* * *

The authors thank J. R. ENSHER for a critical reading of the manuscript and E. A. CORNELL, W. KETTERLE, R. HULET, and J. DALIBARD for providing copies of figures.

REFERENCES

[1] EINSTEIN A., *Quantentheorie des einatomigen idealen Gases, Sitzungsber. Kgl. Preuss. Akad. Wiss.* (1924) 261.
[2] EINSTEIN A., *Quantentheorie des einatomigen idealen Gases, Zweite Abhandlung, Sitzungsber. Kgl. Preuss. Akad. Wiss.* (1925) 3.
[3] BOSE S. N., *Plancks Gesetz und Lichtquantenhypothese, Z. Phys.*, **26** (1924) 178.
[4] FERMI E., *Sulla quantizzazione del gas perfetto monoatomico, Rend. Lincei*, **3** (1926) 145.
[5] FERMI E., *Zur Quantelung des idealen einatomigen Gases, Z. Phys.*, **36** (1926) 902.
[6] HUANG K., *Statistical Mechanics*, second edition (Wiley, New York) 1987.
[7] GRIFFIN A., SNOKE D. W. and STRINGARI A. (Editors), *Bose Einstein Condensation* (Cambridge University Press, Cambridge) 1995.
[8] ANDERSON M. H., ENSHER J. R., MATTHEWS M. R., WIEMAN C. E. and CORNELL E. A., *Observation of Bose-Einstein condensation in a dilute atomic vapor, Science*, **269** (1995) 198.
[9] DAVIS K. B., MEWES M.-O., ANDREWS M. R., VAN DRUTEN N. J., DURFEE D. S., KURN D. M. and KETTERLE W., *Bose-Einstein condensation in a gas of sodium atoms, Phys. Rev. Lett.*, **75** (1995) 3969.
[10] BRADLEY C. C., SACKETT C. A., TOLLETT J. J. and HULET R. G., *Evidence of Bose-Einstein condensation in an atomic gas with attractive interactions, Phys. Rev. Lett.*, **75** (1995) 1687; **79** (1997) 1170.
[11] BRADLEY C. C., SACKETT C. A. and HULET R. G., *Bose-Einstein condensation of lithium: observation of limited condensate number, Phys. Rev. Lett.*, **78** (1997) 985.
[12] Special issue on: *Laser cooling and trapping of atoms*, edited by CHU S. and WIEMAN C., *J. Opt. Soc. Am. B*, **6** (1989) 2020.
[13] ARIMONDO E., PHILLIPS W. D. and STRUMIA F. (Editors), *Laser manipulation of atoms and ions, Proceedings of the International School of Physics E. Fermi, Varenna, Course CXVIII* (North-Holland, Amsterdam) 1992.
[14] CHU S., *The manipulation of neutral particles, Rev. Mod. Phys.*, **70** (1998) 685.
[15] COHEN-TANNOUDJI C., *Manipulating atoms with photons, Rev. Mod. Phys.*, **70** (1998) 707.
[16] PHILLIPS W. D., *Laser cooling and trapping of atoms, Rev. Mod. Phys.*, **70** (1998) 721.
[17] ERTMER W., BLATT R., HALL J. L. and ZHU M., *Laser manipulation of atomic beam velocities: Demonstration of stopped atoms and velocity reversal, Phys. Rev. Lett.*, **54** (1985) 996.
[18] PHILLIPS W. D. and METCALF H., *Laser deceleration of an atomic beam, Phys. Rev. Lett.*, **48** (1982) 596.
[19] HÄNSCH T. W. and SCHAWLOW A. L., *Cooling of gases by laser radiation, Opt. Commun.*, **13** (1975) 68.
[20] CHU S., HOLLBERG L., BJORKHOLM J. E., CABLE A. and ASHKIN A., *Three-dimensional viscous confinement and cooling of atoms by resonance radiation pressure, Phys. Rev. Lett.*, **55** (1985) 48.

[21] LETT P. D., WATTS R. N., WESTBROOK C. I., PHILLIPS W. D., GOULD P. L. and METCALF H. J., *Observation of atoms laser cooled below the Doppler limit, Phys. Rev. Lett.*, **61** (1988) 169.

[22] DALIBARD J. and COHEN-TANNOUDJI C., *Laser cooling below the Doppler limit by polarization gradients: simple theoretical models, J. Opt. Soc. Am.*, **6** (1989) 2023.

[23] UNGAR P. J., WEISS D. S., RIIS E. and CHU S., *Optical molasses and multilevel atoms: theory, J. Opt. Soc. Am.*, **6** (1989) 2058.

[24] SALOMON C., DALIBARD J., PHILLIPS W. D., CLAIRON A. and GUELLATI S., *Laser cooling of cesium atoms below 3 $\mu K$, Europhys. Lett.*, **12** (1990) 683.

[25] RAAB E. L., PRENTISS M., CABLE A., CHU S. and PRITCHARD D. E., *Trapping of neutral sodium atoms with radiation pressure, Phys. Rev. Lett.*, **59** (1987) 2631.

[26] STEANE A. and FOOT C., *Laser cooling below the Doppler limit in a magneto-optical trap, Europhys. Lett.*, **14** (1991) 231.

[27] MONROE C., SWANN W., ROBINSON H. and WIEMAN C., *Very cold trapped atoms in a vapor cell, Phys. Rev. Lett.*, **65** (1990) 1571.

[28] LINDQUIST K., STEPHENS M. and WIEMAN C., *Experimental and theoretical study of the vapor-cell Zeeman optical trap, Phys. Rev. A*, **46** (1992) 4082.

[29] KETTERLE W., DAVIS K. B., JOFFE M. A., MARTIN A. and PRITCHARD D. E., *High densities of cold atoms in a dark spontaneous-force optical trap, Phys. Rev. Lett.*, **70** (1993) 2253.

[30] CHU S., BJORKHOLM J. E., ASHKIN A. and CABLE A., *Experimental observation of optically trapped atoms, Phys. Rev. Lett.*, **57** (1986) 314.

[31] MILLER J. D., CLINE R. A. and HEINZEN D. J., *Far-off-resonance optical trapping of atoms, Phys. Rev. A*, **47** (1993) R4567.

[32] LEMONDE P., MORICE O., PEIK E., REICHEL J., PERRIN H., HÄNSEL W. and SALOMON C., *An opto-electric trap for cold atoms, Europhys. Lett.*, **32** (1996) 555.

[33] DAVIDSON N., LEE H. J., ADAMS C. S., KASEVICH M. and CHU S., *Long atomic coherence times in an optical dipole trap, Phys. Rev. Lett.*, **74** (1995) 1311.

[34] ASPECT A., ARIMONDO E., KAISER R., VANSTEENKISTE N. and COHEN-TANNOUDJI C., *Laser cooling below the one-photon recoil energy by velocity-selective coherent population trapping, Phys. Rev. Lett.*, **61** (1988) 826.

[35] LAWALL J., KULIN S., SAUBAMEA B., BIGELOW N., LEDUC M. and COHEN-TANNOUDJI C., *Three-dimensional laser cooling of helium beyond the single-photon recoil limit, Phys. Rev. Lett.*, **75** (1995) 4194.

[36] ESSLINGER T., SANDER F., WEIDEMÜLLER M., HEMMERICH A. and HÄNSCH T. W., *Subrecoil laser cooling with adiabatic transfer, Phys. Rev. Lett.*, **76** (1996) 2432.

[37] KASEVICH M. and CHU S., *Laser cooling below a photon recoil with three-level atoms, Phys. Rev. Lett.*, **69** (1992) 1741.

[38] DAVIDSON N., LEE H. J., KASEVICH M. and CHU S., *Raman cooling of atoms in two and three dimensions, Phys. Rev. Lett.*, **72** (1994) 3158.

[39] REICHEL J., MORICE O., TINO G. M. and SALOMON C., *Subrecoil Raman cooling of cesium atoms, Europhys. Lett.*, **28** (1994) 477.

[40] REICHEL J., BARDOU F., DAHAN M. B., PEIK E., RAND S., SALOMON C. and COHEN-TANNOUDJI C., *Raman cooling of cesium below 3 nk: new approach inspired by Lévy flight statistics, Phys. Rev. Lett.*, **75** (1995) 4575.

[41] LEE H. J., ADAMS C. S., KASEVICH M. and CHU S., *Raman cooling of atoms in an optical dipole trap, Phys. Rev. Lett.*, **76** (1996) 2658.

[42] WING W., *Prog. Quantum Electron.*, **8** (1984) 181.

[43] KUGLER K. J., PAUL W. and TRINKS U., *A magnetic storage ring for neutrons, Phys. Lett. B*, **72** (1978) 422.

[44] MIGDALL A. L., PRODAN J. V., PHILLIPS W. D., BERGEMAN T. H. and METCALF H. J., *First observation of magnetically trapped atoms, Phys. Rev. Lett.*, **54** (1985) 2596.

[45] DOYLE J. M., SANDBERG J. C., YU I. A., CESAR C. L., KLEPPNER D. and GREYTAK T. J., *Hydrogen in the submillikelvin regime: sticking probability on superfluid $^4$He, Phys. Rev. Lett.*, **67** (1991) 603.

[46] LUITEN O. J., WERIJ H. G. C., SETIJA I. D., REYNOLDS M. W., HIJMANS T. W. and WALRAVEN J. T. M., *Lyman-α spectroscopy of magnetically trapped atomic hydrogen, Phys. Rev. Lett.*, **70** (1993) 544.

[47] DAVIS K. B., MEWES M.-O., JOFFE M. A., ANDREWS M. R. and KETTERLE W., *Evaporative cooling of sodium atoms, Phys. Rev. Lett.*, **74** (1995) 5202; **75** (1995) 2909.

[48] MEWES M.-O., ANDREWS M. R., VAN DRUTEN N. J., KURN D. M., DURFEE D. S. and KETTERLE W., *Bose-Einstein condensation in a tightly confining dc magnetic trap, Phys. Rev. Lett.*, **77** (1996) 416.

[49] PREVEDELLI M., CATALIOTTI F. S., CORNELL E. A., ENSHER J. R., FORT C., RICCI L., TINO G. M. and INGUSCIO M., *Trapping and cooling of potassium isotopes in a double-magneto-optical-trap apparatus, Phys. Rev. A*, **59** (1999) 886.

[50] PETRICH W., ANDERSON M. H., ENSHER J. R. and CORNELL E. A., *Stable, tightly confining magnetic trap for evaporative cooling of neutral atoms, Phys. Rev. Lett.*, **74** (1995) 3352.

[51] MYATT C. J., BURT E. A., GHRIST R. W., CORNELL E. A. and WIEMAN C. E., *Production of two overlapping Bose-Einstein condensates by sympathetic cooling, Phys. Rev. Lett.*, **78** (1997) 586.

[52] ARNDT M., BEN DAHAN M., GUERY-ODELIN D., REYNOLDS M. W. and DALIBARD J., *Observation of a zero-energy resonance in Cs-Cs collisions, Phys. Rev. Lett.*, **79** (1997) 625.

[53] KIM J., FRIEDRICH B., KATZ D. P., PATTERSON D., WEINSTEIN J. D., DECARVALHO R. and DOYLE J. M., *Buffer-gas loading and magnetic trapping of atomic europium, Phys. Rev. Lett.*, **78** (1997) 3665.

[54] BERGEMAN T., EREZ G. and METCALF H. J., *Magnetostatic trapping fields for neutral atoms, Phys. Rev. A*, **35** (1987) 1535.

[55] MAJORANA E., *Atomi orientati in campo magnetico variabile, Nuovo Cimento*, **9** (1932) 43.

[56] BERGEMAN T. H., MCNICHOLL P., KYCIA J., METCALF H. and BALAZS N. L., *Quantized motion of atoms in a quadrupole magnetostatic trap, J. Opt. Soc. Am. B*, **6** (1989) 2249.

[57] PRITCHARD D. E., *Cooling neutral atoms in a magnetic trap for precision spectroscopy, Phys. Rev. Lett.*, **51** (1983) 1336.

[58] GOTT Y. V., IOFFE M. S. and TEL'KOVSKII V. G., *Nucl. Fusion, Suppl.*, Pt. **3** (1962) 1045; 1284.

[59] HESS H. F., *Evaporative cooling of magnetically trapped and compressed spin-polarized hydrogen, Phys. Rev. B*, **34** (1986) 3476.

[60] HESS H. F., KOCHANSKI G. P., DOYLE J. M., MASUHARA N., KLEPPNER D. and GREYTAK T. J., *Magnetic trapping of spin-polarized atomic hydrogen, Phys. Rev. Lett.*, **59** (1987) 672.

[61] KETTERLE W. and VAN DRUTEN N. J., *Evaporative cooling of trapped atoms, Adv. At. Mol. Opt. Phys.*, **37** (1996) 181.

[62] WALRAVEN J. T. M., *Atomic hydrogen in magnetostatic traps,*, in *Quantum Dynamics of Simple Systems, Proceedings of the 44th Summer School in Physics, Stirling 1994*, 1996.

[63] ANDREWS M. R., MEWES M.-O., VAN DRUTEN N. J., DURFEE D. S., KURN D. M. and KETTERLE W., *Direct, nondestructive observation of a Bose condensate, Science*, **273** (1996) 84.

[64] HECHT E., *Optics*, second edition (Addison-Wesley, Reading, MA) 1989.

[65] ANDREWS M. R., KURN D. M., MIESNER H.-J., DURFEE D. S., TOWNSEND C. G., INOUYE S. and KETTERLE W., *Propagation of sound in a Bose-Einstein condensate, Phys. Rev. Lett.*, **79** (1997) 553-556; **80** (1998) 2967.

[66] MORICE O., CASTIN Y. and DALIBARD J., *Refractive index of a dilute Bose gas, Phys. Rev. A*, **51** (1995) 3896.

[67] ENSHER J. R., JIN D. S., MATTHEWS M. R., WIEMAN C. E. and CORNELL E. A., *Bose-Einstein condensation in a dilute gas: measurement of energy and ground-state occupation, Phys. Rev. Lett.*, **77** (1996) 4984.

[68] GROSSMANN S. and HOLTHAUS M., *On Bose-Einstein condensation in harmonic traps, Phys. Lett. A*, **208** (1995) 188.
[69] KETTERLE W. and VAN DRUTEN N. J., *Bose-Einstein condensation of a finite number of particles trapped in one or three dimensions, Phys. Rev. A*, **54** (1996) 656.
[70] BAGNATO V., PRITCHARD D. E. and KLEPPNER D., *Bose-Einstein condensation in an external potential, Phys. Rev. A*, **35** (1987) 4354.
[71] GIORGINI S., PITAEVSKII L. and STRINGARI S., *Thermodynamics of a trapped Bose-condensed gas, J. Low Temp. Phys.*, **109** (1997) 309.
[72] BIJLSMA M. and STOOF H. T. C., *Renormalization group theory of the three-dimensional dilute Bose gas, Phys. Rev. A*, **54** (1996) 5085.
[73] JIN D. S., ENSHER J. R., MATTHEWS M. R., WIEMAN C. E. and CORNELL E. A., *Collective excitations of a Bose-Einstein condensate in a dilute gas, Phys. Rev. Lett.*, **77** (1996) 420.
[74] STRINGARI S., *Collective excitations of a trapped Bose-condensed gas, Phys. Rev. Lett.*, **77** (1996) 2360.
[75] JIN D. S., MATTHEWS M. R., ENSHER J. R., WIEMAN C. E. and CORNELL E. A., *Temperature-dependent damping and frequency shifts in collective excitations of a dilute Bose-Einstein condensate, Phys. Rev. Lett.*, **78** (1997) 764.
[76] STAMPER-KURN D. M., MIESNER H.-J., INOUYE S., ANDREWS M. R. and KETTERLE W., *Collisionless and hydrodynamic excitations of a Bose-Einstein condensate, Phys. Rev. Lett.*, **81** (1998) 500.
[77] BOGOLIUBOV N., *J. Phys., USSR*, **11** (1947) 23.
[78] LEE T. D., HUANG K. and YANG C. N., *Eigenvalues and eigenfunctions of a Bose system of hard spheres and its low temperature properties, Phys. Rev.*, **106** (1957) 1135.
[79] ZAREMBA E., *Sound propagation in a cylindrical Bose-condensed gas, Phys. Rev. A*, **57** (1998) 518.
[80] RUPRECHT P. A., HOLLAND M. J., BURNETT K. and EDWARDS M., *Time-dependent solution of the nonlinear Schrödinger equation for Bose-condensed trapped neutral atoms, Phys. Rev. A*, **51** (1995) 4704.
[81] DALFOVO F. and STRINGARI S., *Bosons in anisotropic traps: ground state and vortices, Phys. Rev. A*, **53** (1996) 2477.
[82] FESHBACH H., *A unified theory of nuclear reactions, II, Ann. Phys.*, **19** (1962) 287.
[83] TIESINGA E., VERHAAR B. J. and STOOF H. T. C., *Threshold and resonance phenomena in ultracold ground state collisions, Phys. Rev. A*, **47** (1993) 4114.
[84] INOUYE S., ANDREWS M. R., STENGER J., MIESNER H.-J., STAMPER-KURN D. M. and KETTERLE W., *Observation of Feshbach resonances in a Bose-Einstein condensate, Nature*, **392** (1998) 151.
[85] STAMPER-KURN D. M., ANDREWS M. R., CHIKKATUR A. P., INOUYE S., MIESNER H.-J., STENGER J. and KETTERLE W., *Optical confinement of a Bose-Einstein condensate, Phys. Rev. Lett.*, **80** (1998) 2027.
[86] LARSON D. J., BERGQUIST J. C., BOLLINGER J. J., ITANO W. M. and WINELAND D. J., *Sympathetic cooling of trapped ions: a laser-cooled two-species nonneutral ion plasma, Phys. Rev. Lett.*, **57** (1986) 70.
[87] ABRAHAM E. R. I., MCALEXANDER W. I., GERTON J. M., HULET R. G., COTE R. and DALGARNO A., *Triplet s-wave resonance in $^6$Li collisions and scattering lengths of $^6$Li and $^7$Li, Phys. Rev. A*, **55** (1997) R3299.
[88] CATALIOTTI F. S., CORNELL E. A., FORT C., INGUSCIO M., MARIN F., PREVEDELLI M., RICCI L. and TINO G. M., *Magneto-optical trapping of Fermionic potassium atoms, Phys. Rev. A*, **57** (1998) 1136.
[89] ANDREWS M. R., TOWNSEND C. G., MIESNER H.-J., DURFEE D. S., KURN D. M. and KETTERLE W., *Observation of interference between two Bose condensates, Science*, **275** (1997) 637.
[90] BURT E. A., GHRIST R. W., MYATT C. J., HOLLAND M. J., CORNELL E. A. and WIEMAN C. E., *Coherence, correlations, and collisions: What one learns about Bose-Einstein condensates from their decay, Phys. Rev. Lett.*, **79** (1997) 337.

[91] KAGAN Y., SURKOV E. L. and SHLYAPNIKOV G. V., *Effect of Bose condensation on inelastic processes in gases, JETP Lett.*, **42** (1985) 209.
[92] WISEMAN H., MARTINS A. and WALLS D., *Quantum Semiclass Opt.*, **8** (1996) 737.
[93] HOLLAND M., BURNETT K., GARDINER C., CIRAC J. I. and ZOLLER P., *Theory of an atom laser, Phys. Rev. A*, **54** (1996).
[94] SPREEUW R. J. C., PFAU T., JANICKE U. and WILKENS M., *Laser-like scheme for atomic-matter waves, Europhys. Lett.*, **32** (1995) 469.
[95] OLSHANII M., CASTIN Y. and DALIBARD J., *A model for an atom laser*, in *Proceedings of the 12th International Conference of Laser Spectroscopy*, edited by M. INGUSCIO, M. ALLEGRINI and A. SASSO (World Scientific, Singapore) 1995, p. 7.
[96] BORDÉ CH. J., *Amplification of atomic fields by stimulated emission of atoms, Phys. Lett. A*, **204** (1995) 217.
[97] MEWES M.-O., ANDREWS M. R., KURN D. M., DURFEE D. S., TOWNSEND C. G. and KETTERLE W., *Output coupler for Bose-Einstein condensed atoms, Phys. Rev. Lett.*, **78** (1997) 582.
[98] BOIRON D., MICHAUD A., FOURNIER J. M., SIMARD L., SPRENGER M., GRYNBERG G. and SALOMON C., *Cold and dense cesium clouds in far-detuned dipole traps, Phys. Rev. A*, **57** (1998) R4106.
[99] DOYLE J. M., FRIEDRICH B., KIM J. and PATTERSON D., *Buffer-gas loading of atoms and molecules into a magnetic trap, Phys. Rev. A*, **52** (1995) R2515.
[100] BUTTS D. A. and ROKHSAR D. S., *Trapped Fermi gases, Phys. Rev. A*, **55** (1997) 4346.
[101] HOUBIERS M., FERWERDA R., STOOF H. T. C., MCALEXANDER W. I., SACKETT C. A. and HULET R. G., *Superfluid state of atomic* $^6$Li *in a magnetic trap, Phys. Rev. A*, **56** (1997) 4864.
[102] SCHNEIDER J. and WALLIS H., *Mesoscopic Fermi gas in a harmonic trap, Phys. Rev. A*, **57** (1998) 1253.
[103] VICHI L., INGUSCIO M., STRINGARI S. and TINO G. M., *Quantum degeneracy and interaction effects in spin-polarized Fermi-Bose mixtures, J. Phys. B*, **31** (1998) L1.
[104] DALFOVO F., GIORGINI S., PITAEVSKII L. P. and STRINGARI S., *Theory of Bose-Einstein condensation in trapped gases, Rev. Mod. Phys.*, **71** (1999) 463.
[105] INGUSCIO M., STRINGARI S. and WIEMAN C. E. (Editors), *Bose-Einstein condensation in atomic gases, Proceedings of the International Scool of Physics E. Fermi, Varenna 1998, Course CXL* (IOS Press, Amsterdam) 1999.
[106] FRIED D. G., KILLIAN T. C., WILLMANN L., LANDHUIS D., MOSS S. C., KLEPPNER D. and GREYTAK T. J., *Bose-Einstein condensation of atomic hydrogen, Phys. Rev. Lett.*, **81** (1998) 3811.

Direttore responsabile: GIUSEPPE-FRANCO BASSANI

Prodotto e realizzato dalla Redazione del Nuovo Cimento, Bologna
Stampato dalla tipografia Compositori, Bologna
nel mese di Giugno 1999
su carta patinata ecologica chlorine-free
prodotta dalle *Cartiere del Garda S.p.A.*, Riva del Garda (TN)

Questo periodico
è iscritto
all'Unione Stampa
Periodica Italiana

# La Rivista del Nuovo Cimento
## della Società Italiana di Fisica


Quote di abbonamento alla *Rivista del Nuovo Cimento* per l'anno 1999:

| | |
|---|---|
| Per i Soci in Italia | L. 357.000 |
| Per i non Soci in Italia | L. 440.000 |

Abbonamento cumulativo a *Il Nuovo Cimento*, Sezioni A, B e C, *Rivista del Nuovo Cimento*:

| | |
|---|---|
| Per i Soci in Italia | L. 2.200.000 |
| Per i non Soci in Italia | L. 2.560.000 |

La *Rivista del Nuovo Cimento* è in vendita anche in fascicoli separati al prezzo di lire 45.000 ciascuno; per ordini cumulativi di almeno 10 copie sarà concesso uno sconto del 10% sul prezzo complessivo. Le somme per l'abbonamento vanno versate (direttamente o per mezzo di un libraio) a **Editrice Compositori, via Stalingrado 97/2, 40128 Bologna**, alla quale occorre rivolgersi anche per l'acquisto di volumi arretrati o numeri isolati.
Trascorsi 6 mesi dalla data di pubblicazione, non saranno più accettati reclami per i fascicoli non pervenuti.
Subscriptions to *Rivista del Nuovo Cimento* for the year 1999:

| | |
|---|---|
| To members abroad | US $ 340.00 |
| To nonmembers abroad | US $ 430.00 |

Combined subscription to *Il Nuovo Cimento*, Sections A, B and C, *Rivista del Nuovo Cimento*:

| | |
|---|---|
| To members abroad | US $ 1960.00 |
| To nonmembers abroad | US $ 2440.00 |

Subscribers who wish to receive their issues by air mail will be charged extra postage. The airmail postage for 1999 amounts to US $ 55.00.
Single issues of *Rivista del Nuovo Cimento* may be purchased at the price of US $ 40.00 each; 10% discount on this price will be allowed for bulk orders of 10 copies or more.
Subscriptions should be sent, either directly or through a bookseller, to **Editrice Compositori, via Stalingrado 97/2, I-40128 Bologna, Italy**. Requests for back numbers or single copies should be directed to the same address.
Six months after publication complaints for issues not received will not be considered.
Per qualsiasi ordinazione rivolgersi a
For any order please write to

**EDITRICE COMPOSITORI**
Via Stalingrado 97/2
I-40128 Bologna, Italy

tel. +39-0514199711
fax +39-051327877
e-mail: 1865@compositori.it

Autorizzazione del Tribunale di Bologna n. 3382 del 24 dicembre 1968

ISSN 0393-697X

# La Rivista del Nuovo Cimento

volume 22 serie 4 numero 4 1999

## Experiments on Bose-Einstein condensation

G. M. Tino and M. Inguscio



Price of this issue $ 40.00
10% discount for bulk orders
of 10 copies or more

Prezzo del fascicolo lire 45.000
sconto 10% per ordini
cumulativi di almeno 10 copie